UNIVERSITÀ DEGLI STUDI DI PADOVA

Dipartimento di Fisica e Astronomia "Galileo Galilei"

Corso di Laurea Magistrale in Fisica

Tesi di Laurea

Realization methods of hyperpure germanium detectors with pulsed laser junction

Relatore

Prof./Dr. Davide De Salvador

Correlatore

Dr. Gianluigi Maggioni

Laureando

Salvatore Alessi

Anno Accademico 2020/2021

To my family

"Doubt is the origin of wisdom"
Rene Descartes

Acknowledgements

My greatest gratitude goes to my supervisor, Prof. Davide De Salvador whom I consider to be one of the most brilliant minds I have ever met, in his ability to reduce complex problems in their fundamental logical components, in his humility that distinguishes great scientists, and in his great talent in transmitting passion to his students. Another big thanks goes to Stefano Bertoldo who dedicated a lot of his time to explain to me the fundamental results obtained when I first arrived at LNL, becoming an excellent friend and a fundamental reference for me in LNL activities; I consider Stefano a great scientist capable of solving any problem without the slightest hesitation. Together with Stefano I want to thank Dr. Walter Raniero, Dr. Gianluigi Maggioni, Dr. Sara Carturan, and Dr. Daniel Riccardo Napoli, who welcomed me to the Legnaro Laboratories making me feel at ease and providing me with practical tools for research and human teachings for life.
A special thanks, the most important, to my family who supported me in everything.
A large part of my gratitude certainly goes to my colleague Pietro Grespan with whom I have shared a long part of my university career, and to all my friends who have supported me.

Summary

The hyperpure germanium detectors (HPGe detectors) are diodes optimized for operation at high reverse polarization voltages that find application in high resolution gamma-ray spectroscopy.

Such detectors are manufactured starting from hyperpure germanium crystals with impurity concentration of the order of $10^{10} atoms/cm^3$. Starting from this hyper-pure crystal, the diode is processed by doping one of the faces with a high concentration of substitutional impurities of the opposite type to the crystal to obtain a rectifier contact and the other face with a high concentration of impurities of the same type of the crystal. There are many reasons why Germanium is the best material for gamma spectroscopy and among the main ones, certainly stand out its high absorption coefficient due to the atomic number larger than silicon, its high mobility which is to the advantage of the charge collection especially for large volume detectors; these characteristics converge in excellent energy resolution and good timing resolution in the energy range relevant for gamma spectroscopy. The current state of the art is well represented by AGATA and GRETA who are taking the place of the EUROBALL and the Gammasphere spectrometer. The unprecedented advantages of germanium detector arrays such as AGATA and GRETA derive from the possibility of analyzing the pulse shape (Shockley – Ramo theorem) by comparing net and induced charge, allowing the identification of the point of interaction at the volume of the segment and therefore the tracking of the paths of the rays inside the array, through the development of specific algorithms.

In this dissertation a recent doping method is presented that allows the construction of shallow junctions through doping with the pulse laser melting (PLM) technique; such a junction has the advantage of being easily segmented, and does not contaminate the hyper-pure crystal in depth, allowing it to be eventually reprocessed.

The realization of this shallow junction is the result of the collaboration of the University of Padua and the Legnaro National Laboratories (LNL-INFN) in which I carried out the experimental activity.

My work at LNL has touched various areas of the development and characterization of segmented large volume HPGe detectors. In particular, various planar detectors have been developed to test the new processes as they are very easy to

treat thanks to their simple geometry. I will therefore present the procedures and the results of various optimizations of techniques that concern the construction and characterization through results of electrical measurements.

After a brief theoretical review, the presentation of the PLM methodology for doping and the description of the main measuring devices in the first chapter, I will move on to a brief and detailed description of the diode manifacturing starting from a planar crystal in the second chapter;

In the third chapter I will deal specifically with various aspects concerning the processing of the rectifying contact and the various optimizations tested; in particular I will focus on the problem of contaminants depositing on the crystal during the manufacturing process that negatively affecting the performance of the diode; new methods have been tested for effective control and removal of contamination. Finally, in the last chapter I will describe the applied optimizations by means of electrical characterizations and I will present efficient ways to measure particular quantities on segmented detectors.

Keywords: *Thesis*, *HPGe*, *Degree*, *Physics*, *Detectors*.

Contents

Chapter 1

Interdisciplinary background, techniques and instrumentation

1.1 Introduction

Interest in Germanium for technological research has a very troubled history. It is a semimetal of the IV group with atomic number 32, predicted by Mendeleev and initially called ekasilicon because it had to be located under the silicon on the periodic table. It was discovered 15 years later by Winkler, who thus confirmed Mendelev's prediction

The commercial use of Germanium took a turn in 1945, when the first solid-state amplifier was created based on Shokley's idea. This type of solid-state amplifier would serve to replace the vacuum tube amplifiers with which calculators of that period were built. The idea was precisely to use an external electric field to modify and control the electrical resistivity of the semiconductor device. After several unsuccessful attempts on Silicon, the project was entrusted to Bardeen and Brattain who replaced Silicon for Germanium because it was easier to purify and also has the same electronic structure as Silicon but electrons on a higher shell. In 1947 the first solid state amplifier was built by the two and baptized with the name "Transistor". In 1950, transistor factories took off with the introduction of transistor technology devices on the market. From pocket radios to transistor speaker amplifiers that replaced tube ones, germanium transistors started a new technological revolution. But they had one big flaw: germanium transistors warmed up easily, blocking circuits at relatively high temperatures; furthermore, Germanium was not as widespread in nature as Silicon. The research then moved back to Silicon and the first Silicon transistor was presented by Gordon Teal in 1954. The interest in Germanium then began to fade until a few decades ago when it began to

find application in radiation detectors, in microelectronics , in photonics, for solar energy. This interest is justified by the fact that of all semiconductors, Germanium has the smallest bandgap, is easier to purify and has a very high charge carrier mobility. Furthermore, the continuous technological battle for the miniaturization of high-performance devices is aimed at thinner junctions and therefore higher levels of doping (and therefore of purity control) never achieved before. As for HPGe detectors, hyperpure germanium allows to increase the thickness of the depletion zone and therefore the complete absorption of gamma photons for detection.

For this reason, in this thesis I will present an innovative technique for the doping of Germanium which allow to obtain homogeneously doped layers with a high density of electrically active dopant without causing damage to the lattice. This technique allows the incorporation of the dopant by diffusion through laser annealing (or pulse laser melting). The doping procedure is a relevant aspect in the research field of high purity Germanium detectors (HPGe). Among different doping processes (thermal diffusion, ion implantation with activation annealing) few of them are suitable for HPGe since heating the crystal may induce contamination that worsten the dopant background level.
Laser annaling , thanks to its reduced thermal budget allows to preserve the high purity while allowing to control and localize the doping according to the desired depth and therefore allows to maintain the original purity of the underlying crystal to control and localize the doping according to the desired depth (see secton 1.4). It must be optimized for operations of the diode at high reverse polarization voltages and moreover, thanks to the shallow junction, it allows the segmentation of the contact itself by photolitography, for the localization and tracking of the incident gamma photon inside the crysta.

1.1.1 Why Hyperpure Germanium?

The real breakthrough for particle detection came when the properties of semiconductor materials began to be understood and the first junctions began to develop for different purposes.

The advantage of using semiconductor materials to build detectors mainly derives from their compactness (just think that a solid state detector is like a cloud chamber in which the gas is replaced by a semiconductor) and the excellent energy resolution. This is due to the fact that semiconductors have a low ionization energy (1-5 eV per electron-hole pair) compared to other gas detectors (30 eV for a single ion pair) or scintillators (up to 300eV). So, for the same amount of energy deposited by the incident radiation, a relatively large number of pairs are created in a semiconductor detector (80 $e^{-}hole$ pairs $/\mu m$ for a minimum ionizing particle (MIP) are produced). The downside is that such materials are sensitive to radiation damage.

The most common detectors are the so called "surface barrier" detectors, reversed

biased pn silicon junctions, which find a myriad of applications in the detection of short range particles (α, β particles) but are not very suitable for the detection of more penetrating radiation and therefore for gamma spectroscopy.

This is due to the limit of the maximum width of the depletion region that can be obtained despite applying voltages near to the breakdown level **that must be attribuited** to the purity of the semiconductor.

In fact, the trick to detect very penetrating radiation is to create a thick depletion zone, that implies a great volume sensitive to the passage of radiation; the thickness w of the depletion region is given by 1.1

$$w = \sqrt{\frac{2\epsilon V}{eN}} \tag{1.1}$$

[Nea02] where N is the net imputity concentration of the bulk, V is the applied reverse bias voltage, ϵ is the dielectric constant and e the electronic charge (For more details see the chapter 1.3.3); then the lowering of the net impurity concentration, fixed a reverse bias potential, increases the thickness of the depletion region. Considering that the purest silicon that can be obtained has a dopant level of 10^{12} cm^{-3}, while the purest Ge reach less than $10^{10} cm^{-3}$, HPGe outperform the detection depth of Si by an order of magnitute reaching several cm collection depth.

Germanium properties	
Crystal Structure	Diamond (cubic)
Space Group	Fd3M
Lattice Constant	6.579060 Å
Crystal Density (at 300K)	5.3256 g/cm^3
Liquid Density	$5.60 g/cm^3$
Volume per Unit Cube	$1.8112x10 - 22 cm^3$
Atomic Density	$4.47110 - 22 cm^{-3}$
Melting Point	1210.4K
Specific Heats (at 273.3K)	0.3295 J/gK (Cp), 0.3284 J/gK (Cv)
Thermal Expansion (at 300K)	$5.9010^{-6} K^{-1}$
Thermal Conductivity (at 300K)	0.6 W/cm

1.1.2 Interaction radiation with matter: semiconductor materials in comparison

The detection of the radiation is based on its interaction with the medium of which the detector is made. A charged particulate radiation interacts with the Coulomb field of the nuclei causing multiple scattering,(i.e. deflections of the particle trajectory) and Bremsstrahlug (i.e. loss of radiative energy, which is inversely proportional to the mass squared of the incident particle and therefore very significant for electrons and positrons). Heavy charged particles ($M >> m_0$, where m_0 is the electron mass), on the other hand, lose energy by interacting with the electrons of the absorber medium and for further details see [Fan63]. The interaction of photons with matter occurs in various mechanisms that are classified according to the target and the effect of the interaction of the photon with the latter (absorption or scattering); in particular at energies beyond the ultraviolet range the dominant processes are photoelectric absorption, Compton scattering and pair production. At low energies the incident photon disappears and transfers energy to the target atom with the consequent expulsion of a photoelectron with kinetic energy given by the difference between the energy of the photon and the breaking energy of the bond; this **photoelectric absorption** mechanism represents the greatest contribution to the cross section in the low energy range and it results that the intensity of a monochromatic beam of photons at energy E decreases exponentially as a function of the penetration length x into the material:

$$I(x) = I_0 \mathrm{e}^{-\mu x}, \tag{1.2}$$

where the attenuation coefficient μ can be expressed as:

$$\mu(E) = N\sigma_\gamma(E) \tag{1.3}$$

where N is the atomic density and σ_γ the photoabsobition cross section and

$$E = h\nu = \frac{hc}{\lambda}$$

with $hc = 1{,}228$ KeV nm. Photoabsorption can be accompanied by fluorescence emission in which the expulsion of an electron from an inner shell causes the rearrangement of the electrons of the other shells with the emission of characteristic X-rays, in turn photoabsorbed inside the material and reconverted into less energetic photoelectrons. The **Compton effect** becomes predominant when the energy of the photon is greater than the binding energy of the electron which, with a good approximation, is considered free and initially at rest. In this case the photon is deflected after having transferred part of its energy to the electron. By the conservation of energy and momentum, the final energy of the photon is related to its initial energy and the angle of deflection θ by

$$E' = \frac{m_0 c^2}{1 - \cos\theta + (1/u)} \tag{1.4}$$

where $u = E/m_0c^2$ is the energy of incident photon in units of the electron rest energy. The maximum kinetic energy $T = E - E'$ of the electron occurs in the case of a frontal collision or $\theta = \pi$ showing a cut-off in the energy spectrum (or Compton edge) at

$$T_{\max} = E\frac{2u}{1+2u} \tag{1.5}$$

where $u = E/m_0c^2$.

Pair production is a threshold mechanism that occurs when a photon enters the coulomb field of an atom and converts into an electron-positron pair with opposite moments. The presence of the nucleus guarantees the conservation of the moment. The probability of interaction for pair production dominates for photon energies above the threshold $E = 2mc^2 = 1.022MeV$ and the excess energy $h\nu - 2mc^2$ is converted into the kinetic energy of the pair. While the electron can travel inside the material, the positron annihilates immediately giving rise to a pair of photons of 0.511 MeV each. These annihilation photons can be collected, contributing to the full energy peak if absorbed by the material; if instead these annihilation photons both escape, the net effect will be an energy double-escape peak at energy $h\nu - 2mc^2$ while if only one of these escapes, these events will contribute to a single escape peack located at $h\nu - mc^2$ (Fig 1.1)

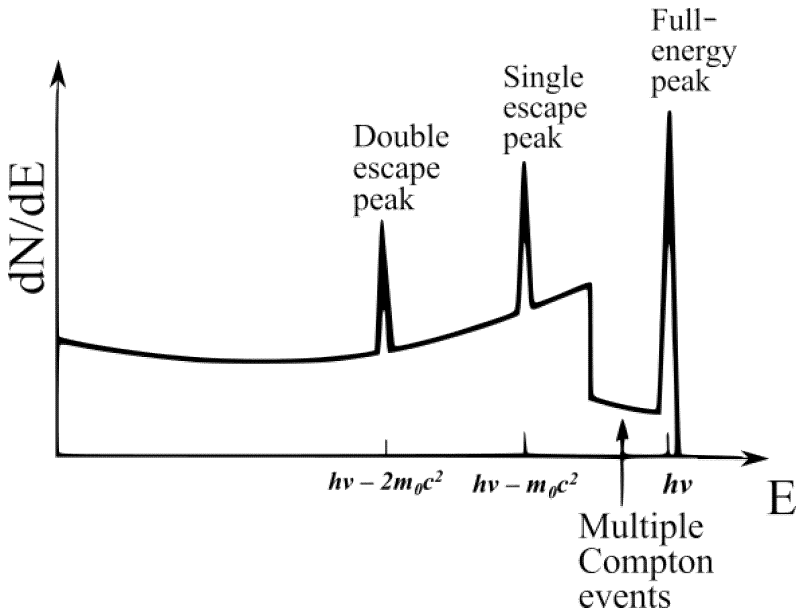

Figure 1.1: *Gamma interaction spectrum, in which the phototoelectric peak (full energy peak) and the two pair-production peaks are shown.*

The figure 1.2 shows the gamma ray absorbition cross section for various materials compared to Germanium. The attenuation curve is given by the contribution

of the three interaction mechanisms described above. As can be seen in the Fig-

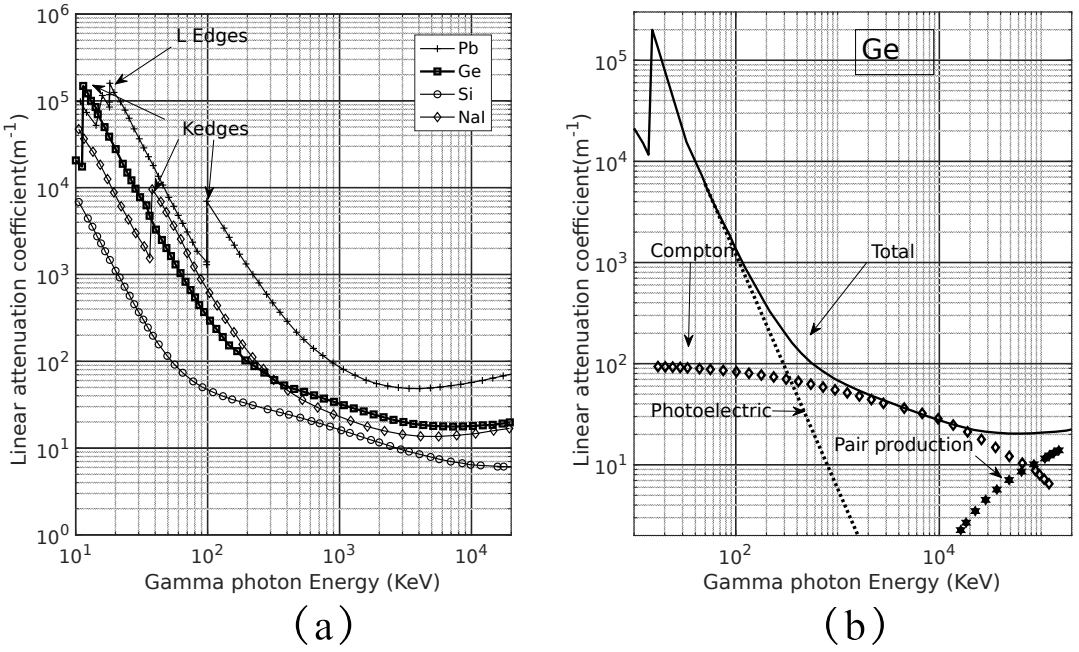

Figure 1.2: *a)Attenuation coefficient for various materials; b)attenuation coefficient of Ge in its component parts*

ure 1.2(b), at low energies of the gamma photon (<500MeV), the photoelectric effect dominates; the discontinuities seen in the absorption spectrum at low energies, called absorption edges, occur as more and more internal shell electrons are expelled as the gamma energy increases. the K absorption edge, for example, occurs in Germanium at energies 11.1 KeV; below these energies only L electrons and other higher order electrons can be photoelectrically expelled; moreover, as is clearly visible, the L edge reflects the three electronic sub-levels of the L shell. The photoelectric cross section decreases exponentially and, when the gamma energy photon reaches the threshold of 500KeV Compton scattering begins to become important; The Compton mechanism remains dominant up to 7MeV, while above this energy, the pair production mechanism becomes favored. Figure 1.3 shows a plane defined by the atomic number of the absorbent medium and the incident energy of the gamma rays, which highlights the regions in which the various mechanisms described are dominant. The lines delimiting these areas correspond to the values of Z and E for which two mechanisms have the same cross-section. It can be seen that at low energies and for high Z the photoabsorption dominates, for high energies and high atomic number the production of pairs dominates, while for intermediate energies the Compton effect is favored.

It is therefore deduced that for the detection of gamma rays it is convenient to

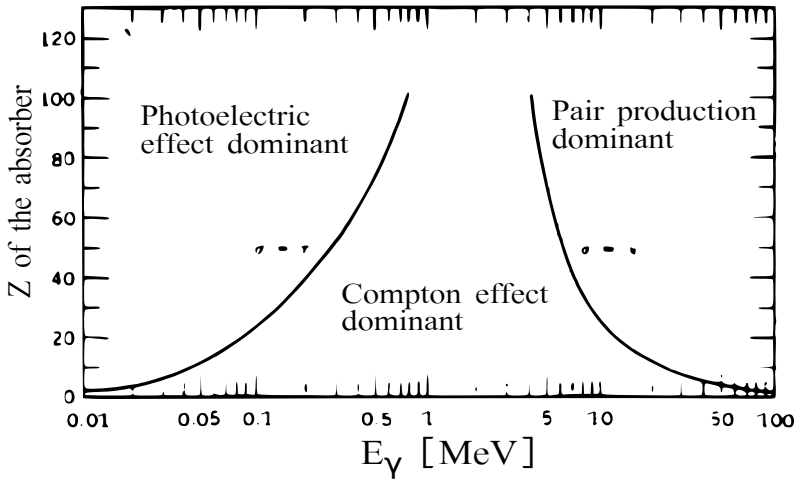

Figure 1.3: *Importance of the various interaction mechanisms as a function of the energy of the gamma photon and the Z of the absorber material [Att86]*

use a material with a high atomic number Z since the mechanisms of interest are photoabsorption and production of pairs; since $Z_{Ge} = 32 > Z_{Si} = 14$, Germanium is preferable to silicon; moreover, Germanium has greater mobility which allows a more efficient collection of the charge generated by the passage of a gamma ray. Furthermore, a Ge detector has high energy resolution thanks to its small bandgap (0.6 eV) which results in a very low electron-hole creation energy (2.96 eV) [Kno10; Kra87].

Finally, from the comparison of various semiconductors in the figure 1.4 it can be seen that the Compton window of the Silicon is visibly very large compared to that of the Germanium which therefore shows a greater "Compton efficiency". In general, silicon absorbs little due to its low zeta; CdTe has higher absorption even if in Compton regime it is comparable to Ge; the fairly large gaps of Si (Eg = 1.1 eV) and CdTe (Eg = 1.5 eV) allow them to work at room temperature as they have very few thermal carriers, while Ge (Eg=0.6 eV) must be cooled to eliminate intrinsic thermal carriers. On the other hand, the low gap allows to produce a large quantity of carriers for the same energy of a gamma event and this guarantees the absolute best energy resolution for HPGe. Ge is the purest material and can reach depletion tickness superior to the others. Depending on the applications, all of them can be used, but for the above reasons the material of choice for high resolution spectroscopy is germanium.

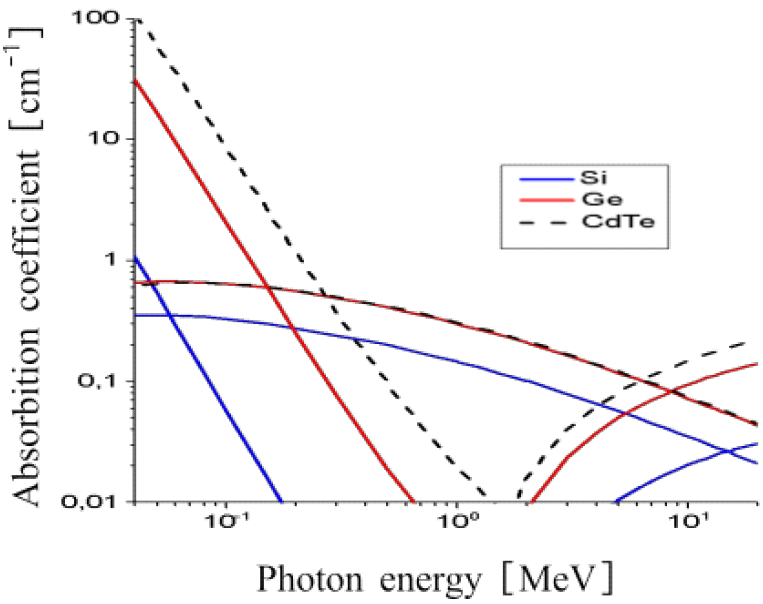

Figure 1.4: *Absorbition mechanisms for various semiconductors in comparison.*

1.1.3 Brief history of Ge detectors

In the 1960s, the purity of germanium attainable (concentration of net impurities $\sim 10^{13} cm^{-3}$) was not enough to allow the depletion of large volumes necessary for the efficient detection of gamma rays. To overcome this limitation, lithium was diffused on a p-type germanium crystal while it was heated and then "drifted" through the application of a specific voltage bias procedure [Pel60]. The result was a compensated semiconductor crystal in which Li donors could compensate acceptor impurities by giving almost zero net impurities. These large volume "litium-drifted" or Ge (Li) detectors could therefore be depleted but the impurities caused scattering of the free charge carriers reducing their mobility; furthermore they had to be immediately cooled [Tav64] within an hour after the drift process and they had to remain cold, because otherwise the Li atoms could diffuse destroying the compensated distribution of impurities. In the 70s techniques were developed to purify Germanium obtaining a purity of 10^{10}atoms cm^{-3} [HH82; BH70; Lla72] and the Ge (Li) detectors have been progressively replaced. The developed technique is based on zone refining through a selective melting; an RF coil is also passed continuously along the ingot allowing a motion of the molten material and, since most of the impurities have a greater solubility in liquid Ge than in solid Ge, at the end of the process, they tend to move with the molten zone and to be concentrated on one side of the ingot obtaining an electrically active impurity concentration of $10^{12} cm^{-3}$. Germanium is then melted in an inert crucible (Czochralski crystal growth method) and a crystal seed, immersed on the surface of the liquid, is pulled upwards in the presence of

hydrogen gas to passivate some defects and impurities [Hal06]. An entrapment of imputities occurs during the regrowth process, such that the seed tends to become p-type while the tail n-type . [HH82]. This method allows to obtain bowls of 10 cm in diameter with a net impurity concentration reduced to $10^{10} cm^{-3}$. Unlike Ge (Li), HPGe detectors have many advantages: they can be processed starting from both p-type or n-type crystals, they can be kept at room temperature for a long time and various types of contacts can be tested.. The current state of the art of germanium spectrometers, as already mentioned in the preface, are large volume coaxial HPGe detectors with an n+ hole-blocking contact and a p+ electron-blocking contact [] and are commercially available as simple detectors that do not provide the position sensing; alternatively they can be segmented planar based on [Ame+84; PR77; Gut90; Det76; Coo+07] junction contacts, which combine excellent resolution with position sensitivity, up to the segmented large volume coaxial detectors used in the AGATA and GRETA projects; moreover, among the most prominent modern manufacturing technologies is that with amorphous semiconductor contacts which simplifies the manufacturing process, [AL00; ALB07; LPD94; VBM04] allowing to obtain inter-contact spacings of 50 μm [Hea+07]. The current challenges concern the experimentation of new techniques that guarantee production reliability, low cost and high position-sensitive performance of high volume detectors.

1.2 HPGe detectors for gamma imaging applications

Gamma ray imaging is an ever-expanding sector of interest for medicine, biomedical research and astrophysics. It also finds application in the field of security and safety, providing potential tools for locating and characterizing radioactive materials in different environments in the event of accidents, storage or illicit use. In all these areas, the gamma emission of the isotopes is used as a fingerprint to identify the isotopes and locate the sources [Vet+18] in space. At the heart of every imaging technology are detectors that allow you to measure the position and energy released by gamma rays. The development of these detectors and their improvement in terms of efficiency, stability and cost reduction are therefore strategic activities with profound repercussions in the field of research but also of civil society.

1.2.1 Compton Camera

One of the most promising examples currently for imaging applications in various fields is the Compton camera. In the range of interest for the gamma emission, the Compton interaction is very strong (approximately between 0.1-10MeV) which causes a widespread release of energy in the materials. As a consequence, the use of collimators to form the images of rays with energy around the MeV is not very

effective since the rays are prevalentemete diffused by Compton and not selectively stopped [Mih+07].

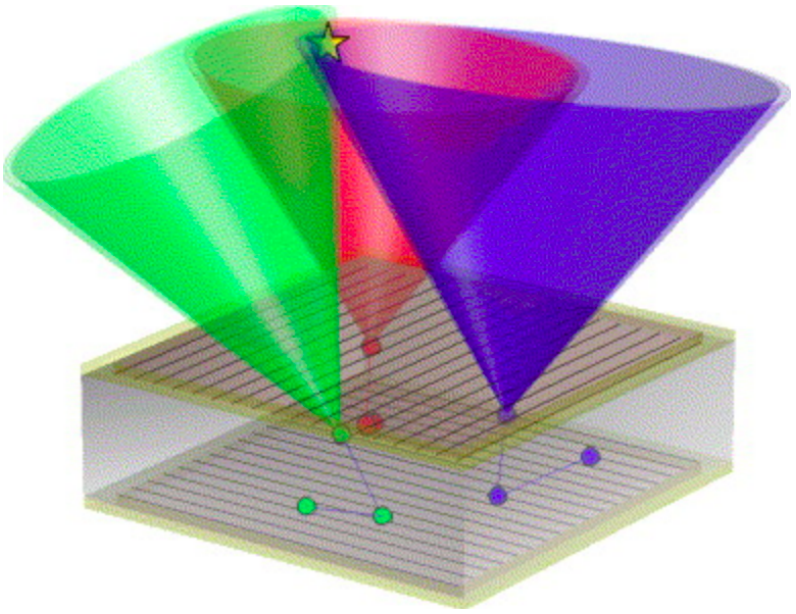

Figure 1.5: *Representation of a single double-sided segmented Ge detector acting as a compact Compton camera. Credits:[Mih+07]*

The Compton Camera [TNE74; SHS73] takes advantage of this prevalent interaction to reconstruct images without using collimators. Thanks to the use of highly segmented detectors, sensitive to position and energy, the energy released and the position of subsequent interactions (E, X, Y, Z) are measured and the direction and energy of the rays. This instrument has been proposed both in astrophysics and in medicine [TNE74; SHS73]. There are numerous projects and prototypes for its use in the medical field [Hue+16; Gho13; Har+12; Kri+15] and in security / safety [Vet+18]. In particular, the extension of gamma ray imaging techniques of the order of MeV would make it possible to use gamma prompts to monitor proton therapy treatments in real time [Kri+15] and would allow to extend the range of radiopharmaceuticals that can be used to more energetic emitters [Hue+16].

1.2.2 HPGe for imaging

The detectors used for the construction of Compton cameras are mainly semiconductor, Si, Ge and Cd (Zn) Te thanks to their high energy resolution compared to scintillators. Among these, many studies identify and use hyperpure Ge (HPGe) as a fundamental type of detector for the realization of the instrument. HPGe detectors have the best existing energy resolution and have a wide energy window in which the Compton interaction (150KeV-4MeV) prevails. HPGe also allows high

efficiency, having a Compton absorption coefficient similar to that of CdTe and 2 times higher than Si and having the ability to work with large volumes of interaction: the high purity allows to extend the electric field over thicknesses of several cm (see 1.4). The HPGe was therefore proposed and built in several prototypes of Compton chambers both as a monolithic element [Mih+07] and as a second detector after a silicon in a chamber optimized to operate at 120KeV [Har+12].

1.2.3 Double strip detectors

In this context, the most used detector geometry is a planar detector with double orthogonal strip on opposite faces. In this type of detector the hole and electron signals generated by a single interaction reach the two sets of opposite strips allowing X Y localization. Pulse shape analysis, widely developed for nuclear tracking applications (AGATA) allows to derive the Z position of the event considering the time difference between the hole signal and electrons. The total charge collected is as known proportional to the energy released in the event (E). There are prototypes for pixelated detectors that would have the advantage of a lower capacity on the single contact (less boring) but have the disadvantage of requiring a greater number of read-out circuits (one for each pixel instead of one for each strip) which are not easily scalable. in current implementations [Gho13]. The double strip detector is currently the most promising way to have a good number of "equivalent pixels" over a large area [Ish+10], also in consideration of the fact that a CMOS technology that can be directly implemented on Ge is not mature. This project focuses on the optimization of manufacturing processes and proposes the development of "strip type" contacts as a test bench. The process technology and knowledge developed could also be very useful for future developments for pixel detectors if advances in read-out electronics make this technology feasible.

1.2.4 Revolutionizing the methods of making contacts on HPGe

The strip segmentation of the detector takes place through the creation of electrically separated contacts (segments). On the one hand we will have an n + contact that accumulates the positive charge that generates the field, repels the holes and collects electrons. On the other side we will have the p + contact with the opposite role. The p + contact is made by ion implantation of Boron which (an almost unique case in semiconductors) is partially active even without carrying out aggressive heat treatments which would otherwise undermine the purity of Germanium [Bol+18]. The current technology to produce n + contacts is based on the diffusion of lithium at low temperature and is limited in terms of efficiency (creates a dead zone up to 1mm), segmentability (the insulation between the contacts would require digging at least 1mm deep grooves, leaving an area with a poorly controlled field of at least

as much width between one contact and another) and stability (subsequent heat treatments possibly necessary to remove the radiation damage cause the further diffusion of lithium risking to short-circuit the segments). An alternative technology is based on amorphous Ge contacts but has shown stability problems even at room temperature.

These problems limit the application of Germanium HPGe to imaging technologies, undermining the significant advantages that this material would have, increasing the maintenance cost and reducing the life of the devices. The laser annealing technology that we propose to develop and study in the project has the potential to overcome these problems: it incorporates large quantities of dopant in a small thickness (100nm) ensuring easy segmentability and does not contaminate the massive part of the material since it provides a strongly localized surface heating. The literature reports a remarkable stability of the laser junction following heat treatments [Mil+14; Imp+13; Lin16]. The project therefore aims to introduce a substantial improvement in the manufacturing processes of HPGe junctions with repercussions in the strategic gamma imaging sector, of fundamental importance in multiple sectors of research and applications, leading to significant social benefits. We believe that this experiment, at its low cost, can pave the way to give the institution a key role in a strategic sector. Possible developments are in larger projects (CALL) that implement the results in a real imaging device with high performance, or in the eventual involvement in production activities (SPIN-OFF). In this perspective, we believe that the development of a "fully laser" technology that also includes the creation of p + junctions is strategic. This would allow a production reality to have a single instrumentation for the realization of all contacts with obvious advantages of efficiency and costs.

1.3 Review of relevant semiconductor theory for the experimental work

In this section I will describe in a very synthetic and concise way the main quantities that characterize an inversely polarized junction, taking for granted some basic concepts for the development of the theory [Sze81a; Nea02].

1.3.1 Zero biased P-N Junction

Let's consider an intrinsic semiconductor. From elementary theory, the following equations hold for the concentration of free charge carriers (n_i for electrons ,p_i for holes) assuming that the Boltzmann approximation is valid ($(E_C - E_F) > 3kT$)

$$\text{Intrinsic} \begin{cases} n_i = N_C exp(-(E_C - E_{F_i})/kT) \\ p_i = N_V exp((E_V - E_{F_i})/kT) \end{cases} \tag{1.6}$$

$$n_i = p_i \qquad \text{with} \qquad n_i p_i = n_i^2 = N_C N_V exp((E_C - E_V)/kT) \tag{1.7}$$

where E_C is the minimum energy of the conduction band and E_V is the maximum energy of the valence band, N_C and N_V are respectively the effective density of states accessible in the conduction and valence band, E_{Fi} is the intrinsic Fermi energy , k the Boltzmann constant and T the temperature.
If substitutional impurities of p (or n) type are included in the lattice, the crystal is doped p-type or n-type. Assuming complete ionization of the doping impurities, the following relations hold for each of the two doped zones:

$$\text{P-doped} \begin{cases} p_p \sim N_a = n_i exp[(E_{F_i} - E_F)/kT] \\ n_p = n_i^2/p_p \end{cases} \tag{1.8}$$

$$p_p n_p = n_i^2 \qquad \text{with } p_p \neq n_p \tag{1.9}$$

$$\text{N-doped} \begin{cases} n_n \sim N_d = n_i exp[(E_F - E_{F_i})/kT] \\ n_n = n_i^2/p_n \end{cases} \tag{1.10}$$

$$n_n p_n = n_i^2 \qquad \text{with } n_n \neq p_n \tag{1.11}$$

in which the subscript on the concentrations indicates the type of doping of the semiconductor.
A p-n junction is a metallurgical junction of a $p-type$ semiconductor with a $n-type$. A graphic representation of the p-n junction at equilibrium is shown in the figure 1.7, while the respective band diagram is shown in the figure 1.6; these representations are susceptible to a quantitative analysis of the quantities involved; in fact, the figures refer to the equilibrium condition (zero bias potential)

in which the diffusion of the carriers from one side to the other of the doped areas is precisely contrasted by the electric field generated by the fixed spatial charges in the depletion area: the result is a perfectly balanced antagonist "diffusion-drift" mechanism in which there is no net motion of free charge carriers if the external potential applied is zero; it follows that the Fermi level for ptype is equal to that of n-type causing a bending of the bands.
The (internal) potential difference that generates the electric field that opposes the diffusion is called the built-in potential V_{bi} and is easily expressed as a function of the dopant density concentration N_a (in the p zone) N_d (in zone n); V_{bi} is obtained by

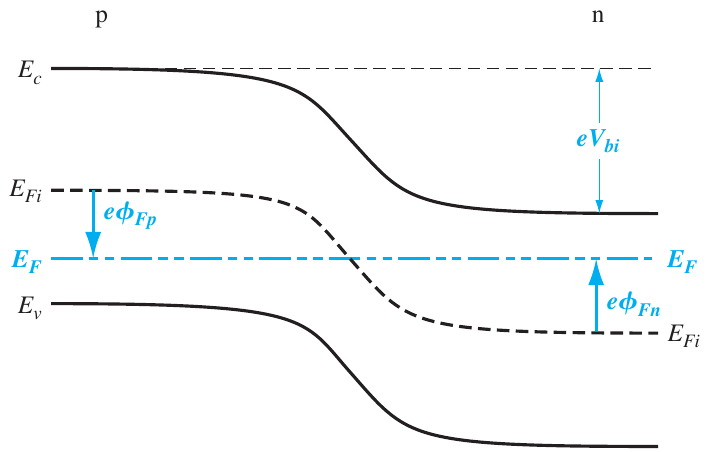

Figure 1.6: *Thermal equilibrium energy band diagram for a p-n junction with zero applied bias. Credits:[Nea02]*

using the equations 1.8 and 1.10 to obtain $|\phi_{F_n}|$ (difference between intrinsic (EFi) and extrinsic (EF) fermi potential in the zone p) and $|\phi_{F_p}|$ (difference between intrinsic (E_{Fi}) and extrinsic (E_F) still potential in zone n) referring to the figure, and adding their absolute values:

$$V_{bi} = |\phi_{F_n}| + |\phi_{F_n}| = \frac{kT}{e} log\left(\frac{N_a N_d}{n_i^2}\right) \tag{1.12}$$

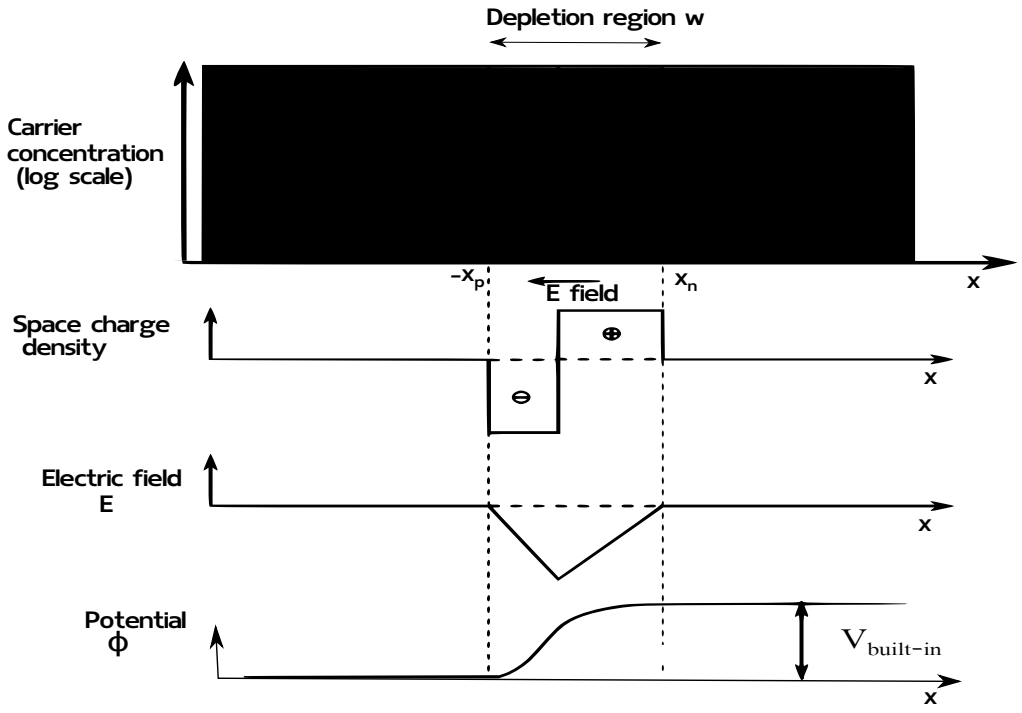

Figure 1.7: *The p-n junction with zero apllied bias*

In figure 1.7 the quantities, $\rho(x)$ concentration of space charge, electric field $E(x)$ and potential $\phi(x)$ are represented for the various spatial regions specified, assuming a uniform concentration of the doping in the two p-type and n-type parts (with a sudden change in concentration near the junction), in a condition of complete ionization:

$$\rho(x) = \begin{cases} -eN_A & \text{for } -x_p < x < 0 \\ -eN_D & \text{for } 0 < x < x_n \\ 0 & \text{elsewhere} \end{cases} \tag{1.13}$$

$$E = -\frac{d\phi}{dx} = \begin{cases} \frac{eN_a}{\epsilon\epsilon_0}(x + x_p) & \text{for } -x_p < x < 0 \\ \frac{eN_d}{\epsilon\epsilon_0}(x - x_n) & \text{for } 0 < x < x_n \\ 0 & \text{elsewhere} \end{cases} \tag{1.14}$$

$$\phi(x) = \begin{cases} 0 & \text{for } x < -x_p \\ \frac{eN_a}{2\epsilon\epsilon_0}(x + x_p)^2 & \text{for } -x_p < x < 0 \\ \frac{eN_d}{\epsilon\epsilon_0}(x_n \cdot x - \frac{x^2}{2}) + \frac{eN_a}{2\epsilon\epsilon_0}(x_p^2) & \text{for } 0 < x < x_n \\ V_{bi} & \text{for } x > x_n \end{cases} \tag{1.15}$$

Therefore, assuming a dopant concentration profile $\rho(x)$ (eq. 1.13), The electric field can be obtained using the Gauss theorem, considering that at equilibrium the electric field outside the depletion zone is equal to zero. The potential is calculated by integrating the spatially electric field and using the appropriate boundary conditions. Note that passing from the p-doped to n-doped zone in figure 1.7 the potential increases ($d\phi = -Edx$) but in the band diagram of figure 1.6 the energy band bends proportionally but "on the contrary" as the one represented in the graph is the energy accessible to an electron and therefore $\Delta\mathcal{E} = -eV_{bi}$. We can affirm that the formation of fixed space charges generate an electric field that bends the bands by an energetic amount $\Delta\mathcal{E} = -eV_{bi}$; this means that an electron cannot go up the energy barrier from the n region to the p region in the conduction band nor a hole can pass from p to n in the valence band if the junction is in equilibrium or inversely polarized.

Starting from the expression of V_{bin} as a function of the depletion width in n-type region (x_n) and in p-type region (x_p) and from the condition of spatial neutrality:

$$\text{Built-in} \qquad V_{bi} = (\phi(x = x_n)) = \frac{e}{2\epsilon\epsilon_0}\left(N_d x_n^2 + N_a x_p^2\right) \tag{1.16}$$

$$\text{Neutrality condition} \qquad eN_a x_p = eN_d x_n \tag{1.17}$$

it is possible to derive x_n and x_p as a function of the dopant concentration N_a, N_d and the built-in potential

$$x_n = \left[\left(\frac{N_a}{N_d}\right)\frac{2\epsilon\epsilon_0 N_A V_{bi}}{eN_d(N_a + N_d)}\right]^{1/2} \text{ and } x_p = \left[\left(\frac{N_d}{N_a}\right)\left(\frac{2\epsilon\epsilon_0 V_{bi}}{e(N_a + N_d)}\right)\right]^{1/2} \tag{1.18}$$

and the total depletion width

$$w = x_n + x_p = \left(\frac{2\epsilon\epsilon_0 V_{bi}}{e}\frac{(N_a + N_d)}{N_a N_d}\right)^{1/2} \tag{1.19}$$

1.3.2 Reversed Biased P-N Junction

An inversely biased junction is a diode to which a positive potential is applied to the n contact and a negative potential to the p contact in order to increase the built-in potential and widen the depletion zone.

$$V_{tot} = |\phi_{F_n}| + |\phi_{F_n}| + V_R = V_{bi} + V_R \tag{1.20}$$

$$w = x_n + x_p = \left(\frac{2\epsilon\epsilon_0(V_{bi} + V_R)}{e} \frac{(N_a + N_d)}{N_a N_d} \right)^{1/2} \tag{1.21}$$

to obtain the maximum electric field we consider the triangular profile of the electric field module in figure 1.7; it is clear that the area subtended by this triangle corresponds to the potential -Vbi if the junction is in equilibrium while it corresponds to $-(V_{bi} + V_a)$ if inversely polarized (being $E = -d\phi/dx$); the maximum electric field is the height while the depletion width is the base; therefore

$$-E_{max} \cdot w \cdot \frac{1}{2} = (V_{bi} + V_a) \tag{1.22}$$

$$\implies E_{max} = -2(V_{bi} + V_R)/w \tag{1.23}$$

another way is to combine the 1.14 equations of the electric field for the two doped regions. At this point it is easy to introduce the Capacitance of a reverse biased junction; in fact, if the reverse bias potential V_R increases in modulus, the depletion width w also increases and therefore the space charge in the depletion zone increases:

$$C = \frac{dQ}{dV_R} = \frac{eN_d dx_n}{dV_R} = \frac{\epsilon\epsilon_0}{w} \tag{1.24}$$

1.3.3 Highly asymmetrical junction approximation

if $N_a >> N_d$ the junction is said to be highly asymmetric or one-side junction.

$$\text{Depletion tickness:} \qquad w \sim \left(\frac{2\epsilon\epsilon_0(V_{bi} + V_R)}{e} \frac{1}{N_d} \right)^{1/2} \tag{1.25}$$

$$\text{Capacitance} \qquad C = \frac{\epsilon\epsilon_0}{w} \sim \left(\frac{e\epsilon\epsilon_0 N_d}{2(V_{bi} + V_R)} \right) \tag{1.26}$$

$$\implies \frac{1}{C^2} = \left(\frac{2\,(V_{bi} + V_R)}{e\epsilon\epsilon_0 N_d} \right) \tag{1.27}$$

The equation 1.27 shows that the square of the inverse of the capacitance is linearly dependent on the reverse bias voltage and the dopant concentration of the low-doped region.

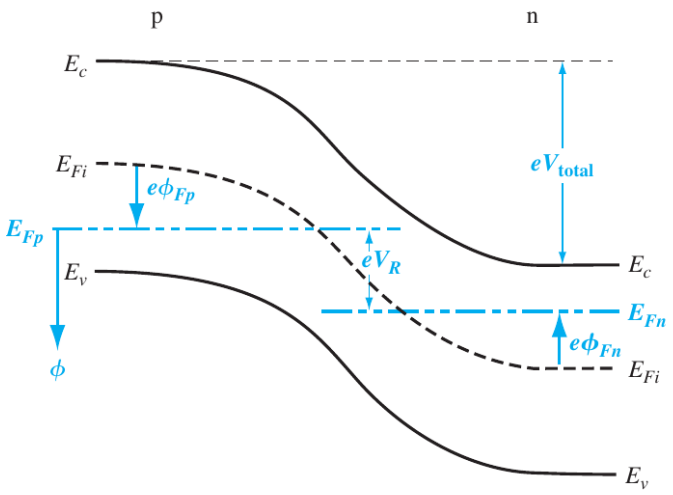

Figure 1.8: *Energy-band diagram of a reversed biased p-n junction. Credits: [Nea02]*

1.3.4 Breakdown Mechanism in P-N Junction Diode.

The leakage current of a diodes depends on two main contributions: The current coming from the junction border or lateral surface. This is due to surface conduction and is generally reduced or by proper electrical passivation of the diode lateral surface by means of dielectric layer deposition or chemical treatments as in our case.

The current generation coming from the area of the junction that may depend on 4 different physical mechanisms [Duf+10] that are briefly summarized in Fig 1.9

- Diffusion current: This is due to band-to-band thermal generation of carriers that are captured by the junction field after diffusion. The temperature dependence is due to a Boltzman term with an energy activation equal to the energy gap, that is the energy cost needed to produce the carrier couple. No dependence on the voltage is present since the diffusion region extension does not depend on the voltage.

- Reed Hall Shockley generation current. This is also called trap assisted generation since it is mediated by deep levels traps that induced by defects or impurities. The current is generated into the depletion region where the traps are empty due to the field, therefore the traps can aid the thermal transfer of an electron of valence band to conduction band by 2 steps jump passing through the trap level energy ET. The energy cost of each jump is lower than energy gap. As a first approximation, the ET level is at about the middle gap and therefore the activation energy is about Eg/2. The RHS generation occurs into depletion region and is proportional to the depletion region length. Being

this last proportional to the square-root of the reverse bias the RHS current is proportional to $V^{0.5}$.

- Band to band tunneling current. This is the quantum mechanical transfer of an electron of the valence band to the conduction band through a barrier. This mechanism is not thermal activated and occurs only if the depletion region is of the order of a few nanometers. This is absolutely not the case of an asymmetric junction on a HPGe germanium that has a macroscopic depletion length from 200microns to cms depending on the bias.

- Trap assisted Tunneling (TAT). This 2 steps mechanism involves the tunneling of an electron of valence band to a trap level into the depletion region, and the thermal activation emission of the electron from the trap to the conduction band. Global activation energy has an energy cost (activation energy) similar to the RHS mechanism. The V dependence is generally with V^X with X greater than 0.5.

Both lateral and area currents may undergo breakdown when a strong electric field is present. In this case the energy for the hole-electron couple production is given by the field itself in the form of kinetic energy due to electric force acceleration. The phenomenon is an avalanche phenomenon that depend nonlinearly on the field and has a threshold given by the fact that the electron kinetic energy has to overcome the energy gap before carrier production starts. The thermal dependence of breakdown is quite weak and depends on the mobility variation with temperature, no activation thermal energy giving a Boltzman term is needed to start breakdown. Generally, HPGe standard junction may reach thousands of volts and an electric field as high as some KV/cm before breakdown. Field concentration in some regions of the junction due to structural imperfection or defect may cause breakdown even at lower voltage.

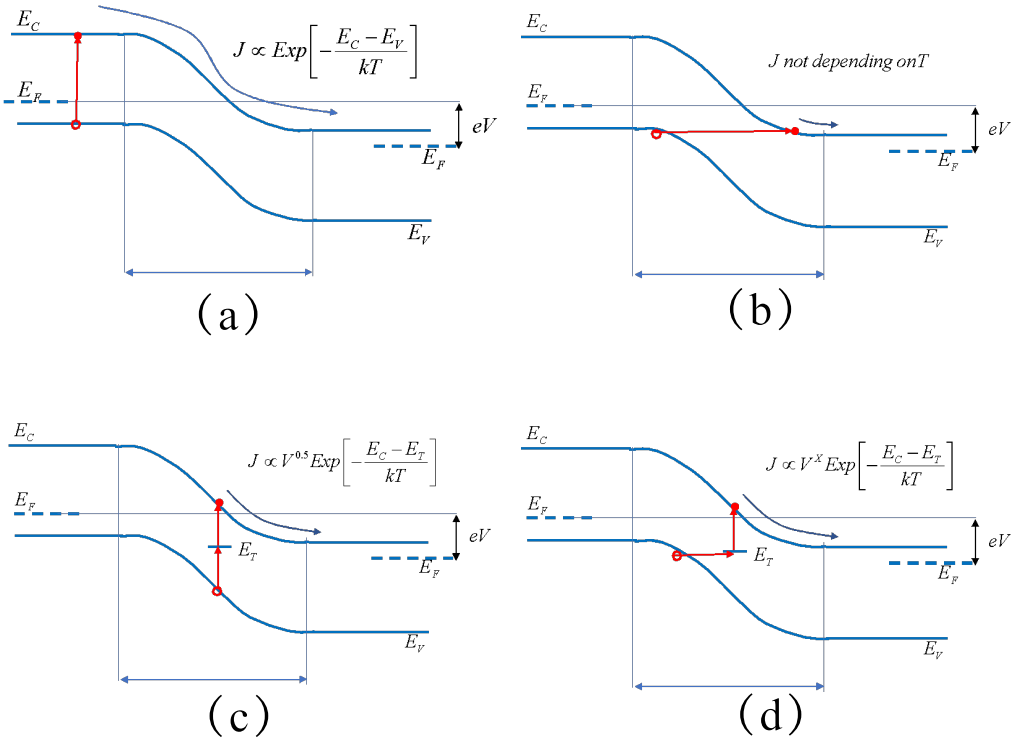

Figure 1.9: *In the figure the four main mechanisms producing non lateral leakage current are depicted. The bent band scheme of a diode under reverse bias V is reported. Ec and Ev are the conduction band and valence band edges levels. EF is the Fermi level. J is the leakage current density. The generation mechanism produces a hole-electron couple that produces a current along the junction field.*

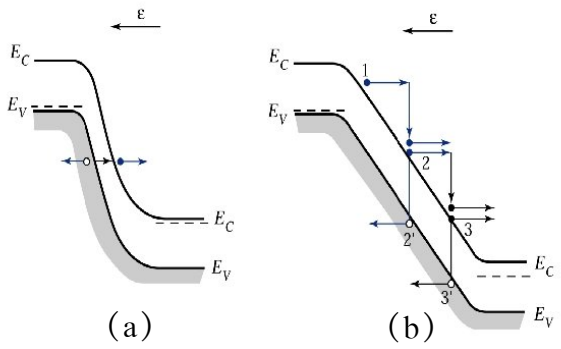

Figure 1.10: *band diagram of a pn junction in breakdown conditions illustrating the tunneling (a) and avalanche brekdown mechanisms (b). Credits: [Sze81b]*

1.4 Laser annealing (PLM doping methodology)

1.4.1 Pulsed laser treatment for the incorporation of the dopant

The pulse laser melting (PLM) is a doping technique recently proposed by LNL-DFA research team to create the pn junction on a surface of the HPGe crystal [Mag+18; Ber+21]. After the deposition of the dopant, the substrate is treated with laser pulses that melts the surface for a very short time (<100 ns) and allow the diffusion of the dopant inside the wafer substrate up to thicknesses of hundreds of nanometers.

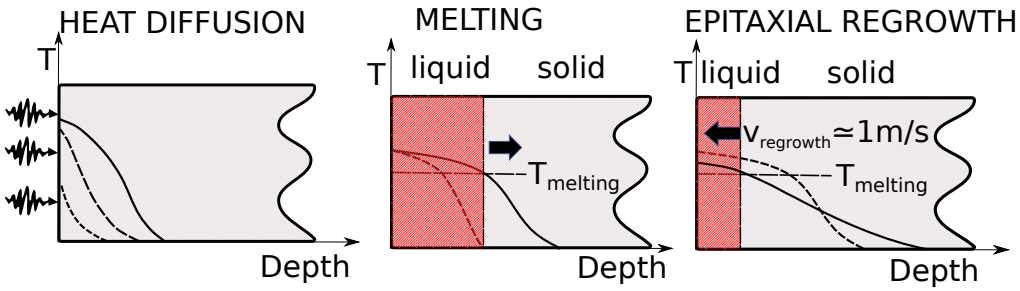

Figure 1.11: *The three phases that schematize the doping of a shallow region through the pulse laser melting process*

The physical steps involved in this process can be summarized as:

- **Heat diffusion - Melting** In a first stage the UV laser deposit the energy at the surface of the material due to photelectric absorpiton. If energy is high enugh melting of the surface may occur. The following simplified equation can describe the time evolution of temperature under a transient irradiation.

$$\frac{\partial T}{\partial t} = \frac{1}{\rho C_p}\frac{\partial}{\partial z}\left(k\frac{\partial}{\partial z}T\right) + \frac{\alpha}{\rho C_p}I(z,t) \tag{1.28}$$

  where z is the depth, $I(z,t)$ is the light power density of the laser at depth z and time t, T is the temperature, and p, C_p , k, and α are the density, specific heat, thermal conductivity, and absorption coefficient of the sample, respectively [Bae+79]. If the absorbent medium is homogeneous, the power density can be modeled as:

$$I(z,t) = I_0(t)(1-R)\exp(-\alpha z) \tag{1.29}$$

  where R is the reflectivity of the semiconductor surface and I_0 is the power density of the laser; The time duration of the pulse we used with the laser

Excimer Krf at the DFA laboratories is of the order of 25 ns. The tipical decay time of the temperature shot is of the order of hundreds of ns. The 248 nm wavelegth we used in our processes laser has a penetration depth $1/\alpha = 7nm$ thus being very close to the surface. Reflectivity R strongly depends on the sample roughness and this can be a critical point that may condition the reproducibility of the process. Surface finish of the HPGe sample will be one of the topic disussed in this thesis in section 3.2.1.

- **Diffusion of the dopant in melting regime** The conditions for obtaining the diffusion of the dopant within the bulk are:

  1. The presence of a concentration gradient of the doping atoms, in our case they are deposited on the surface;
  2. Thermal energy sufficient to cause the motion of the dopant atoms in the material, supplied by the pulsed laser in the melting regime. Exceeding a melting energy threshold, a liquid/solid interface is created, which advances inside the bulk following the diffusion of heat until it reaches the maximum melt depth; (the maximum melt depth monotonously depends on the energy deposited [Bru+12; Kal+16] as we will see with examples in the paragraph 1.4.2)
  3. at this stage the diffusion of the dopant begins and should follow Fick's law

$$\frac{\partial C(z,t)}{\partial t} = \frac{\partial}{\partial z}\left(D(z,t)\frac{\partial C(z,t)}{\partial z}\right) \qquad \text{Fick } 2^\circ \text{ law} \tag{1.30}$$

  where the diffusion coefficient follows the Arrhenius law

$$D(z,t) = D_0 \exp\left(\frac{E_a}{k_B T(z,t)}\right) \tag{1.31}$$

  The diffusion of the dopant is limited only to the molten part of the germanium because the diffusion coefficient in the liquid is typically 5 orders of magnitude higher than that in the solid

- **Velocity of epitaxial regrowth** Once the pulse is over, the subsequent cooling causes a fast recrystallization, with the interface moving with a speed that depends on the heat dissipated by the bulk [Eds82]:

$$v_{regrowth} = \frac{k}{\Delta H \rho}\frac{\partial T}{\partial z} \tag{1.32}$$

  where H is the enthalipy of fusion, ρ the germanium density an k the thermal condictivity. The whole process has a duration of about 100ns so it is strongly out of equilibrium.

The PLM technique allows the control of crystal contamination because its local heat treatment action, unlike thermal annealing in which all the crystal is heated.

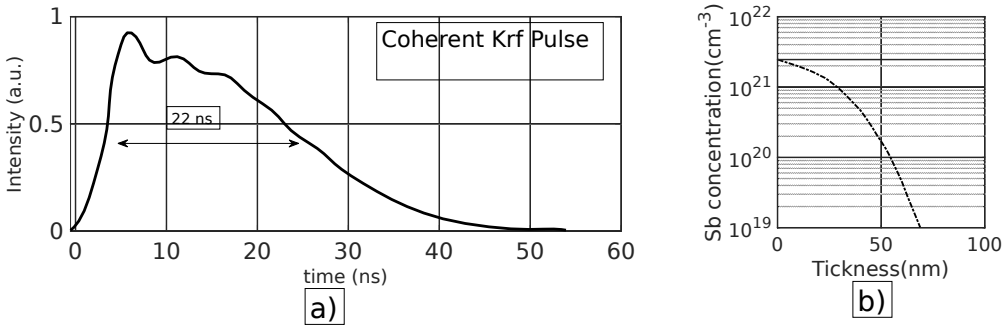

Figure 1.12: *a)Single pulse intensity b)Sb profile diffusion after PLM*

The laser pulse melts a thickness of 200nm from the surface, with pulse time less than 100ns; the sputtered dopant atoms diffuse in this region, towards the germanium allowing the substitution and therefore the doping. In this local-out of equilibrium process, the bulk of the germanium remains at room temperature and therefore this technique limits the contamination;
In confirmation of what has been said, our research group has shown in the following article [Bol+18] that the PLM technique preserves purity if compared to other dopant diffusion processes at high temperatures. The analysis shows that there is a strong activation of acceptor levels inside the n-type bulk HPGe by diffusion through annealing at high temperatures in a standard furnace, and this problem is overcome by introducing the laser thermal annealing technique.

More in detail, four point-probe measurements and Hall measurements are performed to measure the carrier density in the bulk of HPGe species treated with various surface doping approaches including processes with aggressive thermal cycles; the measurements are performed at a temperature ranging from room temperature to about 100K. For example, at low temperatures, for a bulk of n-type Germanium, positive charges are measured after treatment in a standard furnace, while negative charges are measured for samples treated with the PLM technique. In Fig. 1.13 the carrier concentration is reported as a function of temperature in an Arrhenius plot (log of the carriers vs inverse of the temperature). Two zones are distinguished, as expected: starting from room temperature (low $1/k_bT$ values) thermal carriers of intrinsic regime dominate in almost all the species, by reducing the temperature carriers exponentially decreases down to the saturation regime where the carrier due to residual dopant contaminants are measured. . This last regime is of particular interest since the charge density that occurs is equal to the concentration of the ionized dopant; the higher the saturation plateaus, the more contaminated the crystal and the less efficient the doping process is. In particular a residual doping level of about 10^10 is measured in the starting p and n type material (black

symbols). Once treated above 600°C the dopant level increases reaching even10^14 for treatments at 800°C. The contamination is of p-type and is most likely due to copper fast diffusion into the bulk. The only doping treatment that do not change the residual doping level are the boron implantation (green stars), that do not need any thermal treatment for activation and the Pulsed Laser Melting (light blue circles). In fact, It can be clearly seen that the curve corresponding to the PLM has a very low saturation zone in terms of charge concentration and therefore of dopant concentration in the bulk. This demonstrates that PLM is an optimal candidate for HPGe doping.

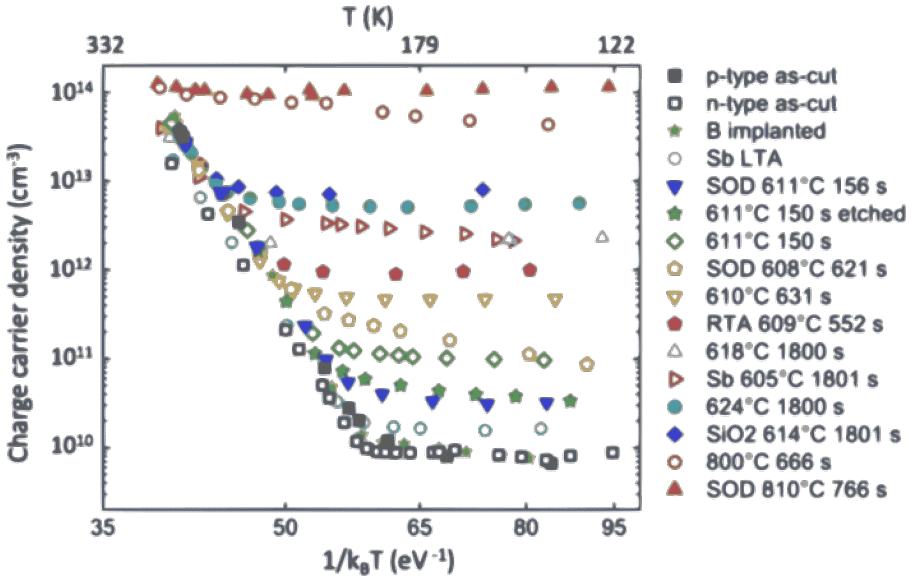

Figure 1.13: *Charge-carrier density curves, function of* $(k_BT)^{-1}$. *Full symbols refer to p-type starting substrates, empty symbols to n-type. Credits [Bol+18]*

In the present work we mainly used a KrF laser at DFA, but we also have access to a Nd:YAG laser at LNL. In the following we reporte the main characteristic of both the lasers:

Solid State	**Nd:YAG(LNL)**	**Excimer KrF(Unipd)**
λ	355 nm	248 nm
time pulse	7 ns	22 ns
Pulse Repetition Rate	10 Hz	$1-10Hz$
Energy Density	400 mJ/cm^2	50-1300 mJ/cm^2
Circle spot diameter	7 mm	
Square spot dimension	4x4 mm^2	5x5 mm^2
Homogeneity	$gaussian \sim 15$ %	<2% (2 sigma)

1.4.2 Junction depth and maximum melt depth from SIMS measurements

The Figure 1.14 shows four selective SIMS profiles that represent the concentration of active Sb incorporated in germanium with the pulsed laser technique [Car+20]; in particular the blue curves are related to laser energy density of $0.6 J/cm^2$ and are divided into dotted (1pulse) and continuous (8 pulse); the orange curves correspond to an energy density of the laser beam of 0.5 J / cm^2 and are also distinguished in dotted (1 pulse) and continuous (8 pulse). The 8-pulse concentration profiles (dotted lines) show a steep drop at well-defined depths (162nm for the orange curve and 281nm for the blue curve) and this is due to the fact that the liquid / solid interface never exceeded this depth in none of the eight pulses (maximum melting depth); consequently the dopant, subjected to various melting stages of the multipulse treatment, gradually accumulates near the corresponding interface at maximum melt depth because it cannot diffuse beyond; it is also clear from the figure 1.14 that the maximum melt depth depends on the energy density E of the laser pulse. The same effect is not visible in a single pulse (dotted line) due to the shorter diffusion time than in the case of eight pulses. In fact, according to Fick's law, the evolution of the concentration profile is such that it will tend to oppose the concentration gradient, flattening the concentration profile over very long times in melting regime; it is therefore clear that the maximum melt depth represents a boundary condition to the Fick equation in which dopant will accumulate over time, because it fails to cross the solid-liquid barrier.

The dopant profile Sb creates a junction in the p-type doped crystal; this junction is highly asymmetrical, in fact the dopant incorporated through the laser process reaches concentrations of $10^{20} cm^{-3}$ on the doped region while maintaining impurity concentrations of $10^{10} cm^{-3}$ on the HPGe side; moreover, the junction depth is tickness at which compensation between the concentration of the dopant and that of the HPGe impurities occurs.

The junction tickness falls within a depth range between the thickness corresponding to the minimum dopant concentration measured at 1 pls (SIMS sensitivity limit) and the maximum melt depth identified by the 8-pulse SiMS measurement; for a pulse laser the depth range in which the junction falls will be [180,281] nm for energy density$0.6 J/cm^2$ and [119,160] nm for energy density $0.5 J/cm^2$ (see figure). We also expect that within this range the junction falls closer to the maximum melt depth, but a more precise experimental measurement is not allowed as already mentioned, due to the sensitivity limit of the SIMS (it is not possible to measure antimony concentrations below $10^{18} cm^{-3}$); such a solution could be found solving the equations 1.28,1.30,1.32 at the same time managing the evolution of the solid/liquid interface step by step, but this topic goes beyond the objectives of my thesis.

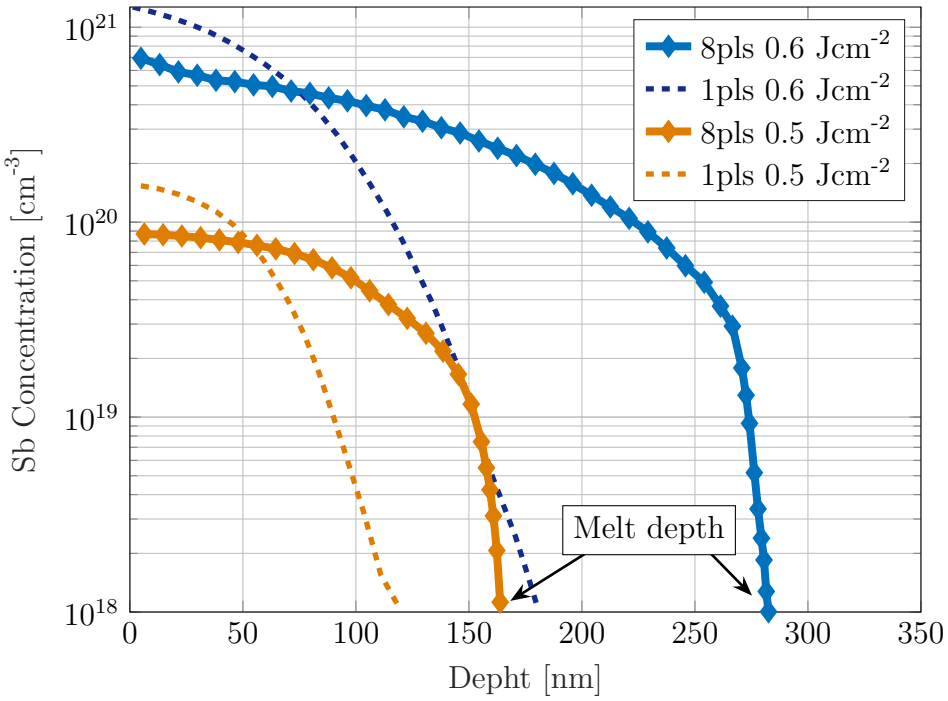

Figure 1.14: *Selection of representative Sb depth profiles measured by SIMS, after 1 pulse (dotted blue line) or 8 pulses (solid blue diamond line) KrF at 600 mJ/cm 2 laser, on Ge samples with deposited prior to irradiation 1 ML (orange) or 2 nm Sb (blue) in the case of KrF processes. The profiles have been extrapolated to the surface within the first 10–20 nm (dashed lines), where SIMS exhibit significant artifacts. Credits: Carraro et al. "N-type heavy doping with ultralow resistivity in Ge by Sb deposition and pulsed laser melting",Fig 1 [Car+20]*

The abrupt junction model is consistent to describe a highly asymmetric junction for the calculation of the depletion and the maximum electric field as reported in eq. (1.25); in fact the built-in depletion tickness is very large ($\sim 200\mu m$) in the low-doped region (HPGe) and negligible in the high-doped zone; Since the germanium of the bulk is hyperpure, such a high doped junction is highly asymmetrical.

From these considerations we can conclude that the junction is abrupt-like even if as mentioned before we are not able to establish through SIMS measurements the trend of the dopant concentration curve near the compensation zone, because of the sensitivity limits of the SIMS measure described.

1.5 Instrumentation

1.5.1 Electronic Devices for IV measurements

The Keithley 237 / 2400 source-measure unit is a precision device capable of supplying voltage and measuring current (or vice versa) simultaneously[Ins01].

Figure 1.15: *The two Keithleys 237 used for reverse current measurements as a function of reverse bias voltage*

In particular in V_{source}-$I_{measure}$ mode, it is able to provide a potential difference across its terminals from 100 μV up to 1100 V and measure a current from 10fA to 100mA. The Keitheley is a hybrid of analog digital circuits; these two electronic parts are separated to avoid interference and problems in the measurement processes.

Figure 1.16: *Keithley 2400*

When carrying out current measurements, it is necessary to check the current leakage limit in the cables. Bad results may in fact be due to current losses through both low and high DUT's resistance measuring (DUT=Device Under Test). A standard coaxial cable has a good resistance of an insulating layer $R_L = 100G\Omega$.

In the case of **high DUT's resistance** of the order of $1G\Omega$, then there will be a loss of about 1% of the current through the coaxial cable. A triaxial cable is therefore required. The triax cable has a central core that provides the high voltage V_C surrounded by an internal shield that has the potential $V_{IS} = V_C \pm 2\text{mV}$ and an external shield grounded.

The small difference of potential between the core and the internal shield ensures very little current loss from the core through the internal shield. The maximum lost current can be calculated for example by considering $R_L = 100G\Omega$, setting a maximum error $\Delta V_{C-IS} = 2mV$. This leads to a leakage current of $2mV/100G\Omega = 20fA$ which is precisely the order of magnitude of the sensitivity of the instrument. The internal shield will never be brought to ground because it is kept at the same potential as the Core by a buffer circuit with an error of $\pm 2mV$ as already mentioned. So the current leakage between core and internal shield is reduced and moreover there will be no more leakage between the core and the external shield, because the internal shield "buffers" the small variations of potential with respect to the Core due to currents through R_G.

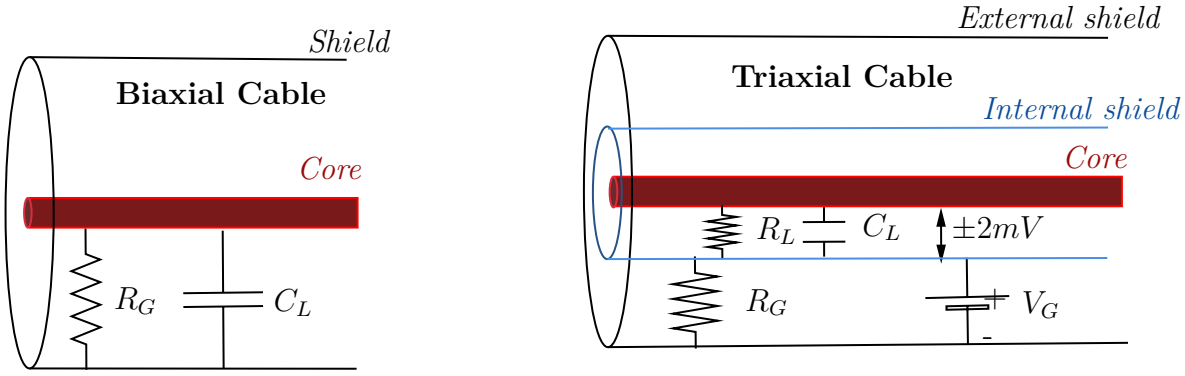

Figure 1.17: *Coaxial and triaxial cable circuits*

In addition, the "Local Sense" option, activated by default, ensures a "readjustment" of the potential by monitoring the output through a potential measurement and sending the feedback to the voltage source. But in the case of **DUT's low resistance**, the "Local Sense" is not enough, since if the resistance is too low it would tend to abruptly lower the potential across the terminals through a very high current. To work around this problem, the "Remote Sense Control" option is available. This consists of connecting another triax cable through a feedback circuit in which the core is set to high voltage and has the task of measuring the potential difference of the DUT to send more significant feedback to the primary control circuit for the correction.

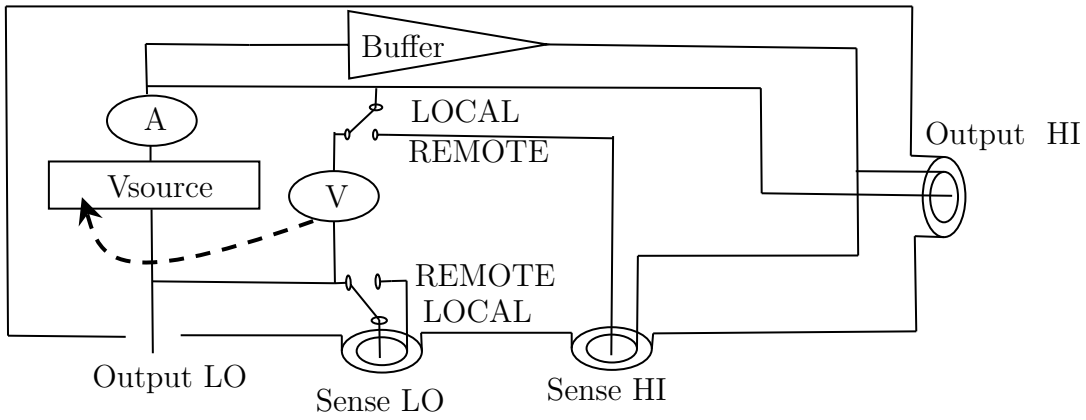

Figure 1.18: *Basic electronic architecture of a keitheley 237*

Keitheley options

The **SUPPLIED VOLTAGE** can vary from -1100V to 1100V at different steps as shown in the table [Ins01]

A **COMPLIANCE** check function is essential to avoid damage to devices due to currents exceeding a certain threshold. Compliance stands for maximum current available for supply, that is, in the case of Vsource I, the measure is the imposed deliverable current limit.

The **INTEGRATION TIME** option concerns the analog to digital conversion when reading data. This option affects the resolution: the greater the integration time, the greater the bandwidth and therefore the better the resolution of the measurement.

1.5.2 Automation of the Keithleys®with Matlab®

MATLAB®(MATrix LABORatory) is an environment for numerical computing that integrates the homonymous programming language. In addition to being a mathematical calculation language, it allows you to interface with other programs or even with instruments equipped with a serial port. We used Matlab together with the Instrument Control Toolbox package to communicate with the available Keithley instruments by automating measurements. Once you have installed the drivers provided by Keithley for Matlab, you have full control of the measures to be programmed, of the processing, of the priority and of the causality in case there are several tools to make the measures. Unfortunately for our Keithley models(237, 2400), Matlab does not provide drivers; we still had access to the communication of the instruments using the SCPI commands on the GPIB communication protocol; in the appendix,I report some Matlab codes developed for simple IV measurements at two Keithleys or night measurements in temperature at three Keithleys in which the K2400 controls the increasing temperature of the detector through a resistance

thermometer and gives the input for measurement IV to two 237 Keitheleys.

The codes used are listed in the appendix B but not explained in detail (as this is not the purpose of the thesis) to leave a trace of them and be available to any reader who needs them.

1.5.3 Scanning Electron Microscope (SEM)

The Scanning Elecron Microscope (SEM) is an electron microscope, that is, it does not use light as a source of radiation but an electron beam generated by an electronic source (a hot Tungsten filament).
This microscope allows analysis of the morphological characteristics of the surfaces on a micrometric scale and is characterized by a high resolution in the scanning of the various objects under examination; although our instrument (Tescan Vega3 XM apparatus located at INFN-LNL) has a good resolution (100nm), there are more advanced technologies that reach resolutions below the nanometer.

The irradiation with an electron beam of the surface to be examined, causes the emission (according to the various dominant interaction mechanisms) of *Auger electrons* (superficial, coming from 1-5 nm of depth with energy 50 - 1000 eV), *secondary electrons* (superficial, coming from 5-50nm energy 0-50 eV), *backscattered electrons* (coming from depths$>$ 100nm, with energy close to that of the 20-30 keV beam) and *characteristic X-rays* (coming from deeper regions $\sim \mu m$ with poor spatial resolution); these electrons (which come from different depths and therefore carry different information) are detected and converted into electrical impulses which are sent to a computer that shows a black and white image with high resolution and large depth of field; The three-dimensional aspect of the image that results in black is given not only by the great depth of field but also by the shadow effect caused by the secondary and backscattered electronic contrast.

The SEM operates in high vacuum (with pressures lower than 10^{-5} Torr) to allow the transmission of the beam (especially for low energy components); the sample must also be conductive (or metallized) and grounded, as the accumulation of charge would not allow its observation.

Chapter 2

Manufacturing processes at LNL

2.1 HPGe detectors built at LNL

An HPGe detector is a thick diode obtained by processing a single crystal of high purity Germanium with a net impurity concentration of $\sim 10^{-10}$atoms $\cdot\, cm^{-3}$, optimized to work with high reverse bias voltages. It is used in large angular coverage spectrometers such as GALILEO and AGATA due to the high spectral resolution in the detection of gamma rays.

Let's begin to presenting the various detectors processed at the Legnaro National Laboratories (LNL-INFN). We started from **planar detectors** because, thanks to their geometry, they are simple and are excellent prototypes for testing both segmentation and PLM diffusion dopant incorporation method. These detectors have high doped contacts, a p + doped face and n + doped opposite face; the contact with doping opposite to the type of the crystal is what constitutes the junction: if the crystal is n-type (p-type) the junction is on the contact p + (n +).The junction can also be divided into several strips by means of a segmentation lithography (see fig.2.6 and section 2.5); the result is therefore the subdivision of the pn junction extended over the whole substrate into various smaller rectifying contacts decoupled from each other by inter-contact-gap. The segmentation will be fundamental in the measurement phase, for the tracking of gamma rays coming from a collimated source through the Shokeley-Ramo theorem [He01]; in fact by associating a fast front-end electronics to the segmented detector it is possible to extract energy, timing and spatial information of the gamma events detected through a pulse shape analysis. The gamma ray trace can then be reconstructed in three dimensions using the Compton scattering formula. These detectors are divided into various classes: that of the Prong, the Head and that of the two strips.

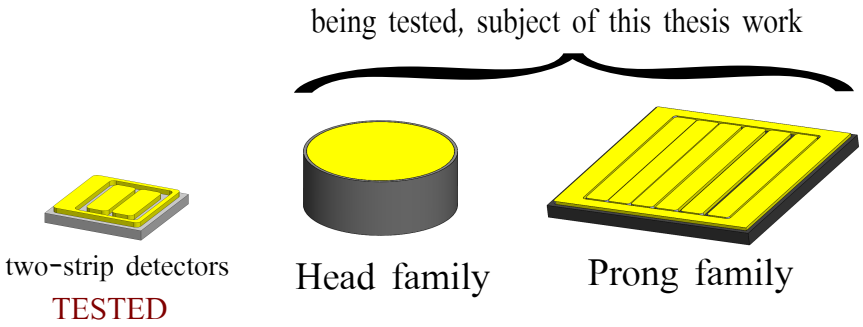

Figure 2.1: *The various families of planar crystals used for the processing of the detectors.*

The figure 2.1 shows various families of detectors processed on the corresponding planar HPGe crystals, which are distinguished by geometry and size; HPGe crystals belonging to the same family are identical copies so it was decided to give a name to each family and an identification number of the crystal:

- The "two-strip detectors" are small prototypes for the first pulsed laser junction tests. They have a square area of $20 \times 20 mm^2$ and 2mm thickness; have already been successfully tested [Ber+21].

- The "Head" crystals are cylindrical HPGe with a thickness of 2 cm and a diameter of 4 cm. Those processed by us are n-types and have been called "Head 23" and "Head 9".

- The "Prong" crystals, on the other hand, are crystals in the shape of straight parallelepipeds with a square base of 35 mm sides and a thickness of 2 mm or 10 mm; they can be p-type or n-type. The "Prongs" processed by us were called "Prong 1p", "Prong 2p" and "Prong 1n", where "p" or "n" stands for the crystal type and the numbers identify the crystals within the type class.

2.1.1 Starting point: small thickness detectors

The small two-strip detector whose junction has been processed with the PLM technique and segmented by lithography (see 2.5) has already been tested and the results are reported in the following article [Ber+21]. This small detector has a surface of $2 \times 2 cm^2$ and thickness <2mm so that it is completely depleted at a reverse bias voltage of about 24V. This depletion voltage is very low compared to that (2400 V) that must be applied to a large volume detector with a tickness of 2 cm.

Starting from this two-strip detector we tried to process another six-strips detector the "prong-1p" from a p-type crystal with a square surface of $34 \times 34 mm^2$

and the same thickness of the previous one equal to 1.6 mm and therefore with low depletion voltage equal to 24-25 V.

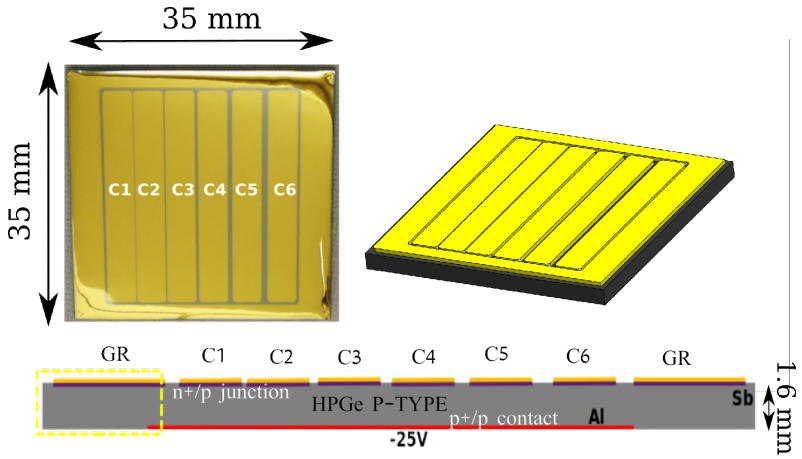

Figure 2.2: *The Prong 1p is a six-segment detector with guard ring, of dimensions* $35 \times 35 \times 1.6 mm^3$*; it is manufactured starting from a p-type crystal and has a segmented n + / p junction with antomonium doping.*

I will limit myself to reporting some summary results regarding the Prong 1p tests as my thesis does not concern the acquisition measurement or the pulse shape analysis, but the construction process, the optimizations and the reverse IV tests (diode measurements) for large volume detectrors. The results shown in the figures are only for the purpose of illustrating the success of the PLM technique for the construction of low thickness HPGe detectors and all the details on the acquisition in detector mode can be found in the article [Ber+21].

The figure 2.3 shows that the reverse bias, the leakage current that is too high for the C5 segment does not allow the acquisition of gamma events with a front-end electronics; we must therefore be sure that all segments do not breakdown. at full volume depletion voltage with a measurement in diode mode. The figure 2.4 shows the calibrated spectrum of 133Ba acquired by the various segments of the Prong 1p detector.

The good results regarding the processing of the small 2-strip detector and the Prong 1-p has motivated us to extend the techniques for large planar detectors and to analyze all the problems related to manufacturing processes trying to solve them through various optimizations. The various steps for the manufacture and the segmentation of the junction through lithography, will be discussed in the following sections and in general are common to all detectors, including those already tested. The optimizations described in the next chapter refer to the problems encountered in the processing of detectors with greater thickness which therefore require much more reverse polarization voltages to be depleted.

Once the study on planar detectors is finished, all the results and procedures

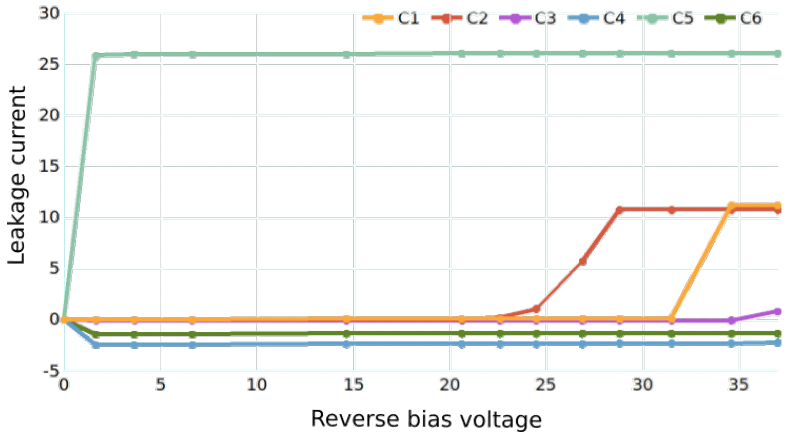

Figure 2.3: *Prong 1p:the measurements in detector mode taken in reading by a preamplifier of the front-end electronics, show leakage currents too high for the C5 segment which therefore failed in the processing*

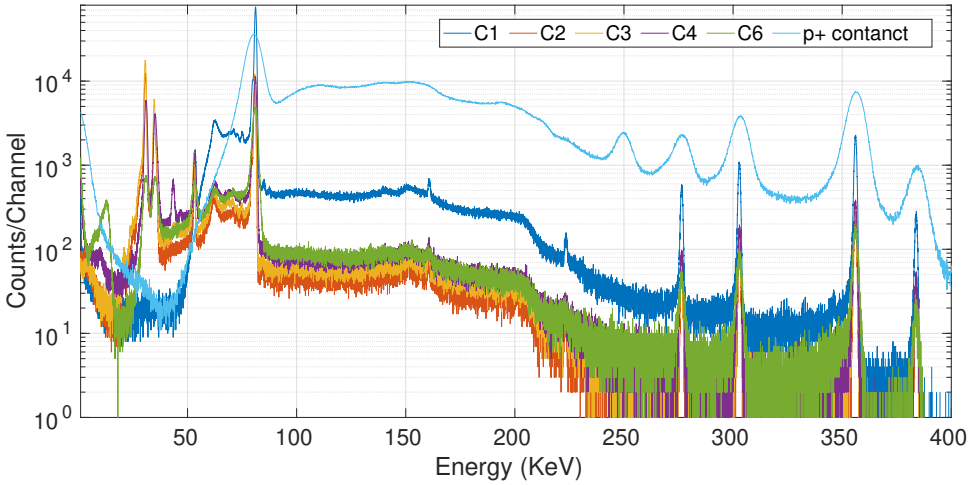

Figure 2.4: *Calibrated gamma-spectrum taken for an uncollimated ^{133}Ba source acquired by five segments and the p+ contact of the Prong 1p detector.One of the six segments (C5) is not reported as it failed in construction showing a breakdown at very low voltages*

obtained can be applied detector with different geometries, with appropriate modifications.

2.2 Summary of the Manufacturing

The process of building HPGe detector starts from a hyperpure germanium crystal and develops into a sequence of chemical-physical processing.

The primary purpose is to create an optimized junction to operate at high reverse polarization voltages, through two main steps:

- deposition of p (or n) dopant on the n-type (or p-type) HPGe substrate by sputtering
- pulsed laser treatment of the substrate, in which the dopant layer is deposited, for the formation of the rectifying p+/n (or n+/p) contact.
- pulsed laser treatment of the opposite face in which a n (or p) dopant layer has been previously deposited on n-type (or p-type) HPGe surface.

Once the pn junction has been processed, it can be easily segmented through a lithography process. The simplicity of the segmentation process derives from the fact that the junction is very tight and therefore can be removed in the contour lines of the strips to be decoupled. As for segmentation lithography, a wet etching solution is used which generally consists of two components: one component oxidizes the germanium and the other removes the oxide. The lithography process is schematized in the figure and consists of the following steps:

- Metallization of the junction through a deposit of a gold layer;
- deposition of the photorestist with spin coating techniques and irradiation with UV rays through a lithographic mask.
- Development of the photoresist through a developer (Tetramethylmmonium hydroxideTMAH)
- gold etchant for the removal of the gold strips in correspondence of the gaps.
- removal of the resist with acetone.
- segmentation etching with $HF(65\%) : HNO_3(40\%)$ (1: 3) solution, in which the gold strips not previously removed prevent the removal of the junction below.

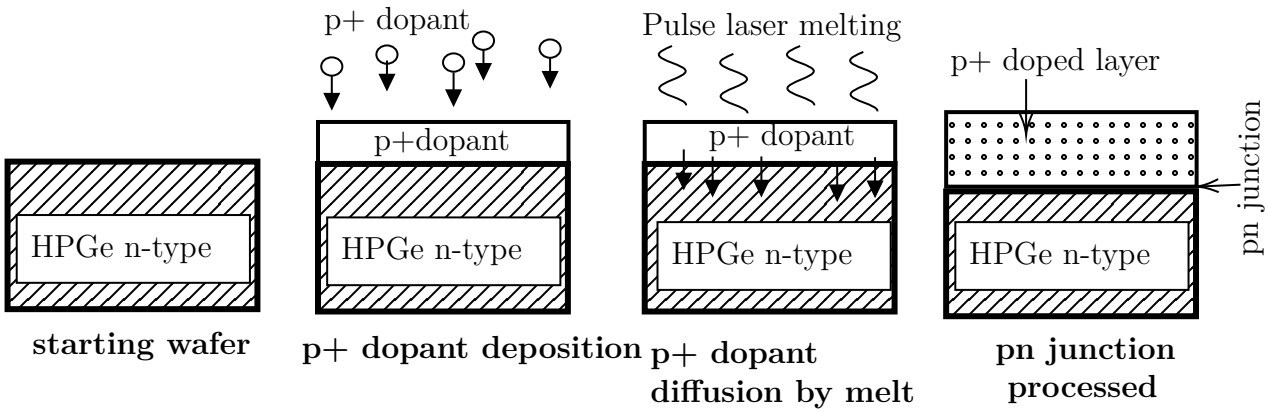

Figure 2.5: *From right to left: processing of the pn junction from an HPGe planar crystal; the same process is used to create n+ contact on the opposite side.*

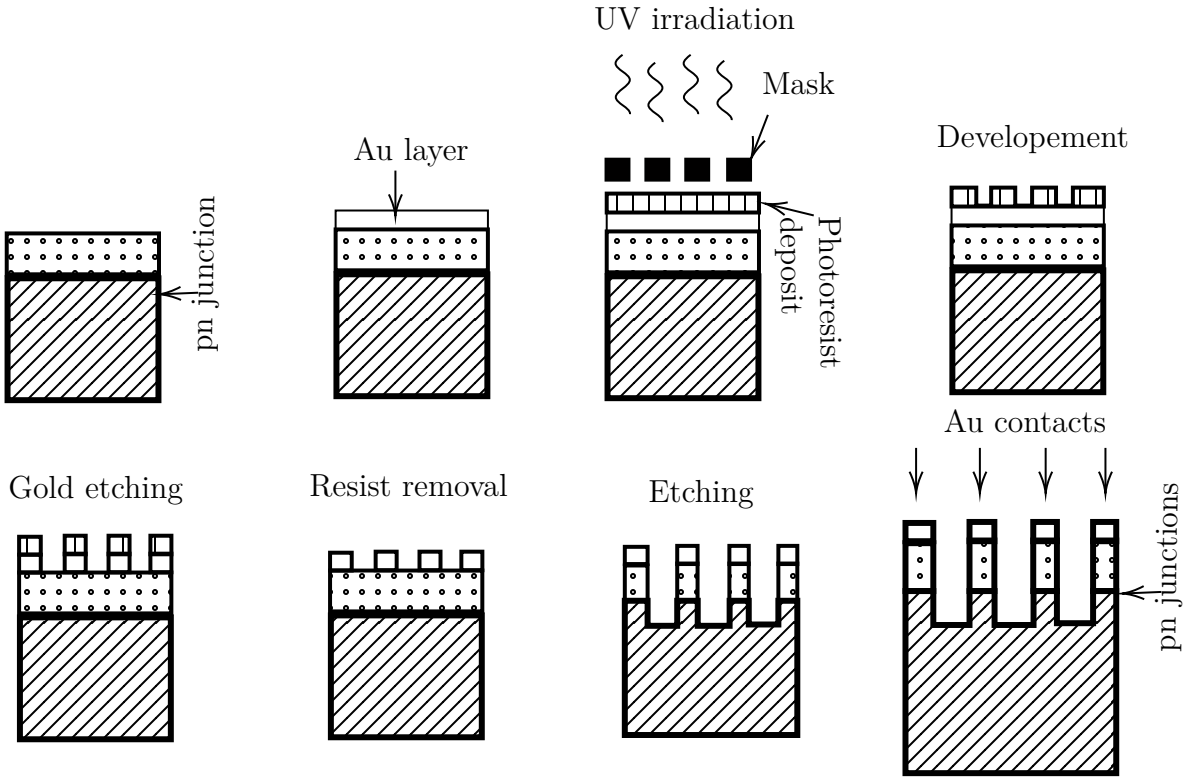

Figure 2.6: *From right to left and from top to bottom: sequence of lithographic processes for the segmentation of a previously processed junction.*

2.3 Preparation of the crystal surfaces

2.3.1 Lapping

Lapping is the first physical process that the crystal undergoes. It consists in rub-

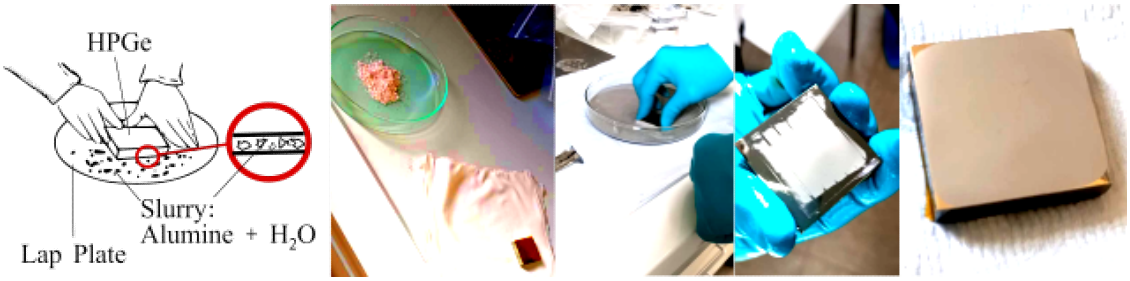

Figure 2.7: *Various steps of the lapping process*

bing the surface of the semiconductor crystal by hands on a plate with an interposed abrasive, usually a slurry of Alumina (Al_2O_3) and water, in order to reduce the curvature of the surface or to remove any previous doped layers on the crystal.

The alumina used to perform the lapping has a grain size of 3 μm, high mechanical strength and high density. The figure 2.8 shows some SEM images at various magnifications of a lapped HPGe surface and a scan with a profilometer stylus to quantify the roughness ($\sim 2.8 \mu m$)

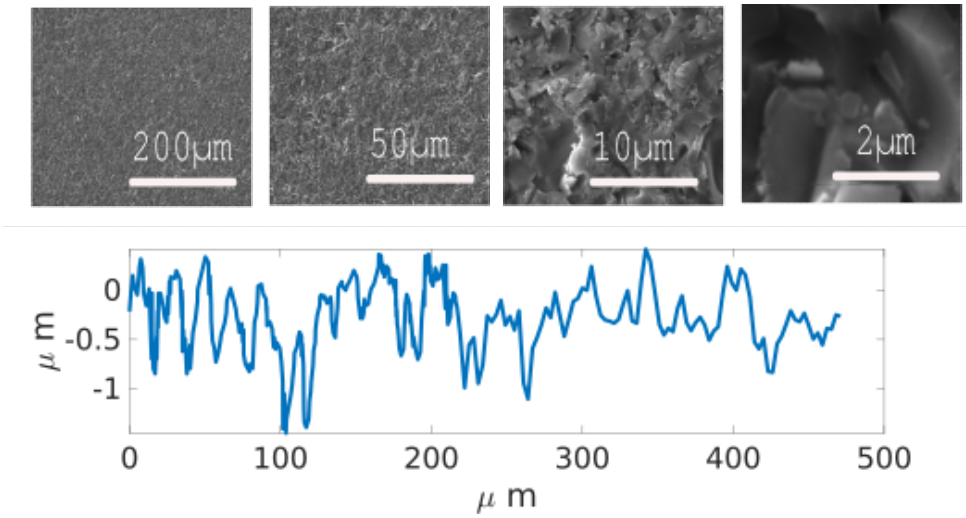

Figure 2.8: *SEM images of HPGe crystal surface lapped at various magnifications and a roughness profile measured with a stylus profilometer*

2.3.2 Etching

The lapping procedure does not fully remove the damage from the crystal, usually it is considered that a damaged layer from 3 to 10 times the grain of the used slurry remain, depending on the material. Moreover the surface has an high roughness as can be deduced by the opaque aspect. (inserisci foto campione as lapped). For this reason an etching step is added after lapping. After the lapping treatment the surface is very rough, typically a few micrometers (see Fig 2.8). At this point a wet etching is used to relieve the crystal surface from their tense state For this reason, a wet etching of $HF(65\%) : HNO_3(40\%)$ (1:3) solution is carried out which reduces the roughness but on the other hand.However, it changes the curvature drastically as shown in the Figure 2.9 which shows the variation of the global profile of a lapped surface subjected to a 3-minutes$HF(65\%) : HNO_3(40\%)$ (1:3) etching[Sch67]. The measured Removal Rate for this type of etching is $17\mu m$ per minute and is compatible with the value reported in the literature.

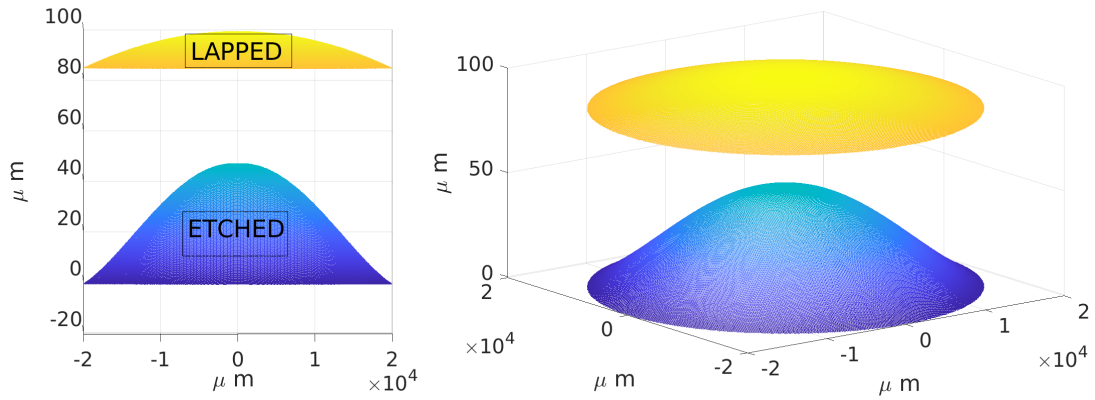

Figure 2.9: *Evolution of the curvature of a lapped surface for a crystal of the Head family, subjected to* $HF(65\%) : HNO_3(40\%)$ *(1:3) etching for 3 minutes.This reconstruction was made by fitting the profiles measured along the diameter of the detector. The relative height between the surfaces is a rough estimate obtained by measuring the real mass loss and comparing it with the theoretical one calculated from the profiles.*

2.4 Junction processing (general scheme)

Theoretically, a junction is schematized by putting two pieces of semiconductor of different types in contact. In practice, however, there are no pieces in contact, but one of the surfaces of the starting crystal is converted into an opposite type semiconductor with respect to the bulk. As already mentioned in chapter 1, we used the PLM technique for the creation of the pn junction in which among the advantages in the construction phase, the ease of segmentation certainly stands out as the junction created with this technique is ultra-thin. The creation of the junction takes place through a pulsed laser treatment of a surface that has been previously prepared as described in the chapters, and on which a doping layer has been deposited; in the next paragraph I describe, among the various deposition methods, the sputtering technique we used.

2.4.1 Dopant deposition

Physical Vapor Deposition (PVD) is a very popular technique for the manufacture of electronic devices used for the deposition of thin films (with a thickness of the order of microns or nanometers) under vacuum on substrates. In processes (PVD) the material to be deposited is evaporated from a solid or liquid source in the form of atoms and transported in vapor form through a vacuum or plasma environment to the substrate where it condenses. Generally PVD is used to create layers of a few tens or hundreds of nanometers, for multi-layer deposits. PVD methods are divided into:

1. **Sputtering**, in which the material to be deposited is eroded by a plasma (powered by direct current or radiofrequency);

2. **Thermal evaporation** in which the Joule effect plays an essential role;

3. **Electron gun**, in which a beam of electrons strikes the material, losing its energy and locally heats the material to be evaporated;

4. **Arc evaporation**, in which evaporation is produced by a direct electric discharge on the material;

5. **Pulsed laser deposition**, in which a high-powered laser vaporizes the material from the target.

The atoms in the gaseous phase, before depositing, travel in a straight line until they collide with a molecule of the residual gas; to reduce this effect it is essential to obtain a high average free path, reducing the gas pressure.

The PVD deposition of the dopant on HPGe used by us is with the sputtering method; in this process the dopant is vaporized through a physical sputtering from

a surface called target (non-thermal vaporization): the surface target atoms of the doping material are physically torn from the target surface by means of the energy transferred to them by a bombardment of ions. These ions are created by low pressure plasma (less than 0.1 Pa) and in this case the extracted particles have a high average free path between the source and the substrate. Furthermore, the plasma fills the entire region between the source and the substrate and is made up of inert gas (Argon).
Regarding the processing of the p +/n junction, the deposition of p-type dopant on the n-type HPGe substrate is a multylayer consisting of an underlying 2nm thickness of aluminum coated with a 4nm amorphous germanium thickness. From now on we will refer to this configuration as "a-Ge/Al 40/2 process" or simply "40/2 doping procedure" or "40/2 recipe" (see Chapter 3.1). The underlying contact n + / n on a crystal (n-type) is processed with the PLM technique by depositing antimony. This contact does not play a role until the entire detector is fully depleted with an adequate reverse bias voltage.

2.4.2 Manufacturing of the junction

As already extensively described in section, after the deposition the surface is subjected to a pulsed laser treatment for the creation of a junction. In this paragraph I will show how it is practically done. Since a pulsed laser spot has a size of $5 \times 5 mm^2$, to cover the entire surface of a detector (previously covered with a dopant layer) it is necessary to introduce an overlap between the spots (0.4 mm), to ensure that all parts of the surface are processed. Figures 2.10 and 2.11 show a visual inspec-

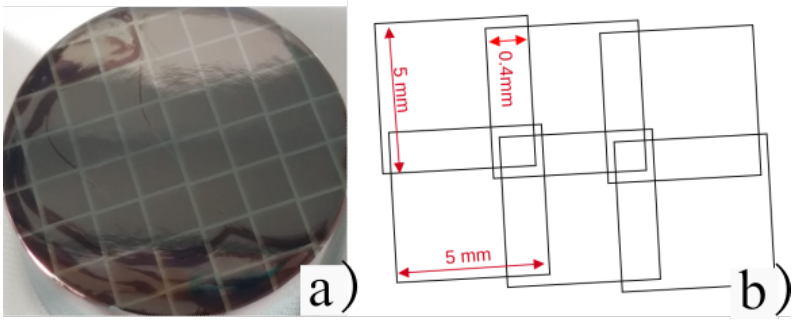

Figure 2.10: *Visual analysis of the treated pulse laser surface (a) and schematization of the overlapping pattern of the laser spots (b). There is a tilt angle of about 2 ° between the upper side of the square spot and the translation axis parallel to the surface; this angle was measured starting from the SEM images.*

tion and SEM images of the surface treated with the pulse laser respectively; we note from the SEM images a tilt angle of about 2 ° between the upper side of the square spot and the translation axis was measured. The investigation of the fol-

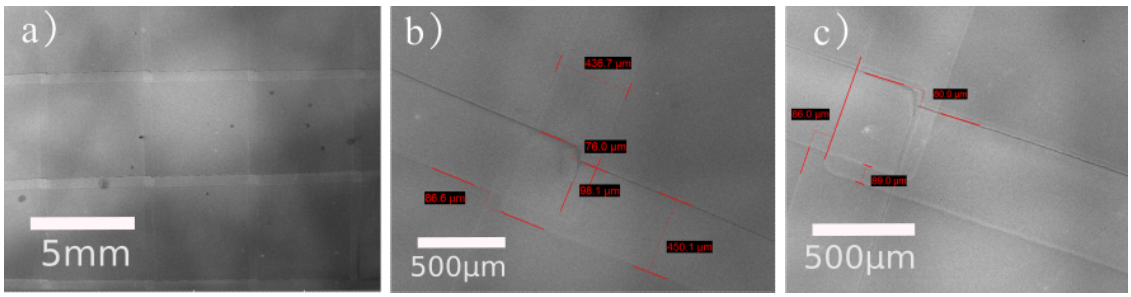

Figure 2.11: *SEM images after pulsed laser treatment show the pattern of overlapping spots covering the entire surface (a); the correspondence of the overlapping region of four spots, a tilt angle of the spot with respect to the translation axis between one spot and the next is highlighted (b)(c)*

lowing chapters will be aimed at analyzing the role of the edges of the spots, both morphological and in the electrical characteristics of the inversely polarized diode.

Overlapping spot configurations will be processed and characterized, but also with contacts on single separate spots.

2.5 Photolitography (junction segmentation)

Once the junction has been created, it can be segmented through a series of chemical processes, covering the parts not to be removed with certain layers of material inert to the segmentation etching, leaving the parts to be excavated uncovered. Note that the junction is a few hundred micrometers deep and to be sure of the removal in the desired areas, it is necessary to know the excavation speed or removal rate (RR) of the etching.

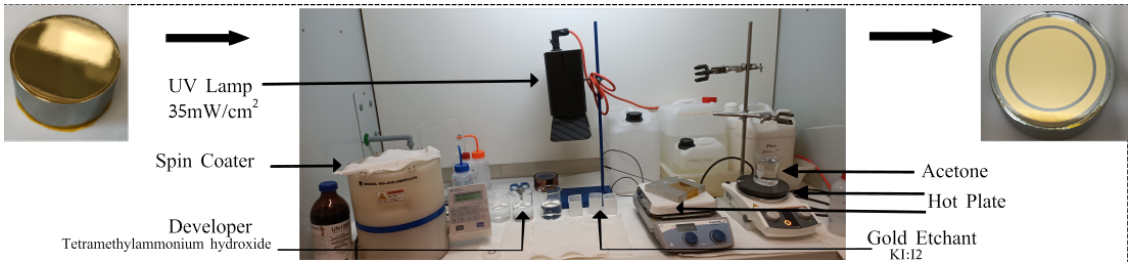

Figure 2.12: General apparatus for lithography. On the top left, the starting crystal (in this case a Head 9) to be lithographed, top right, the final result

Photolithography is a technique consisting of a set of processes, which allows the selection of the surface regions on which to perform appropriate treatments and mask those that must be preserved in the processing. In our case it allows to dig and remove the junction only in selected regions, the so-called gaps, which will separate the final strip junctions from each other trough the transfer of a mask design on the wafer surface as a relief image. The materials used are: photoresist, mask, UV lamp, developer, gold etchant.

The **photoresist** is a light-sensitive polymer, which is exposed through a mask to UV light and developed into a relief image with side walls through the thickness of the resist. This allows to select the regions to be protected, covered by the reisist, and the regions to be etched, not covered by the resist, to select the strips in a subsequent development of the design on the germanium substrate.

The fundamental processes can be summarized in the following steps phases: surface preparation, photoresist spin coat, prebake, exposure,postbake and development.

As an example for the following various procedures, I show the processing of a planar n-type Head 9 which has been segmented to obtain a central Pin surrounded by a guard ring for the collection of lateral leakage currents. However, the segmentation process is universal and is applied in the same way to obtain more segments

as shown in the figure 2.16

2.5.1 Surface preparation

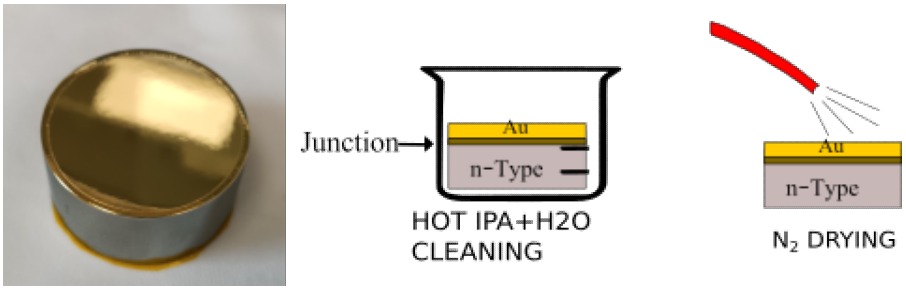

The preparation of the surface on which deposit the resist is fundamental both to improve adhesion and to avoid contamination that can propagate in the subsequent steps and therefore in the final result. Particulate contamination results in defects in the contour line of the pattern, while liquid contamination such as oils or water residues cause poor adhesion of the resist on the substrate.

So proceeds with the chemical-physical cleaning of the particulate contaminant:

- Bath in hot IPA and hot H_2O rubbing with sweb.
- Then the film of liquid contaminants is removed by blowing N_2 through a tube and checking that the surface is dry.

2.5.2 Spin coat

The spin coating is a dynamic process of deposition of the resist which allows to obtain a homogeneous and uniform film on the substrate. It is dynamic because the wafer rotates during deposition and centrifugation allows the resist to be spread well on the substrate. The control of the parameters involved is important for the control of thickness and homogeneity. It is possible to choose between speed, spin times and acceleration depending on the photoresist used. Although there is a theory on the deposition of the resist by spin coating, there are random parameters such as temperature, air humidity, vibrations due to the non-alignment of the rotation axis and therefore also the geometry of the sample, which involve a non uniqueness of the process and therefore the determination of these parameters must be done experimentally in the laboratory in a real recipe based on the result obtained.

Various tests were performed to determine the optimal parameters. The steps can be summarized in the following steps:

- Cover the face not to be processed with kapton tape
- Blow the exposed surfaces with N_2 to eliminate any residual contaminants

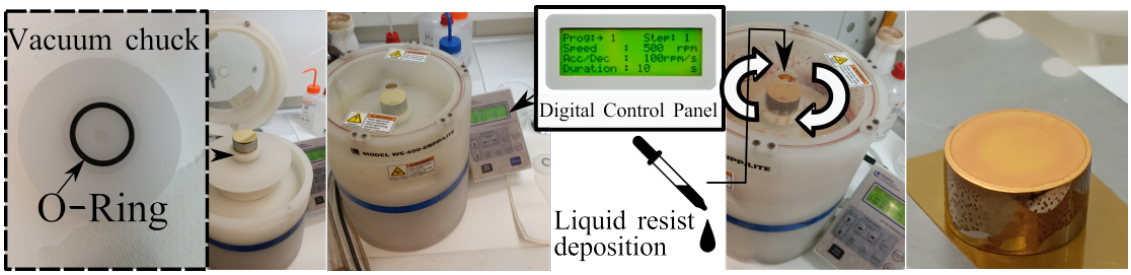

- Spinning 0.3 ml of photoresist, in our case Microposit S1813, on the surface to be processed. This substrate is the one corresponding to the junction and is covered with gold; the gold covering is fundamental for the lithography as will be seen later. Avoid bubble formation during resist deposition.
- The optimal result is obtained by spinning at 500 rpm 5 sec and then reaching 4000 rpm in 40 s with an acceleration of less than 3000 rpm / s

2.5.3 Softbake

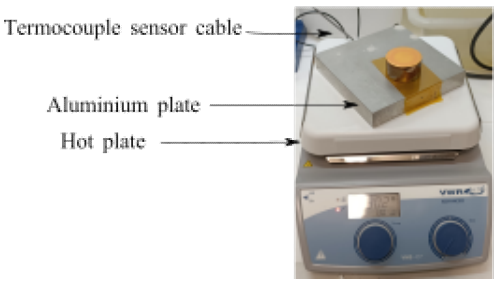

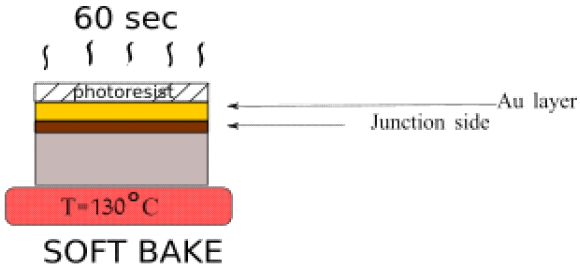

After deposition of the resist by spin coating, the solvent contained in the resist (15-40 %) is reduced by means of a soft bake. The drying of the resist gives more stability to the deposited film which would otherwise deform during UV exposure due to evaporation of the solvent. The positive effects of softbake are certainly the thinning of the resist film, improvement of adhesion on the substrate, hardening of the film which becomes less subject to external contamination and improvement of the quality of the contour lines, since only about 5% of solvent remains near the substrate. Unfortunately, on the other hand, the photoactive compound (PAC) begins to degrade at high temperature and the resin that makes up the resist crystallizes or oxidizes at high temperatures. It is obvious that the optimal process must be established through many tests:

- heating for 60 seconds on a hot plate at T = 130 ° with kapton on the side not processed

- cool the unprocessed surface with N_2 flow

2.5.4 UV Exposure

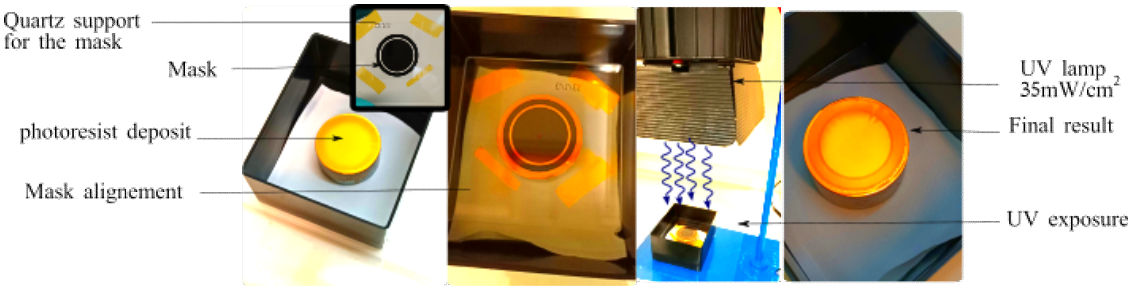

The exposure of the positive photoresist to UV radiation causes a change in the solubility of the exposed parts which will then be easily removed with a developer. This is the principle by which the pattern is transferred from the mask to the substrate of the wafer by means of a photoresist. This happens because the PAC, insoluble in developer solution, becomes soluble if exposed to UV of the wavelength 350-400nm because it is converted into carboxylic acid by exposure. The unexposed part, on the other hand, remains insoluble. An undesirable effect of UV exposure is the so-called standing wave effect. Since the gold substrate is reflective, the monochromatic light that penetrates up to the substrate is partially reflected, and this involves an interference between incoming rays and reflected rays that form a pattern of high and low intensity standing waves across the thickness of the resist . This phenomenon is very important if we are dealing with small resist layers (comparable to the wavelength of the pattern) but in our case the thickness is large enough to ignore this effect. Summarizing the steps:

- Aligning the mask: Place the mask on the substrate through a quartz of area 2x2 cm^2.The quartz layer will serve as a support to the mask, keeping it rigid and well pressed to the photoresist substrate. Quartz is optimal because it is UV transparent
- Cover the sample not involved in the process with a shutter
- The printed side of the mask must be in contact with the resist, to avoid errors in the resolution of the contours

2.5.5 Developement

Development is one of the most delicate processes in lithography. The interaction between developer and photoresist affects the shape of the resist profile and the line width. After exposure, as already mentioned, the exposed resist parts have

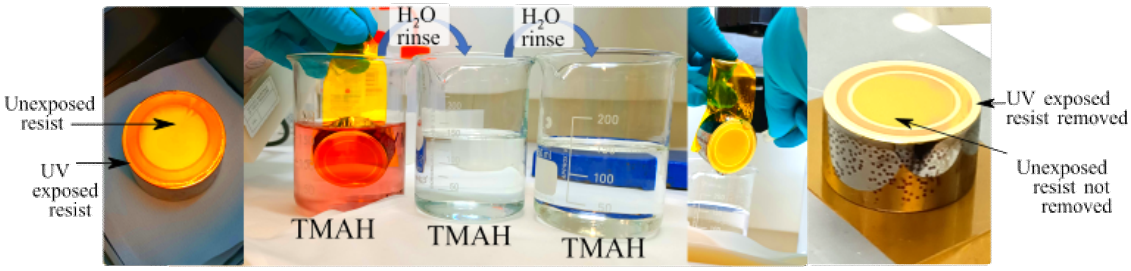

become soluble and must be removed with a developer while the unexposed parts remain unaltered and will result in the relief reproduction of the mask pattern. The solution used for the removal of the exposed resist is called developer, in our case the TMAH (tetramethylammonium hydroxide). Various baths are made to avoid residuals of resist remaining in the unwanted areas. The deed processes be summarized as follows:

- cover with another layer of kapton the unprocessed surface, already covered by the previous layer of kapton. This avoids any contamination of resist deposited on the previous kapton layer.
- Immersion of the crystal in three TMAH baths for 60 seconds each. Rinse with water between one bath and the next to eliminate any contaminants that, in suspension in the developer, may have deposited on the sample.
- Hot water cleaning and drying with N_2

2.5.6 Post bake PB

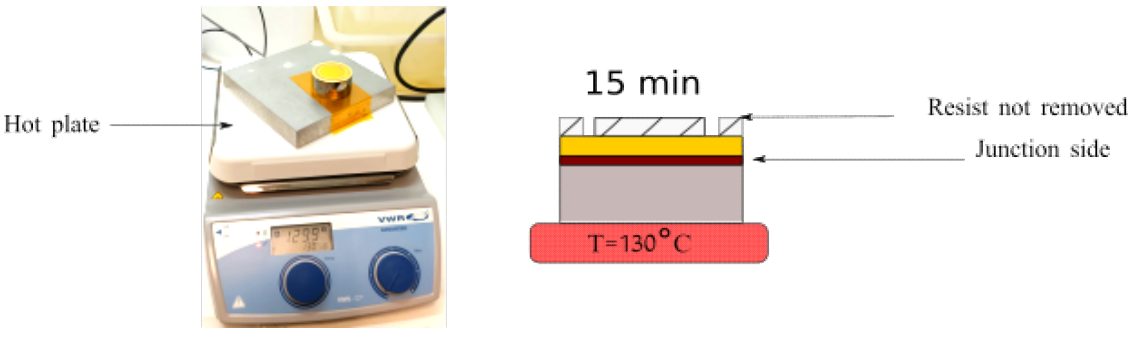

A PB after development is necessary to harden the resist image through the crosslinking of the resinous polymer contained in it, at temperatures of about 130

°, making the image more stable for the subsequent process. At this stage the following processes are required:

- Removal of the double Kapton layer
- Heating the sample at 130 ° for 15 minutes, placing a layer of kapton between the hot plate and the crystal, sticking it to the plate itself

2.5.7 Gold etching and removal of the resist

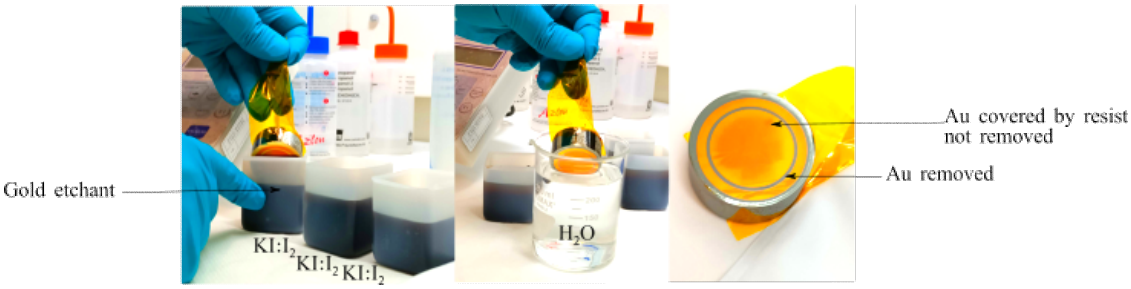

Once the image is reproduced through the resist, it must be transferred to the germanium-doped substrate to create the strips, surrounded and isolated by deep gaps in which the junction is removed. It is at this point that the gold layer, not covered by the resist, plays a fundamental role. In fact, what we have now obtained is a photoresist reproduction in relief of the design printed on the mask; this reproduction is placed on the gold layer that covers the junction. The next step is to transfer the photoresist design onto the Au layer where it is placed. To do this, a gold etchant is first used to remove the uncovered parts of the gold layer, then the resist (which covers the gold layer) is removed in a acetone bath. Once the photoresist that covered the gold layer has been removed, what you get is a gold reproduction of the pattern originally printed on the mask

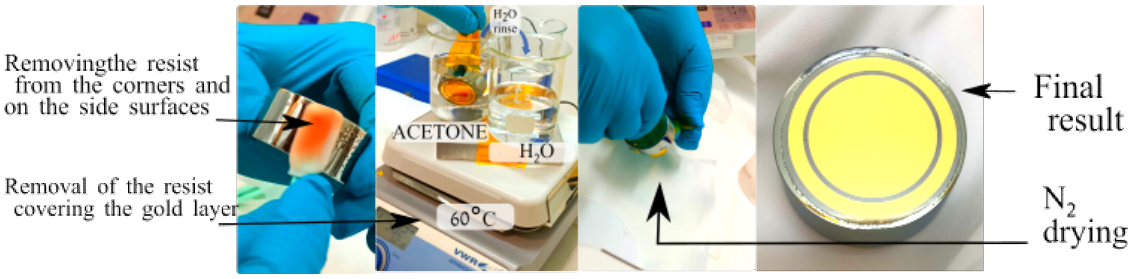

The steps to be performed are as follows:

- Three baths of gold etchant are needed, in our case KI-I_2, for at least 20 seconds each. This is done by supporting the sample with kapton scotch tape, rinsing with water at the end of each bath and drying with nitrogen at the end of the procedure.
- remove photoresist deposits on the edges of the sample with an acetone-soaked swab
- Kapton tape removal, three hot acetone baths (40 ° -50 °) to remove the resist, cleaning in hot water and IPA and drying with N_2 flow
- If Al on the p side, 10 second on HF 10% and hot H_2O bath and dry.

2.6 Ge etching & passivation

At this point we want to remove the junction between the outer ring (guardring) and the central circle to decouple the two contacts. This is the process of creating the gap, and it consists in etching the parts of germanium not covered with gold through a etching of $HF(65\%) : HNO_3(40\%)$ (1:3) until the complete removal of the junction.

The Removal Rate (or etching speed) accordig to literature is 17 $\mu m/min$ so, being the junction 200-300 nm thick, even 1 minute of etching would be enough.

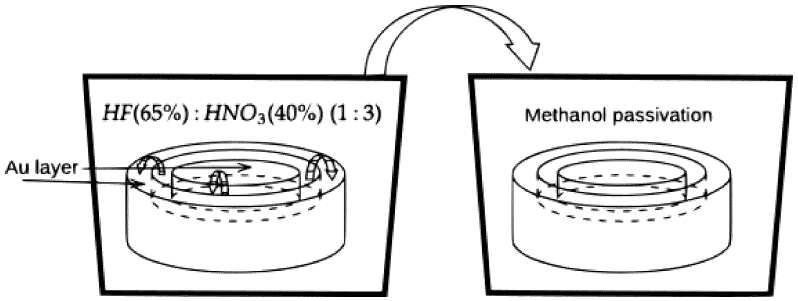

Figure 2.13: *Segmentation etching followed by passivation in methanol; in this phase the material is removed from the area not covered with gold, decoupling the guard ring from the central circular contact*

To be sure of the result, we proceed with a germanium etching of 3 minutes for a total excavation of 51 μm The following steps are to be followed:

- p+/p or n+/n side kapton covering
- $HF(65\%) : HNO_3(40\%)$ (1:3) etching (t>3min)
- methanol quenching

The finale step of methanol quenching produce a carbon containing layer that is demonstrated to passivate the surface of the germanium. These means that the surface not covered by gold and by the contact does not have a reduced amount of surface traps that bring to a low charge accumulation and low surface conductivity [Mag+15].

It is therefore important to stress that this simple double step process (etching plus methanol quenching) allows to reach two distinct and relevant aim: the removal of the junction from the segmentation region and the passivation of the segmentation region and lateral surfaces.

We will see in the following that despite of the semplicity of the process, some improvement of the procedure has to be adopted to perform a better segmentation.

2.7 Final remark

In this chapter I have illustrated the techniques used at LNL for the processing of an HPGe diode optimized for operation as a detector. Some of these processes have been optimized gradually, based on the results that were obtained and I will talk about these optimizations in the next chapter. Although I have described lithography for the segmentation of the junction in the particular case involving the creation of a central circular contact and a concentric guardring on a cylindrical HPGe, this procedure is generally used for any type of segmentation in relation to the design on the mask. The general procedure is illustrated in figure 2.16.

As other examples shown in the figure 2.14 are the main steps for the creation of contacts on single separate spots in the processing of the prong 1n crystal and in the figure 2.15 a photo of a 6-segment detector with a concentric guardring is shown .

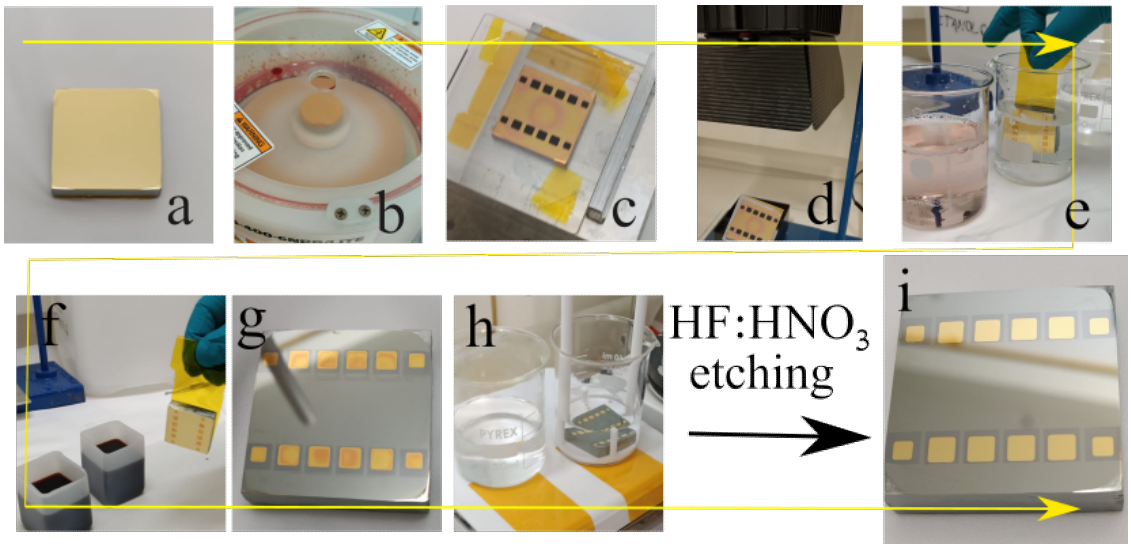

Figure 2.14: *Main phases of the lithographic process for the segmentation of the Prong 1n: metallization of the p + / n junction with gold layer (a); deposit of the resist by spin coating (b); mask alignment (c); UV irradiation of the sample (d); development of the resist in TMAH; removal of gold not covered by the resist with gold etchant (f); result after gold removal (g); removal of the resist with acetone (h); result after the first segmentation etching (i);*

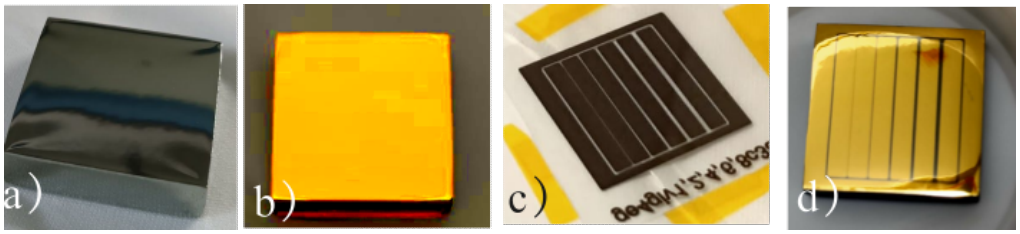

Figure 2.15: *Four symbolic phases for the processing of a six-segment Prong crystal: starting crystal (a); creation of the junction and metallization (b); printing of the mask for the segmentation (c); final result (d)*

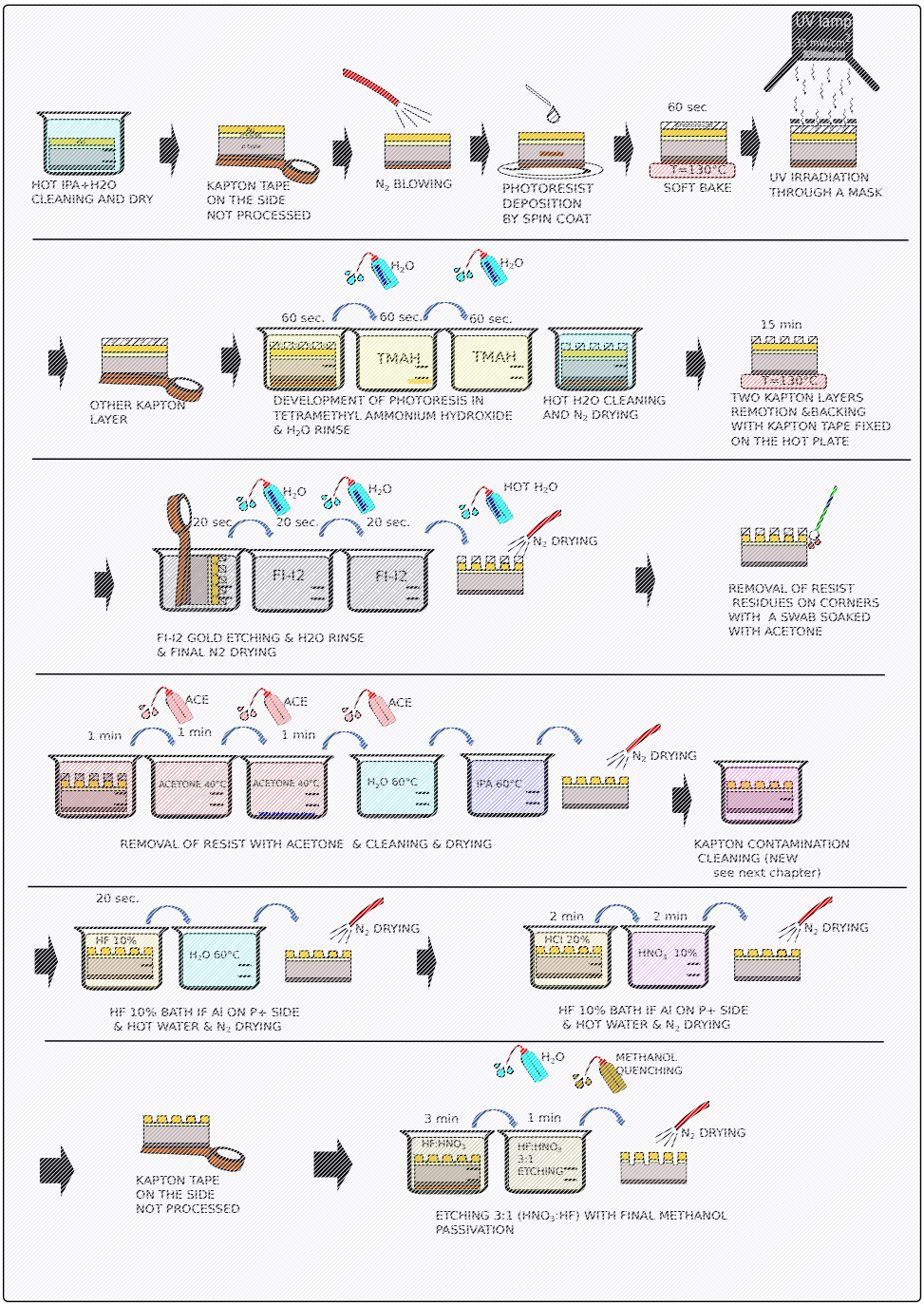

Figure 2.16: Detailed step by step diagram of the lithography process implemented at the LNL of Legnaro for a Prong p-type detector

Chapter 3

Junction processing & optimizations

The following chapter focuses on the methods used to process junctions on HPGe substrates and their optimization for operation at reverse bias voltages. The processing of a junction essentially takes place in two fundamental steps: the deposition of the dopant on the HPGe surface and the subsequent doping by means of a pulsed laser treatment of the same surface; As far as deposition is concerned, two procedure of dopant deposition were tested; these procedure vary according to the type of the junction to be processed. For a p + junction obtained by doping HPGe with aluminum, we decided to use a deposited aluminum layer covered with another layer of amorphous germanium to avoid problems related to ablations on the substrate and oxidation of the dopant in the various pre and post laser melting; the n + junctions, on the other hand, were processed using antimony as dopant, first deposited on a p-type HPGe instead of the lithium with which these junctions are made in conventional n+ jucntion fabrication. Lithium is an element with relatively high diffusion in solid matrix. Lithium diffusion produce thick junction at temperature of 300°C that are low enough to avoid HPGe contamination; it presents other problems including stress of the crystal structure of germanium and significant thicknesses of dead layers where charge collection does not occurs. Moreover, Lithium may diffuse under annealing used to remove radiation damage and theretofore Lithium junction may lose performances. Sb introduced by laser annealing instead, has a negligible diffusivity in solid below temperature as high as 600°C [BB08] and is very stable after incorporation [Bru+10].

3.1 Optimization of a P+ junction on N-type substrate

The procedure for the realization of the p + junction with PLM methodology was progressively developed by the research group of Unipd in collaboration with our LNL-INFN group of Legnaro. The basic idea for the realization of p+ laser annealing procedure is protected by an Italian patent 102020000008662 of UNIPD and INFN.
In order to illustrate the patent and the various optimizations in progress, consider figure 3.1 in which the two main deposition processes of doping Al for the formation of the p + / n junction are schematized; the processes analyzed are divided into: 4nm of Al deposited on n-type substrate (a); 40nm of amorphous Ge on 2nm of Al on n-type substrate (b);

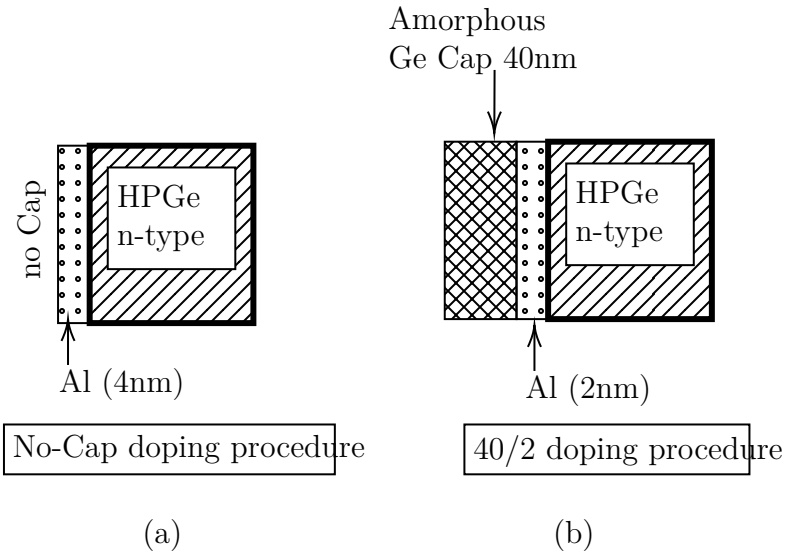

Figure 3.1: *Two configurations of deposited dopant layers prior to pulse laser melting for the creation of the p+ junction. The 40/2 doping procedure deposit was subsequently optimized to 10/4 procedure.*

The direct lasing of an Al source (fig.3.1(a)) exposed to air produce inhomogeneous junction with surface detrimental effects as ablation and roughness. These effects are shown in the SEM image in figure 3.2 (a) and are confirmed by a SIMS measurement (fig. 3.2 (b)) which highlight non-homogeneous aluminum concentrations on various regions of the substrate with high presence of oxygen.

According to the patent most of the drawbacks are improved by depositing an amorphous Ge layer (cap) in rapid sequence of the Al source without vacuum braking in the sputtering chamber (fig.3.1(b)). The amorphous layer separate the Al from the external atmosphere reducing the interaction of Al with oxygen.

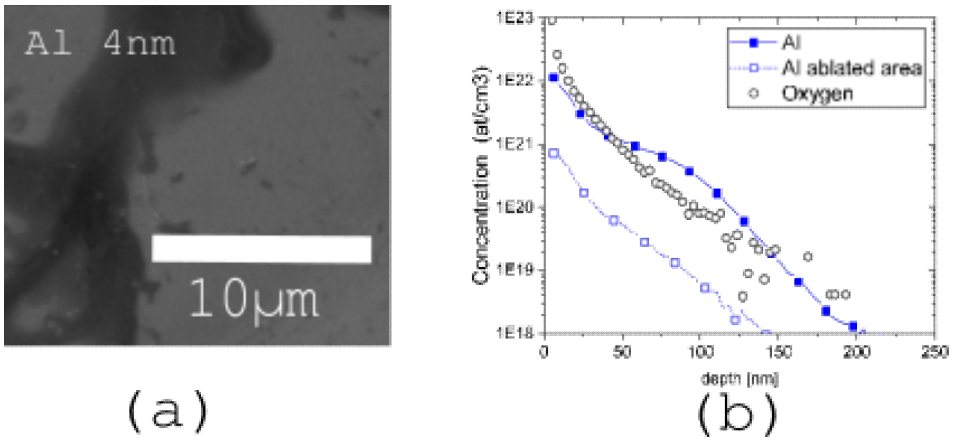

Figure 3.2: *The lasered surface with 4nm of Al deposited shows ablations and roughness confirmed by SEM scans and SIMS measurement with significant oxygen contamination*

Optimization of such process is one of the focus of the thesis work of my collegue Pietro Argenton, here I report some results I contributed to obtain in order to explain the the structure of the processes performed on the detector prototypes that I tested in my thesis with the aim of investigating the possible effect of process optimization on the detector performances.

After the pretreatment of the substrate, the dopant was sputtered at the LNL, the detector was brought to Padua for pulsed laser melting (Fig.3.3) and then returned to the LNL for the subsequent phases (possible segmentation, passivation) and the final IV measurement. Using aluminum for doping and processing the p + junction on an n-type crystal, the doping process was optimized through surface characterization techniques concerning morphology (profilometer, AFM, SEM), impurity depth profiles (SIMS) and active dopant concentration (Vdp-Hall)

Before processing the junctions on a detector, an analysis of the lasered spots was carried out on a test resistive germanium wafer, for an overall characterization. In particular, we proceeded to make an array of 3x5 spots for the Al samples (4 nm) and an identical array with the same number of spots for the Al / a-Ge deposit (2nm/ 40nm).

From a first visual analysis it was seen that the no-cap samples, after the PLM, show some stains and many irregularities; Instead, the cap samples have a very regular surface, and in the 40/2 procedure the spots are darkened and distinguishable by eye from the rest of the non-laser substrate.

From a **profilometer analysis**, the Al/a-Ge 40/2 doping process on samples shows peaks of height 200nm on the edges of the pulsed spots with aspect ratio

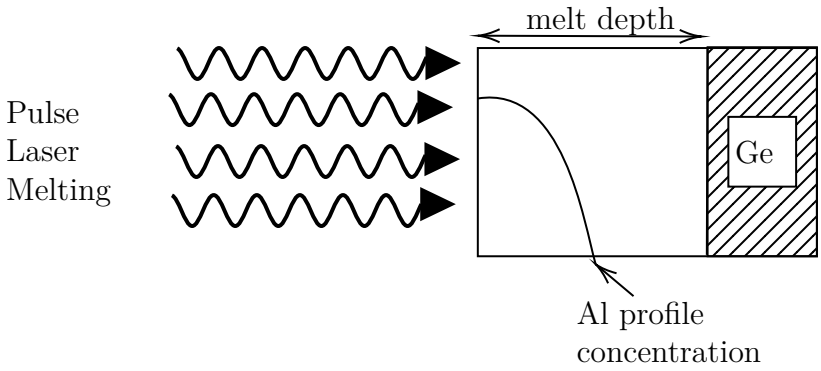

Figure 3.3: *Schematic process of incorporation of the previously deposited dopant, the concentration of which distributes on the melted thickness induced by a pulsed laser treatment (PLM)*

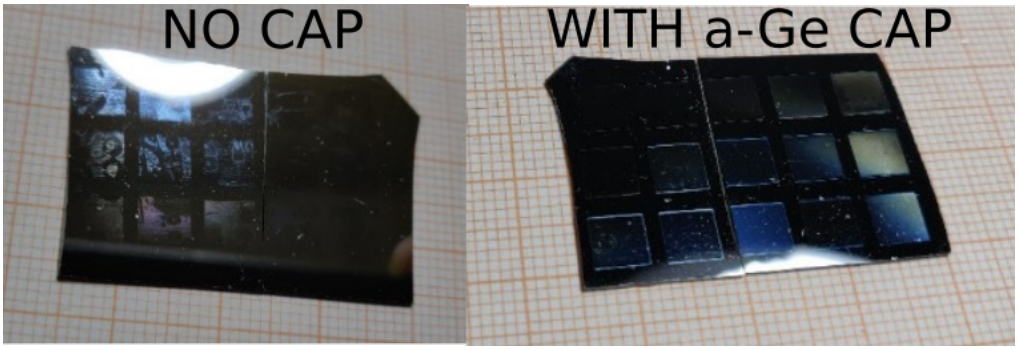

Figure 3.4: *Visual inspection of the test spots after the PLM treatment (500mJ/cm^2); left: pre-PLM deposited aluminum is not covered by amorphous germanium cap; the spots have many irregularities after laser melting. Right: the 2nm aluminum is covered by a deposited 40nm amorphous germanium layer; after the PLM treatment the spots are fairly uniform in appearance.*

$d/l = 0.02$ (see fig.3.5).

This could be caused by a different melting rate between the deposited layers with a resulting build-up of material at the edges . On the other hand, the no-cap samples do not have accumulations on the sides but have very large ablated areas that could compromise the junction.

A complessive SEM analysis reveals the presence of ablated areas especially if the melting takes place in a nitrogen atmosphere. In particular, the ablated areas are very large and irregular in the absence of amorphous germanium caps and are very evident in the nitrogen atmosphere and a little less evident in the air. As for the sample with the amorphous germanium cap, the ablations are reduced to localized holes with a diameter of a few nanometers. Such holes occur in large numbers and are very spread uniformly over the entire surface in the presence of

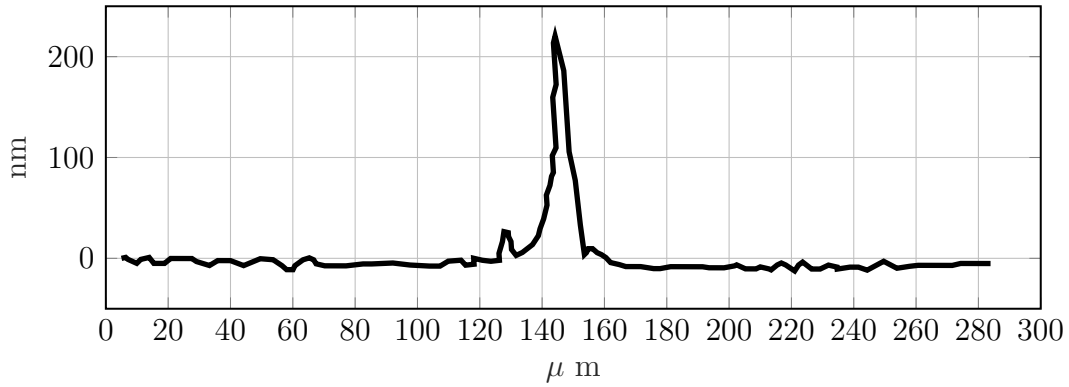

Figure 3.5: *Perimetral spot peak of agglomerated material on the side of the spot with a-Ge cap at the boundary between the doped and non-doped region after the PLM. Measure on profilometer*

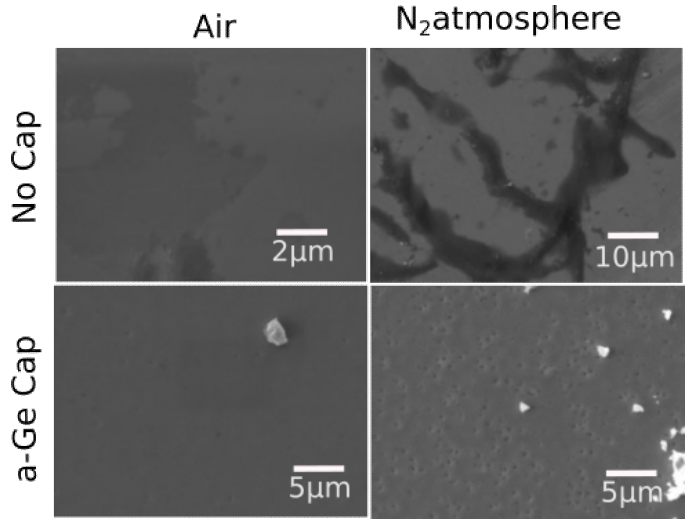

Figure 3.6: *Scanning electron microscope analysis of the doped samples with 500mJ/cm^2 pulsed laser treatment. Vertically a comparison between the samples with pre-deposition of aluminum (4 nm) and those with aluminum (2nm) coated with cap of amorphous germanium (40nm). In horizontal a comparison of the samples lasered in air and in nitrogen atmosphere.*

nitrogen atmosphere but are much less numerous in the presence of air.

A further analysis under the atomic force microscope (AFM) quantitatively confirms the observations on the SEM, showing that the thickness of the ablations is about 20-40 nm for both samples with and without amorphous germanium cap above the aluminum layer. Such ablations are confirmed in very large spots for no-cap samples and localized in holes of a few nanometers in diameter for samples

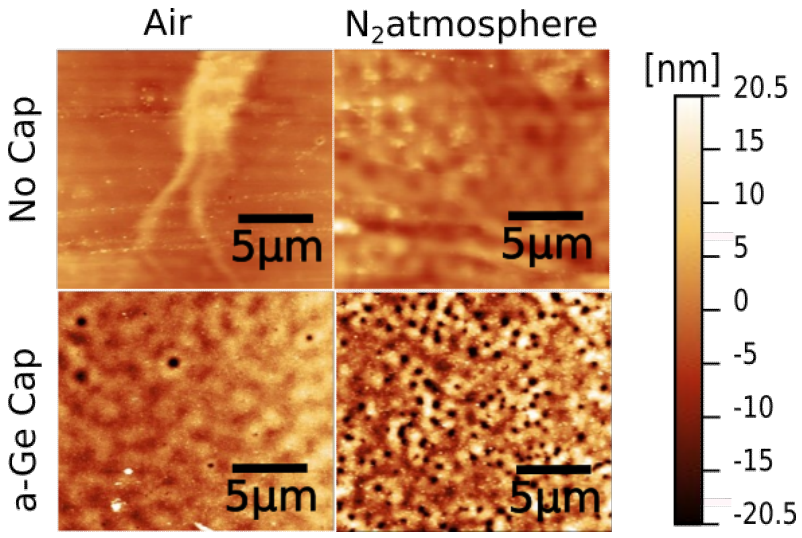

Figure 3.7: *An atomic force microscope scan confirms the SEM analysis of no-cap procedure and 40/2 procedure, showing that the ablations have a depth of tens of nanometers.*

	Air	N_2 atmosphere
No Cap	Diffuse ablations over large areas	Very evident ablations over large areas
a-Ge Cap 40/2 nm	Reduced ablated holes	Ablations localized in single holes

with a-Ge cap.

A direct confirmation of these ablations in the doping procedure 40/2, was measured with the reverse IV charateristics, that I will deal with in the paragraph 4.1.5; briefly anticipate only that the gold metallization of the rectifying contact in the presence of ablations, worsens the quality of the diode in reverse polarization.

Optimized 10/4 procedure

After several attempts at detector processing and having collected enough results for an idea about the efficiency of the doping procedure, we moved on to optimize this procedure by changing the thickness of the amorphous Ge cap and that of the underlying Al. This recent 10/4 doping procedure is shown in the figure 3.8

Samples lasered with the optimized 1/4 procedure have a homogeneous surface, with low probability of ablation and with limited oxygen contamination.
Figure 3.9 shows an SEM analysis, in which the good visual homogeneity of the processed surface is noted and the SIMS measurements confirm both the homogeneity in the composition, showing a fairly reproducible Al concentration profile in various regions of the sample, and the reduced oxygen contamination.

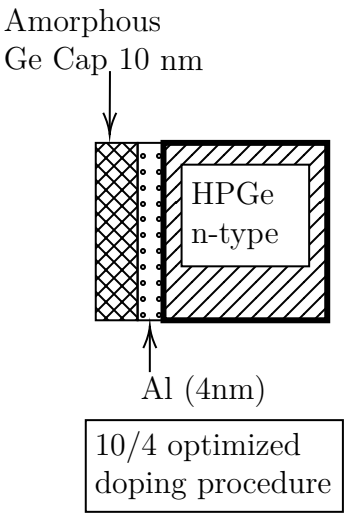

Figure 3.8: *Optimized 10/4 doping procedure:A 4 nm thick layer of Al is isolated from the atmosphere with a 10 nm Cap of amorphous Germanium*

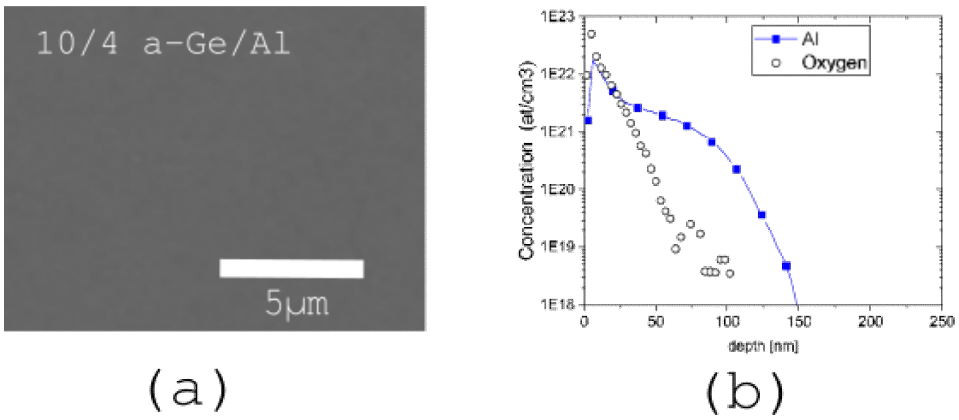

Figure 3.9: *Surface doped with 10/4 doping procedure: SEM analysis shows homogeneity and rare presence of ablations; SIMS measurements confirm spatial homogeneity with limited deep oxygen contamination*

3.2 Improvement of manifacturing processes

The optimization of some manufacturing processes for the improvement of the operation of the diode in reverse bias is a fundamental step as well as the main purpose of the research.

Beside the optimization of the junction on microelectronic grade germanium that was briefly summarized in the previous paragraph, we focused on some critical step of the starting manufacturing procedure of the detectors prototypes that was described in the previous chapter. This starting procedure brings to the production of diodes that, as we will see in the next chapter, suffer of breakdown at lower voltage with respect to what expected.

- The first idea concern a fundamental difference between the material we used for standard optimization of the junction that is commercial microelectronic grade germanium with a polished low roughness surface, and the the standard surface that we use for detector that is an etched surface. As we will see such surface is very different in term of roughness and flatness. This in principle may affect the laser doping in two ways: roughness may change the light reflectivity varying the amount of energy deposited by the laser so influencing the transferability of the optimized protocol from microelectronic to HPGe germanium. An other point is that roughness my be transfered to the junction depth so introducing unwanted corrugation effect of the junction depth. We formulated the hypothesis that the such roughness could influence the breackdown voltage since it is known that the breakdown voltage decreases as the radius of curvature of the junction decreases [SG66].

- An other critical point that we realized in the starting processing protocol is the to much aggressive effect of the $HF : HNO_3$(3:1) ething we adopted for segmentation. The advantage of this etching is that it is part , once concluded by a methanol soaking, of a well assessed passivation procedure [Mag+18]. It means that the same etching that produce the excavation between the contacts can be used to create an insulating surface free of charge between the contacts. Unfortunaltely we relized that this etching is too aggressive (about $17\mu m/min$) and cause an undercut above the gold mask that cover the contact as can be observed in Fig. 3.10

  The presence of large canopies that may break in some case, is a very dangerous effect since it may cause a metale tip effect between the polarized contact and the bulk possibly inducing breakdown effects.

  In paragraph 3.2.2 we therefore tried to investigate the effect of lower rate etching in order to have a better control of the undercut detrimental effect.Test of new wet etching solutions that guarantee greater etching control such as 3HP etching instead of $HF : HNO_3$ (1:3) [BV62] [Bar+19] .

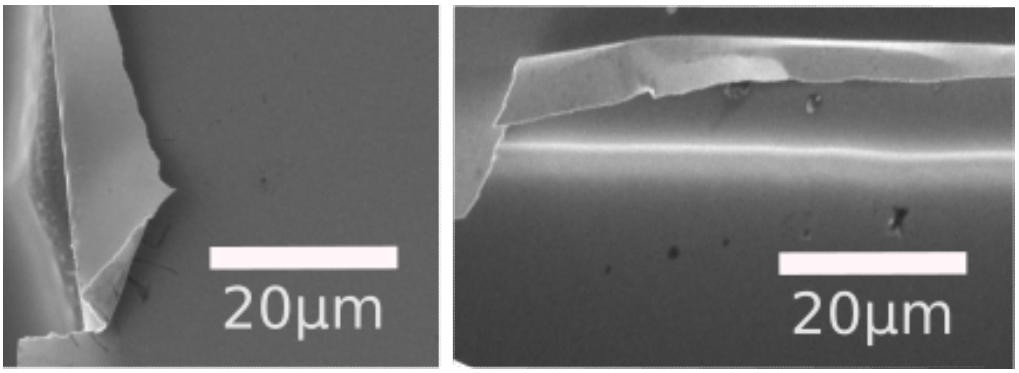

Figure 3.10: *Gold layer canopies on the gap-segment excavation interface after a $HF : HNO_3$ wet segmentation etching; such etching is very aggressive and also excavates below the gold layer near gap-segment interface.*

- Other aspect involves the control of contaminants. Contaminants of different nature that are deposited on the crystal during manufacturing can worsen the working characteristics of the diode in reverse polarizations. In particular, contaminants can influence breakdown, passivation and so the quality of the junction if present before the deposition of the doping atom layer on the substrate.The paragraph (3.3) will be dedicated to the optimization of contamination procedures.

3.2.1 Polishing

Chemical mechanical polishing (CMP) is a smoothing process to planarize the crystal substrate that combines a chemical etching action with a mechanical removal of the material. The procedure consists of a rotating pad on which the crystal is

pressed to smooth the surface. A slurry or etchant solution is interposed between the crystal and the rotating pad. Many studies regarding chemical-physical planarization have been done and there is a vast literature; for example Pitera et al [Pit+04] found low RRs using KOH and colloidal silica-based slurries in the CMP;

the development of Ge removal slurries in fact,was initially relied on silica particle slurries with alkaline compounds to improve removal.

Hydrick et al [Hyd+19] used colloidal silica particles (Nalco 2350) together with NaOCl, H_2O_2 and NH_4OH additives to improve the RR (Removal rate) of Ge, noting a high metallic contamination present in polishing with slurry containing NaOCl and absent on the samples polished with H_2O_2 slurry, but pitting corrosions were also observed for H_2O_2 concentrations greater than 5%. Very recently Peddeti and co workers [Ped+11] proposed an improvement of the above procedure using H2O2 at 1% and increasing the PH by adding KOH solution. The idea of the procedure is to promote surface oxydation of Germanium moving the oxidation process toward the formation of unstable and water soluble Germanium oxide compounds by PH regulation. Oxidation at room temperature is very superficial involving few nanometers at maximum , at the same time the pad and water action remove the oxide selectively on protruding part of the oxide crystal that can undergo further oxidation and removal. The final effect is a flattening of the surface very effective and very "soft" being not necessary the use of hard particles for physical removal that may induce lattice damaging.

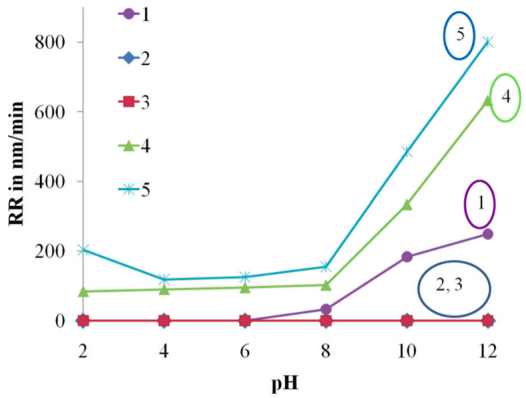

Figure 3.11: *Ge wafer coupon dissolution rate in (1) 1 wt % H_2O_2. Ge disk RRs obtained when polished with (2) pH adjusted DI water, (3) 3 wt % colloidal silica particles in DI water, (4) 1 wt % H2O2, and (5) 3 wt % colloidal silica particles þ 1 wt % H_2O_2. The rates for both (2) and (3) are almost "zero" over the entire pH range. Credits: Peddeti et al [Ped+11]*

The figure (3.11) contains five curves showing the Removal Rate as a function of pH for various polishing solutions. With reference to curve 4 (green) we have prepared a1 w/v % H_2O_2 solution by increasing the pH up to 11 through the following steps:

- **Preparation - 100ml of 5 M KOH solution** Since the molar mass of KOH is $56{,}10\frac{g}{mol}$ we proceeded to calculate the weight in grams to be diluted

in 100ml of DI water to obtain a 5 molar solution:

$$x_g(KOH) = 5\frac{mol}{l} * 0.1l * 56{,}10\frac{g}{mol} = 28.055g \tag{3.1}$$

this solution was used later for the pH correction of 1 w/v % H_2O_2 solution prepared later.

- **Preparation of H_2O_2 solution at 1 w/v % in DI water**

  Since the available H_2O_2 solution is 30 w/v %, and we want to obtain a 1 w/v% solution in DI water, we proceeded to calculate the volume of H_2O_2 in ml to be brought up to 1l with DI water:

$$30\% * x_{l(H_2O_2)} = 1\% * 1000ml \implies x_{l(H_2O_2)} = 33.333ml \tag{3.2}$$

- **pH correction of 1 w/v % H_2O_2 solution with KOH drops**

  Once the 1 w/v% H2O2 solution was obtained, the pH was measured by adding drops of 5M KOH solution each time. 317 drops were counted to reach a pH between 10 and 11 ,but we have to see how many liters correspond to 317 drops starting from the calculation of the liters corresponding to a drop. The weight of 10 drops was measured to be 0.332g and allows us to calculate the weight of one drop as $0.332g/10drops = 0.033$g; since 10ml of KOH solution weighs 10.38g, dividing by the weight of one drop, we get the number of drops in 10ml:

$$n_{\text{drop in 100ml}} = 10.38g/0.033g \sim 313drops \tag{3.3}$$

  and therefore the ml corresponding to a drop are:

$$l_{drop} = \frac{10ml}{313drops} = 0{,}032ml \tag{3.4}$$

  Therefore, to adjust the pH of 1l of 1w/v % H_2O_2 solution in DI water, 375 drops of 5M KOH solution are needed, which correspond to $375 * 0.032ml \sim 12ml$ of KOH solution to be added.

- **Polishing of the semiconductor substrate**

  Once the solution was prepared, the face(on which the pn junction has to be subsequently processed) was polished. The polishing procedure consists in a semi-manual procedure. An special pad with super-finishing cloth (Presi-SUPRA 0.03 μm) was fixed to a rotating plate and the crystal was manually moved on the plate while the plate is gradually wet with the solution.

  The speed of the rotating disk was set at 90 rpm and 100ml/minute of prepared solution were sprayed, to allow adequate exchange of the dirty water.

The removal rate (RR) was calculated by measuring the mass lost at set time intervals; in particular, the average depth of dissolved volume was obtained from the lost mass as:

$$d_{dissolved} = \frac{m_{lost}}{\rho_{Ge} * A} \tag{3.5}$$

$$\implies RR = \frac{d_{dissolved}}{\Delta t} \tag{3.6}$$

where m_{lost} is the difference between a weight measurement and the one prior to the lapping process, $\rho_{Ge} = 5.3 g/cm^3$ is the density of germanium and A is the surface area of particular detector under processing. The obtained RR $\simeq 0.5\ \mu m/min$ is compatible with the results reported in the literature (see Peddeti et al [Ped+11]); this means that the procedure is not strongly sensitive to possible variation in the process due to the maual procedure such as uncontrollable variations in pressure of the crystal against the plate, as the detector was kept with the hand.

Below are the tables of these values calculated step by step by time and the relative graph. The quantities shown in the table are cumulative and therefore a difference must be made between the successive quantities to obtain the dissolution rate and the speed. The RRs of lapping and CMP were also reported using a colloidal silica slurry; this slurry was prepared with the same recipe as before but using colloidal silica instead of DI water.

Head 23	t(min)	RR μm/min	Lost Mass tot (mg)	Rough (nm)
Lapping	15	1.90	145	
Lapping	45	0.87	279	
Lapping	90	1.01	510	2800
1% H_2O_2	107	0.46	550.3	21.5
1% H_2O_2	116	0.54	575	16
1% H_2O_2+silica	121.5	0.98	602.55	9
1% H_2O_2	128.5	0.42	617.7	14
1% H_2O_2	135.5	0.53	636.6	12
1% H_2O_2	142.5	0.44	652.3	6
1% H_2O_2	151.5	0.60	679.8	10
1% H_2O_2	158.5	0.58	700.7	11
1% H_2O_2	164.5	0.56	717.85	
	$< RR_{polish} >= 0.51$	$\sigma_{RR_{polish}} = 0.14$		

The different table refere to data obtained on different crystal realted to different detector prototypes (internally named HEAD23, HEAD9 adn PRONG1n). The

PRONG 1N	t(TOT)min	RR μm/min	Lost Mass tot (mg)
Lapping	60	2.23	864.2
1% H_2O_2	91	0.48	962.1
1% H_2O_2	106	0.48	1009.2
1% H_2O_2	12	0.48	1055.6
1% H_2O_2	136	0.46	1100.8
1% H_2O_2	151	0.56	1155.8
1% H_2O_2	166	0.57	1211.1
	$< RR_{polish} >= 0.51$	$\sigma_{RR_{polish}} = 0.16$	

PRONG 3P	t(TOT)min	RR $\mu m/min$	Lost Mass tot (mg)
Lapping	70	1.49	680.17
1% H_2O_2	103.5	0.57	805.39
1% H_2O_2	130	0.59	906.8
1% H_2O_2	153	0.62	999.92
1% H_2O_2	176	0.46	1068.22
1% H_2O_2	186	0.48	1099.76
1% H_2O_2	196	0.50	1132.2
Lapping	203	2.44	1243.2
1% H_2O_2	214	0.55	1282.85
1% H_2O_2	240.5	0.54	1375.09
	$< RR_{polish} >= 0.53$	$\sigma_{RR_{polish}} = 0.13$	

typical lateral dimension of the sample was 2 cm. We also made and evaluation of the roughness by means of an about 2cm long scan with a stylus profilometer. We can also evaluate the peak to peak flatness along the scan that is quite small in all the cases and lower than few micrometers. The procedure is very effective and reproducible with an avarage removal rate of $0.5 \pm 0.1 \mu/min$. This procedure is not order of magnitues slower that lapping procedure just a factor 3 to 4. Moreover the introduction of silica slurry about double the rate but ad a physical process which residual damage should be tested. After 60 minutes lapping we removed typically 30 microns obtaining a low roughness mirror like surface. This erosion corresponds to 10 times the grain size of the lapping material thus probably guaranteeing a good lattice quality. Work is in progress in order to specifically confirm this point by means of X-ray diffraction crystal damage evaluation.

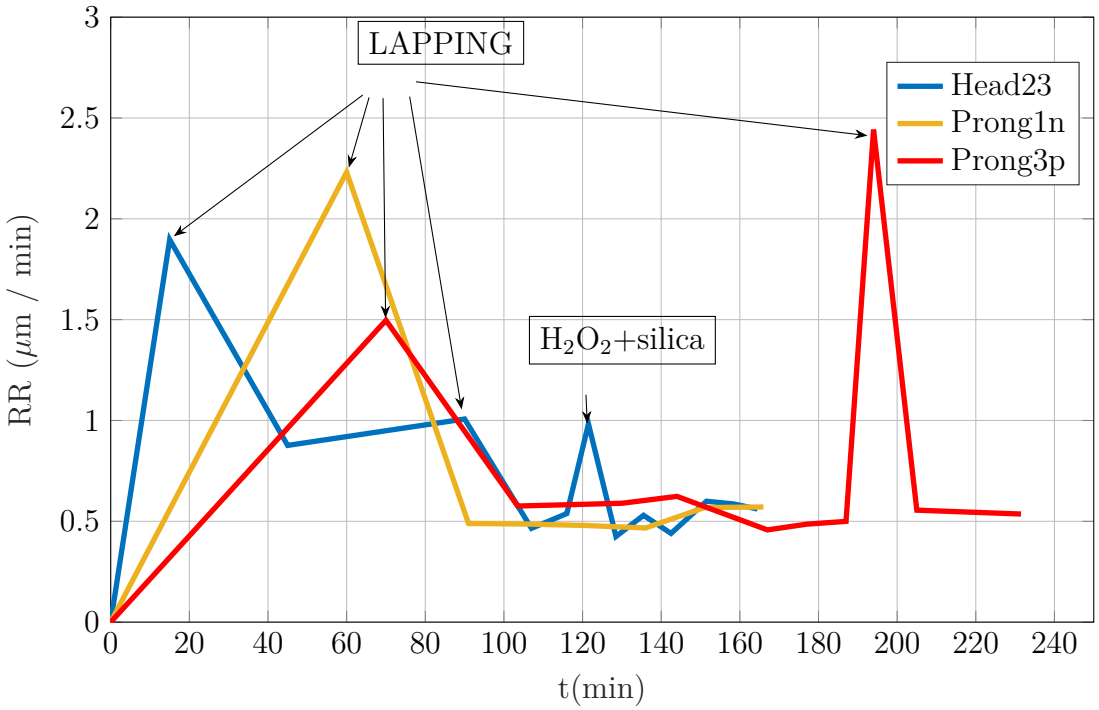

Figure 3.12: *Removal Rate calculated by measuring the mass lost over various time steps for the Head 23, Prong 1n, Prong 3p crystals*

3.2.2 3HP etching test

Common solutions for crystalline Ge etching are hydrofluoric acid and nitric acid mixture diluted in DI water or peroxide-acid-based mixtures. In particular, solutions with peroxide are widely reported in the literature for the selective etching of crystalline SiGe in the manifacturing of nanowire-based gate-all-around transistors in the next-generation logic and memory devices; the selectivity of etching derives from the faster oxidation of Germanium compared to Silicon in the presence of strong oxidants such as HNO_3 and H_2O_2 [Bar+19].The standandard procedure adopered up to now make use of a HF and HNO3 solution with ratio 1:3. Preliminary results obtained by our group [Col] demonstrated that use of a solution of HF and H_2O_2 in 1:1 proportion, diluted in water has a slower and more controlled etch rate that guarantee a good flatness on undoped microelectornic germanium. This last etching will be in the following named 3HP.

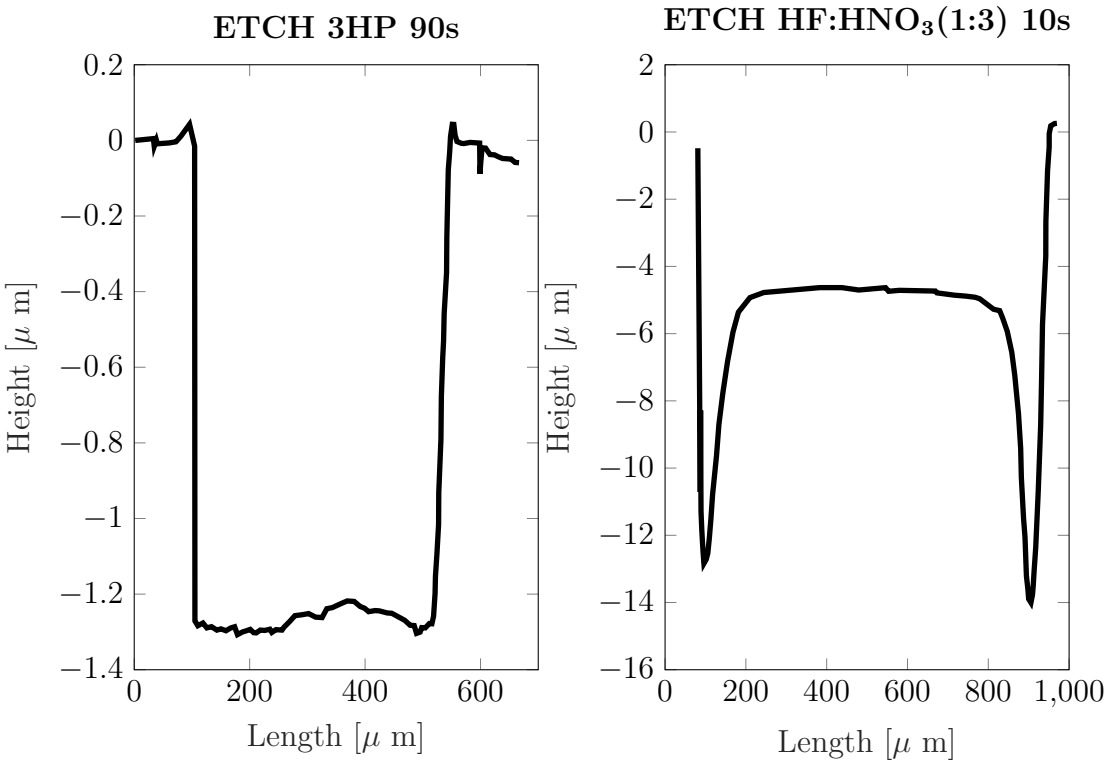

Figure 3.13: *Profiles measured after etching tests with 3HP solution (right) and HF: HNO3 (1: 3) (left). HF: HNO_3 etching shows an uncontrolled removal effect near the edges*

The difference on the effects of etching 3HP and HF: HNO_3 (3:1) have been tested by us on hyperpure germanium to obtain and evaluate the edge effects; 3HP etching is a solution of H_2O_2 (3%): HF (3%): H2O (94%). The profiles after the

etching tests on a resistive-Ge wafer are shown in the figure 3.13; in the figure a stilo profilometer heigt scan is performed trough an etched segmentation trench; the left and right part at about zero level are two Ge area covered by gold that prevent the etching, while the valley in the middle show the effect of the etch that will have the aim of removing the junction and create an insulation gap between the contacts during as a step of the detector production.

These plots show the differences between the gap profiles on the hyperpure germanium substrate, segmented with 3HP etching (left) versus HF:HNO_3 (3:1) etching (right). As can be noted the $HF : HNO_3$ (1:3) etching is very fast and notwistanding the short etching time (10 sec) at limit of what can be controlled in a manual chemical procedure, it produces a very deep trench even too much with respect to our aims that are to remove a 200nm deep junction. Edge effects are noted on the the gap etched with HF: HNO_3i.e. deeper valleys are produced colse to the mask; the etching edge effect is more controlled using the 3HP solution.

Being both etching hysotropic, we can deduce that the under cut effect below the gold will be of the order of the etching depth so much more reduced for HP etching.

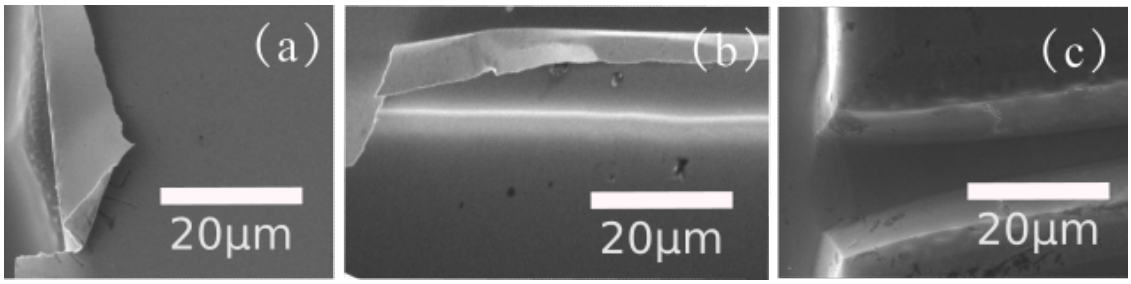

Figure 3.14: *SEM images of segment-gap interfaces after segmentation HF: HNO3 etching. The segment is covered with a layer of gold to prevent etching, but in this excavation interface, the gold layer breaks off into "canopies"(a); this etching in fact is very aggressive and removes material even below the gold layer (b), leaving it uncovered for a few thicknesses of the order of a few micrometers.The segment-gap interfaces after gold removal are also shown (c).*

After this preliminar test, we fabricated a detector with the HPGe etching obtaining an unexpected unsatisfactory results. In Fig 3.15 the surface of detector etched after lithography is shown. As can be noted a checkered structure is visible in the zone not masked by gold deposition.

This structure re-sample the structure of the laser spot array and suggest that etching may be different on lasered germanium. It is worth to note that the in the first trial the doping process was not performed but just the gold deposition and the lithography. In order to deeper understand this phenomenon we proceeded with a controlled test performed over a portion of Ge doped by the Ge/Al deposition

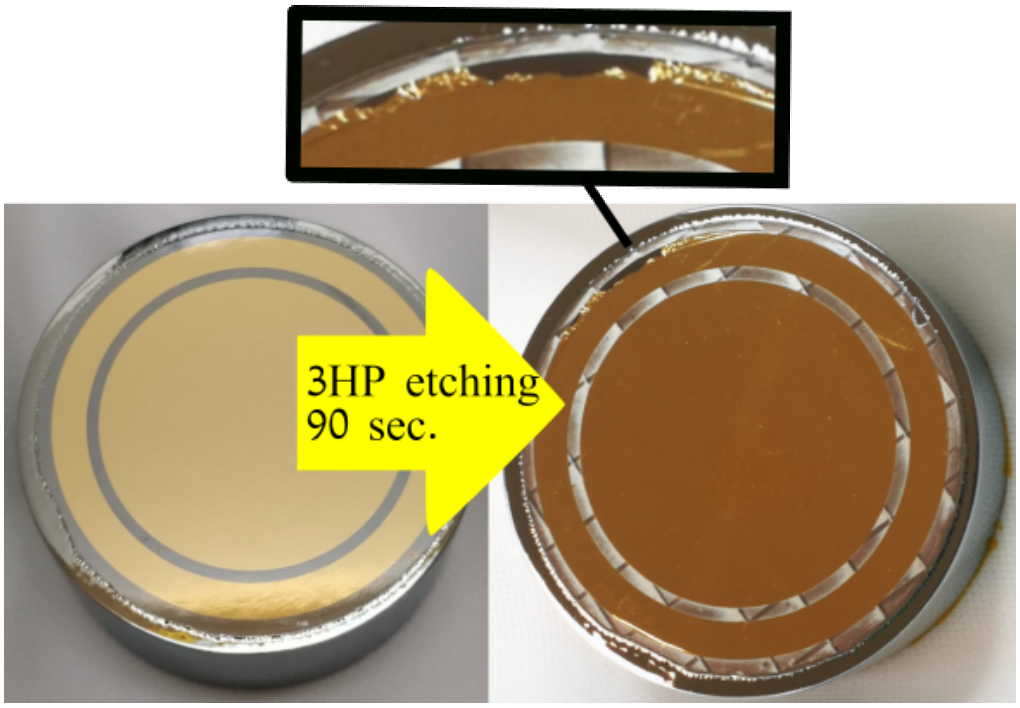

Figure 3.15: *3HP etching effect for the segmentation of a p + junction of a Head detector; in the gap between guard ring and central pin, the checkered texture becomes very evident and in relief. The gold layer at the edges of the contacts is partially damaged.*

and lasing.

We tried to study the selective etching effect on the interface between a doped and non-doped resistive germanium region. After having processed with a single spot a piece of germanium, we covered part of the doped region with a kapton tape that act as an etching mask. A first etching were performed with 3HP for 1 minute. Profilometer scans were performed between masked region and unmasked-undoped region (1a), between unmasked doped and undoped region (2a) and between masked and doped region (3). The scans are qualitatively described in the experimental scheme in figure 3.16 . In a second etching step we removed the kapton mask and performed one more minute of etching and then we repeated the previus scans.

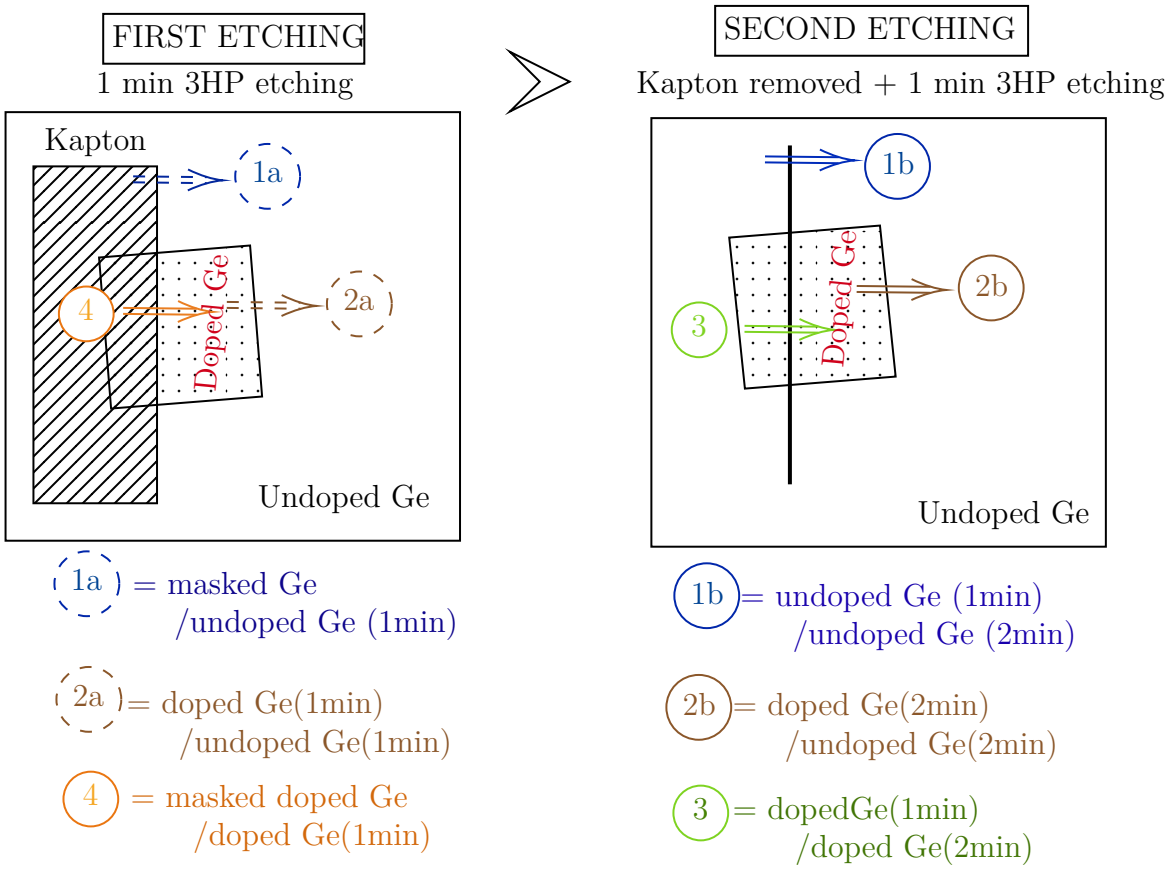

Figure 3.16: *Experimental procedure for the evaluation of selective etching on various resistive Ge interfaces and doped spots using the 3HP solution; arrows indicate scan paths with a profilometer after the two etching cycles. The profiles relating to the arrows are shown in the figure 3.17and 3.18*

Figure 3.18 shows the effects of 3HP etching on undoped Ge/undoped Ge interface (blue curves), unmasked doped Ge / unmasked Ge interface(brown curves) and doped-spot/doped-spot interface (green curve) at the first 1 minute etching step (dotted lines) and at the second 1 minute step (solid lines) on the same sample, in

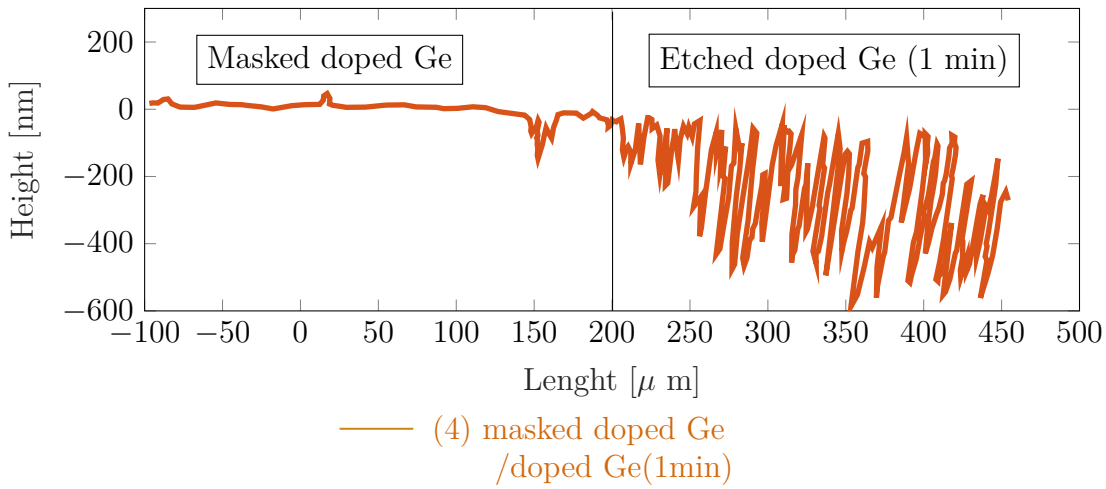

Figure 3.17: *Profile measured on the interface masked doped-Ge/unmasked doped Ge with 3HP solution for 1 min, related to the experimental scheme in figure 3.16. The not-etched spot surface was covered with Kapton*

which one of the two interfaces has been covered by kapton to measure the height difference.

The experimental procedure is also illustrated in the figure 3.16, where the arrows indicate the scan path with a profilometer; The dotted arrows are relative to the first etching step, the continuous ones are relative to the second etching step. The profiles shown in the figure 3.18 (related to the arrows in the figure3.16) have been translated in height by taking the original masked germanium region has the zero level and the removed germanium level after one minute etching compared to the zero level, as an intermediate level; the relative measured height of etching of the etched-spot (1min) / etched-spot (2min) interface (green) it is compatible with the translation of the brown curves (etched-spot / Ge) made previously by taking as references the levels of germanium removed and comparing them to those of the blue curves (Ge / Ge).

For the resistive Ge an RR $\sim 1.1 \mu m/min$ was measured, while the etching effect on the doped spot is stranger, which shows an etch-stop with an increase in roughness at the first minute of etching and then a RR equal to $\sim 1.7 \mu m/min$ at the second minute of etching.

This peculiar behavior would deserve for further investigation to be fully understood. But definitively demonstrates that 3HP etching is not suitable for trenching of p+ laser annealed junctions. In general etching rate variation as a function of the dopant is reported in litterature and is due to the fact that dopant may change electron or hole availability that modifying the kinetic of chemical reaction at the surface. On the other hand , preliminarily tests of our group on Molecola Beam

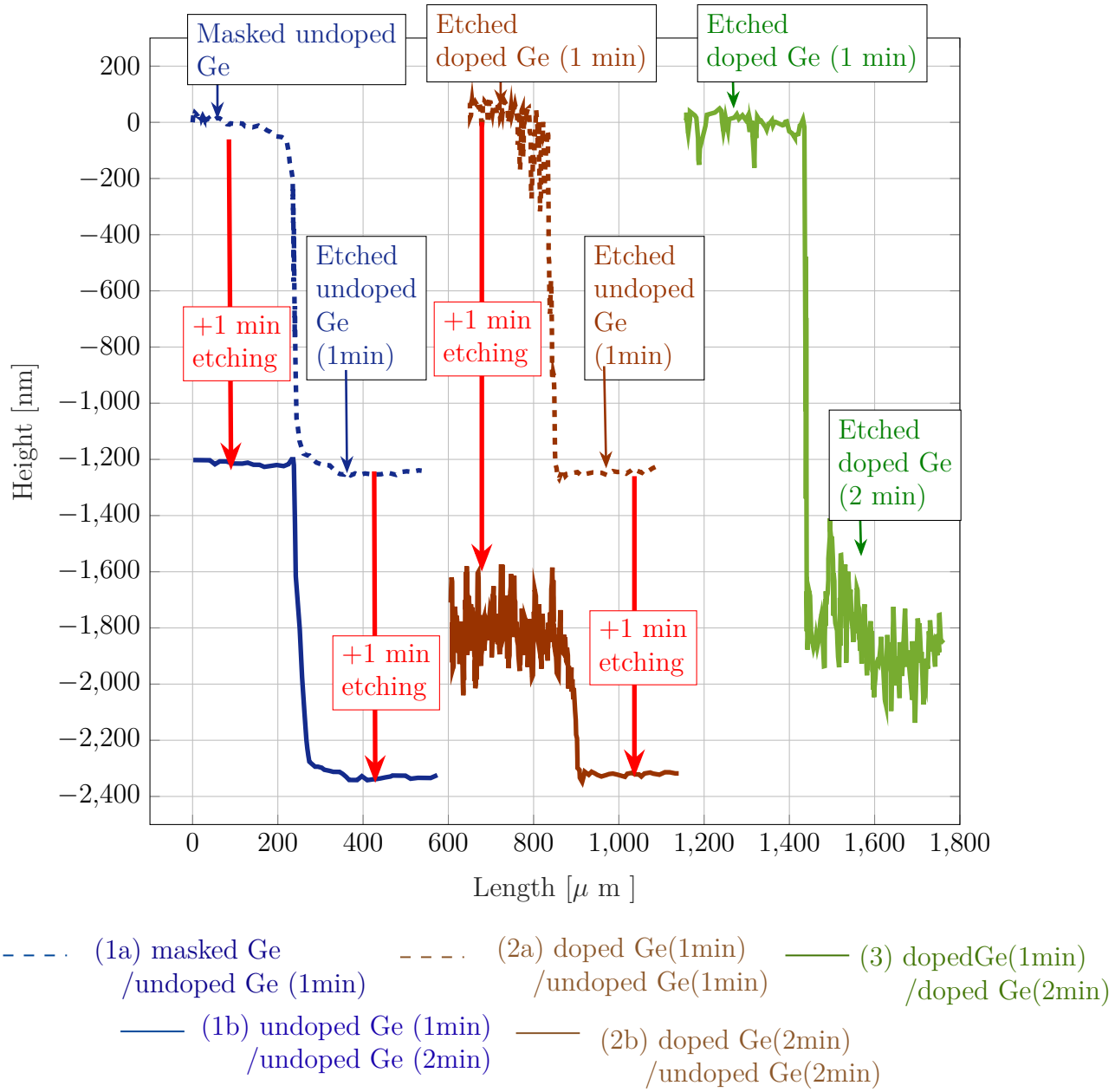

Figure 3.18: *Etching profiles measured on various interfaces related to the experimental scheme in figure 3.16 in which the various scanning interfaces (labeled as 1a, 1b ...) are listed in the legend; in the interfaces of the same type, one of the two was covered by Kapton during the first etching step, to measure the relative excavation height.*

epitaxy doped layer showed very limited effects of 3HP etch rate modification [Col] (actually for this reason we selected 3HP as a good candidate for trenching) .Therefore we can not exclude a chemical role of Al and or Oxygen that are confined at the surface of the Ge/Al laser junction. In the future, in order to improve the undercut problem, other approach like reactive ion etching are being investigated. It is worth to note that the changing of trenching procedure has to be accompanied with a modification of passivation procedure and therefore still further optimization work should be performed on this point.

3.3 Kapton adhesive contamination

[Lai+09]

3.3.1 Introduction

The Kapton tape is composed of a very thermally and mechanically stable polyimide film [-200 ° C- 400 ° C], coated with a silicone adhesive resistant to chemical attacks and therefore widely used for the protection of the desired regions of the germanium crystal during the processing. Among other properties, it is transparent to x-rays and resistant to radiation damage.

Furthermore, thanks to its intrinsically low modulus of elasticity, kapton is very suitable for processes at high temperatures because it relieves stress between substrates with different thermal expansion.

On the other hand, the siliconic adhesive is one of the main contaminating materials for our purposes, since at high temperatures the silicone adhesive part softens, adheres to the germanium substrate and remains attached to it after the removal of the kapton at the end of the crystal processing. Tests were then carried out for the best solution for cleaning the kapton adhesive which, as we will see, has influenced the detector response very positively by moving the breakdown voltage two decades ahead of the previous electrical measurements and therefore brought to change the chemical cleaning process.

I will therefore focus on:

- Understanding how kapton adhesive is chemically made
- Description of the tests I have done regarding the cleaning of kapton or on how different chemicals affect the silicone glue
- Present the finally best result.

3.3.2 Chemical composition of the adhesive

The tape Kapton adhesive is made of MQ siloxane resin and crosslinked polydimethylsiloxane (PDMS) or phenyl siloxane.The adhesive is therefore mainly composed of the silicone polymer, characterized by the siloxane bond (O-Si-O) with organic side chains R linked to the Silicon to form the polyorganosiloxanes (-R2SiO-) n.

The R group can also be an alkane (i.e. a molecule of only carbon and hydrogen) but in the case of silicone glue R is an alkyl group, i.e. an alkane group deprived of a hydrogen atom. The most common organic group R in silicone glues is the methyl group (CH_3) representative for example of the polydimethylsiloxane $[SiO(CH_3)_2]_n$ polymer. However, the composition of the glue has been tested with an EDS spectroscopy analysis as, usually, other organic groups are reacted with the silicon atom

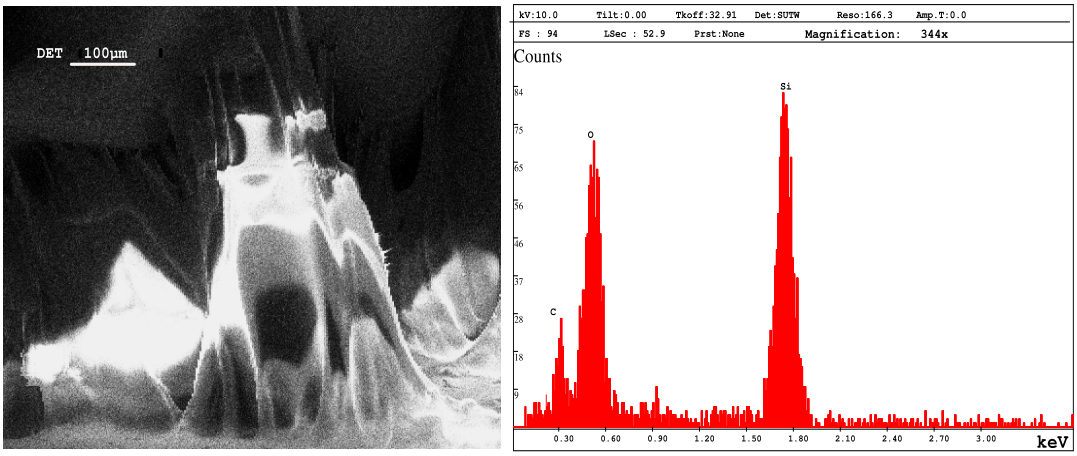

Figure 3.19: SEM scanning of the silicone kapton tape adhesive and EDS spectroscopy

to give the polymer greater thermal stability, greater resistance to solvents or other physical and chemical properties.

The resin is the second component of the glue since, being the silicone polymers very weak when cross-linked in a polymerized matrix, they are reinforced with fumed silica or precisely silicone resins. The two main methods used for silicone glue removal are:

- the use of solvents
- the use of silicone digesters or emulsifiers

3.3.3 Experimental test of solvents

The "primary" solvents used for siloxane decontamination test are: 1 methyl-2 pyrrolidone(NMP), xylene, toluene, accompanied by a "secondary" solvent, in this case IPA which allows to remove the primary solvent, to give a further cleaning and to empirically test whether a reaction with the primary solvent occurs such as to degrade the silicone adhesive. The use of solvents must be accompanied by a mechanical removal action through the use of a swab, since the solvent alone softens and swells the glue and therefore needs a mechanical action removal.

- First we proceeded to dirty some pieces of germanium wafer by sticking the Kapton tape and putting the covered face in contact with a hot plate at T = 100 ° C for 5 minutes. When detaching the tape from the sample, the glue softened by the heat remains partly stuck to the substrate, as can also be seen by eye.

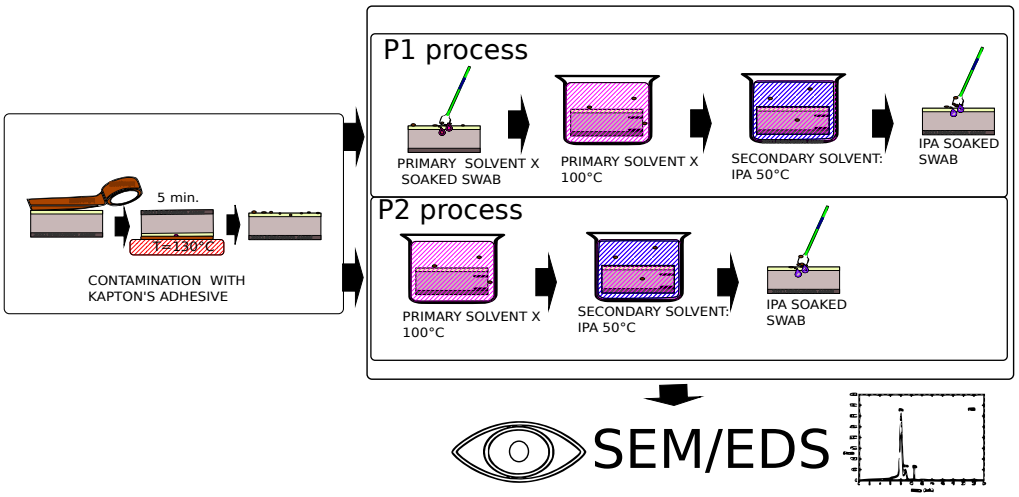

Figure 3.20

- For each solvent two procedures were used which we will call P1 and P2.

  1. P1 consists in scrubbing the contaminated surface with a swab soaked in solvent at T = 100 ° C, immersion of the sample first in the solvent for 5 minutes at 100 ° C, immersion IPA (Isopropyl alcohol) at 50 ° C for 5 minutes, rubbing with a swab soaked in IPA at T = 50 ° C.
  2. P2 consists in immersion of the sample in the solvent for 5 minutes at 50 ° C, IPA immersion at 100 ° C for 5 minutes, rubbing with a swab soaked with IPA at T = 50 ° C.

- After that, the effect of these treatments was verified with a Scanning Electron Microscope, since the glue is not conductive, it is not transparent to the electron beam.

Preliminary results

The images in the Figure show the various contaminated samples in question before treatment, after treatment and, in the case of P2 xylene, also after SEM scanning.

- In the case of NMP it can be seen, both in P1 and P2, that the silicone adhesive has been dissolved but the action of the sweb has spread it on the surface (figure 3.22(a),(b)), increasing the contamination, even if to the eye the surface seemed shiny and clean (figure 3.21). This solvent, used up to this point, is therefore to be avoided.

- Toluene, on the other hand, has a more effective effect than NMP (figure 3.21). The surface seems very clean after the P1 and P2 treatment, but a

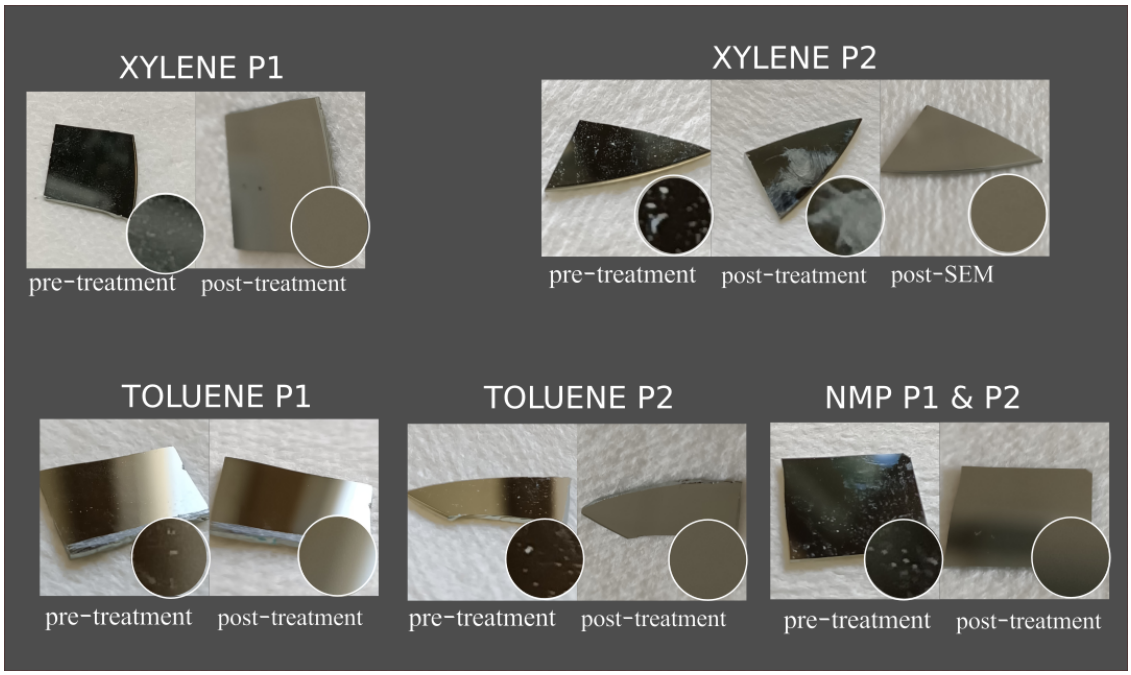

Figure 3.21: At first glance, all appear to be very clean except for xylene P2 which shows a layer of white debris that evaporates during SEM scanning

careful SEM-EDS research shows in various points some very thin layers of Carbon spread on the surface (figure 3.23(a)).

- Xylene, on the other hand, shows an excellent result with the P1 treatment, the surface is very clean and there is no trace of glue except for some pieces not adhered to the side corners of the sample, where the sweb has not been rubbed. It also shows a very particular result in P2. The rubbing with the sweb soaked in hot IPA only at the end of the P2 process results in the formation of a white powder, product of the decomposition reaction of the adhesive glue.This powder was also not seen during the SEM scans because it evaporated at inside the vacuum chamber of the SEM as shown in figure 3.21. The formation of this reaction product by interaction of IPA and xylene through a swab is very important because it allows you to immediately see if a surface is contaminated with siloxanes or not, without the need for SEM scans and to clean it immediately, as this product is very volatile and non-sticky.

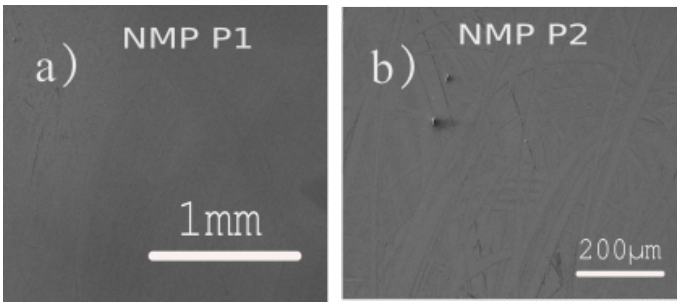

Figure 3.22: *Sem images showing the effect of NMP P1 and P2 processes*

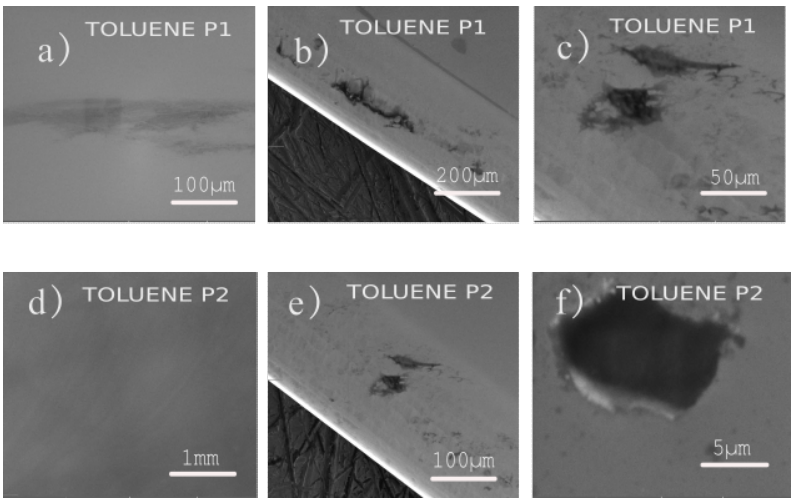

Figure 3.23: *Sem images showing the effect of Toluene P1 and P2 processes*

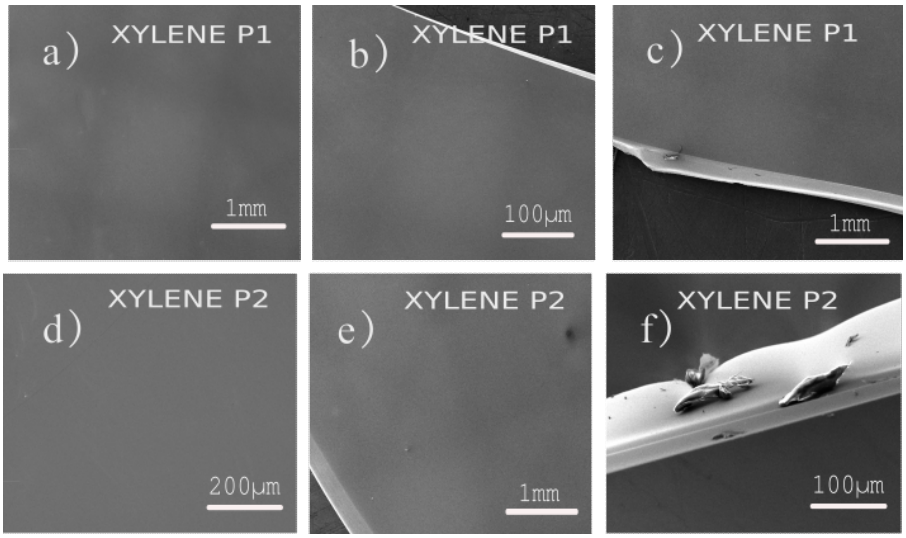

Figure 3.24: *Sem images showing the effect of Xylene P1 and P2 processes*

3.3.4 Reproducibility of the decontamination process, best results and conclusions

The test described above does not conclude the surface cleaning treatment because this procedure must respect some parameters to be faithful and reproducible, the optimal temperature limits; In some cases, in fact, the samples show the presence of carbon halos (similar to the effect seen on toluene with a SEM analysis) at high temperatures of the secondary solvents, while the complete removal of the adhesive does not occur at low temperatures, even when using xylene.

The procedure, as we have seen, works well for smooth surfaces but struggles to completely remove the silicone adhesive residues on the corners of the sample and inside the inlets; this is because the mechanical action of the pad is fundamental in the removal process, it is good for surfaces without morphological defects, but has a minor effect near the corners of the surface imperfections. It has been seen at SEM, through various empirical tests, that the addition of acetone in an intermediate state facilitates decontamination on the edges of the crystal

For these reasons, after a series of numerous empirical tests, by varying and combining the various parameters involved (temperature, combination of xylene and other solvents), a level of reliability and reproducibility of the siloxane decontamination process was achieved; The optimal procedure consists of the following points:

1. **Prepare the xylene solution to temperatures between 90 ° C and 110 ° C, a beaker of acetone to temperatures between 40-50 ° and a beaker of IPA to about 70 °.** Maintain these temperature limits throughout the duration of the whole procedure; decontamination does not take place at low temperatures, while at temperatures higher than those indicated, traces of carbon spread on the surface resulting from the combination of the various solvents at the end of the whole process (the reason not yet explained).

2. **rub more swabs soaked in hot xylene on the crystal surfaces** trying not to reuse the dirty parts for cleaning new surface regions. Insist on decontaminating the edges and imperfections of the crystal

3. **Immerse the crystal in the hot xylene solution for 10-15 minutes.** The silicone glue not removed from the swab will absorb the xylene and soften.

4. **Remove the crystal from the xylene beaker leaving the surfaces abundantly wet and rub it with a swab soaked in hot acetone;** this is the most important decontamination phase as as shown in the figure, in the case of cleaning with xylene in the P2 process, the coexistence of xylene (apolar) and acetone or IPA (polar) combined with the mechanical action of the swab, leads to the formation of a white powder of disintegrated siloxane if

parts of the crystal are still contaminated; such dust as shown evaporates by placing the crystal in a vacuum or or can be removed with swab.

5. **Immerse the crystal for 5 minutes in hot acetone, and repeat the mechanical cleaning with a swab soaked in acetone.**

6. **Repeat the whole procedure using IPA instead of acetone**

The xylene decontamination procedure was first applied to the Head9 crystal previously treated with NMP. Anticipating the analysis of the next chapter (4.1.3), the detector had given poor results during IV measurements as seen in curve 1 of figure 3.25. After treatment with Xylene for repassivation, the breakdown voltage has shifted by one orders of magnitude, confirming the analysis previously performed and confirming xylene as the best solvent among those tested.

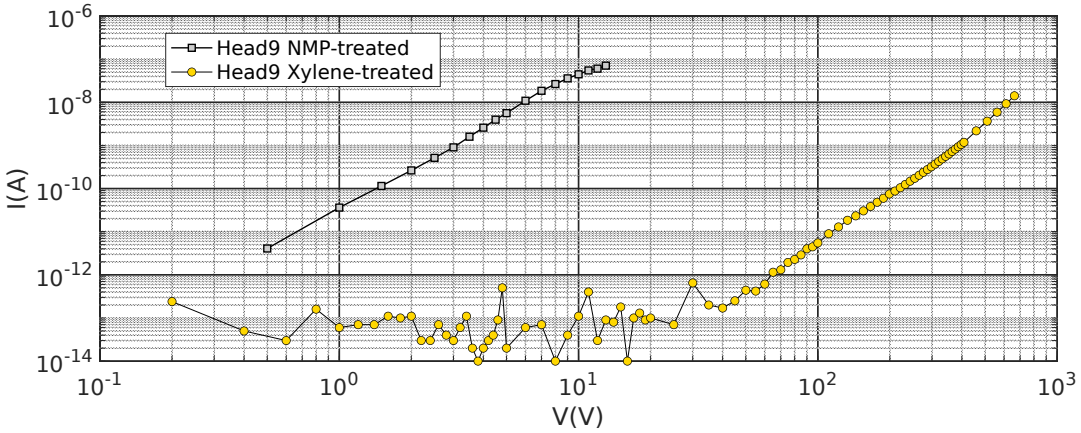

Figure 3.25: Comparison of IV curves in reverse polarization of Head9 treated with NMP and Xylene before the final passivation step. Note: the reverse bias voltages and currents are in absolute value for the log-log scale representation

Chapter 4

Detectors with p + junction

This chapter is dedicated to the measurements of the reverse IV characteristics and therefore to the characterization of the detectors. For segmented detectors, known methods are adopted for the measurement of the insulation between the contacts below the breakdown regime; a new method was tested to find the resistance even if one of the two contacts is in breakdown; The temperature dependence of IVs from important information on dominant processes for the leakage current. Activation energies derived from Arrhenius plots will be discussed.

4.1 Cylindrical diodes IV measurements

4.1.1 Description

Head 23 and Head 9 the are cylindrical HPGe crystal on which the most tests have been performed, regarding the optimization and processing of the p+ junction. These n-type detector have a diameter < 4 cm and a height of 2 cm; it consists of a p + Germanium-Aluminum junction processed with the PLM technique and implemented with or without lithography to study the effects of IV curves in reverse polarization in the presence or absence of guardring.

In order to fully deplete 2 cm, high DC voltage of reverse polarization (-2300V) is needed, as can be calculated by eq. 1.1 in chapter 1.

These high voltages put a strain on lateral passivation and the quality of the junction because the maximum field at the junction is as high as 2.3KV/cm according to abrupt junction approximation (eq. 1.23 chapter 1) . Imperfection at the jucntion depth, or at the border of the junction or in the passivation at the border of the junction my induce breakdown and the occurrence of leakage current that is detrimental for the detector permanences. IV characteristic curve is therefore the primary diode characterization useful to optimize the diode realization process.

However, the study of the curves corresponding to the different processing of the Head 23, has allowed the improvement of doping processes in surface preparation

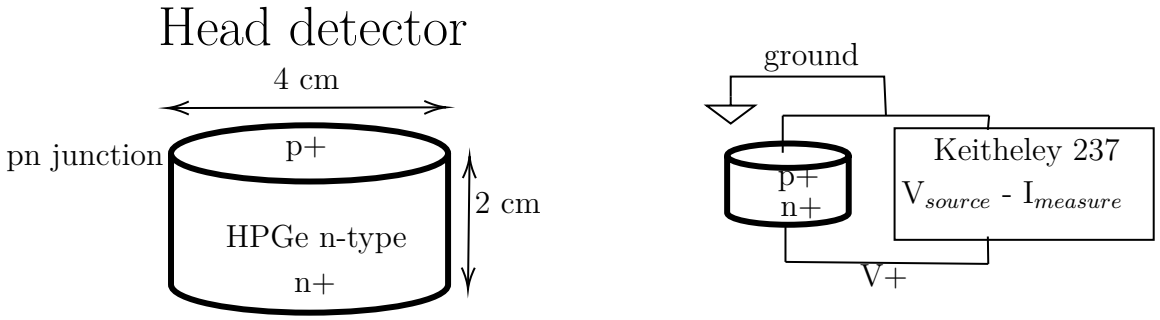

Figure 4.1: on the right, a schematic of the Head detector; on the left, the configuration for the reverse IV measures

by comparing the reverse IV curves obtained after progressing modifications to these processes. The reverse voltage currents (I-V) characteristics are related to the various reprocessing of the crystal . Most of the time we started by performing all the production progress of the p+ junction from the beginning i.e. by removing the previous junction and going on with the renewed junction production. The bare junction can be already tested after a chemical passivation process of the lateral surfaces and doing the electrical contact with the junction by means of indium plates. In some time, only the passivation process is repeated after annealing of the crystal and the cryostat to improve the vacuum or after a cleaning procedure of the lateral surface to improve contamination removal. The final goal of the procedure is to perform a test segmentation of the p+ contact by performing metal sputtered gold, and lithography of the guard ring (see paragraph 2.5) this was performed and tested two times with different processes of the junction. A consistent number of I-V measurements and process modification or repetition was performed; in the following a reasoned summury of the results is reported. from now on I will refer to **reverse bias currents** and **reverse bias voltage** taking them **with the positive sign**, as it is convenient for me for a log-log scale representation.

4.1.2 First tests on Head 23

Pre-lithography reverse bias IV measurements

The initial processing of the head 23 was done, as already mentioned, without the implementation of the guard ring and therefore without the use of lithography. The curves related to these processings are plotted in the figure 4.2 and show reverse bias currents (in absolute value) less than 1 nA at 100 V.

It can be seen in loglog scale that there is a significant change in slope at a reverse bias voltage value between 10V and 100V, which should correspond to the breakdown voltage. The depleted thickness corresponding to this voltage is about 2 mm against the 2cm that should be depleted.

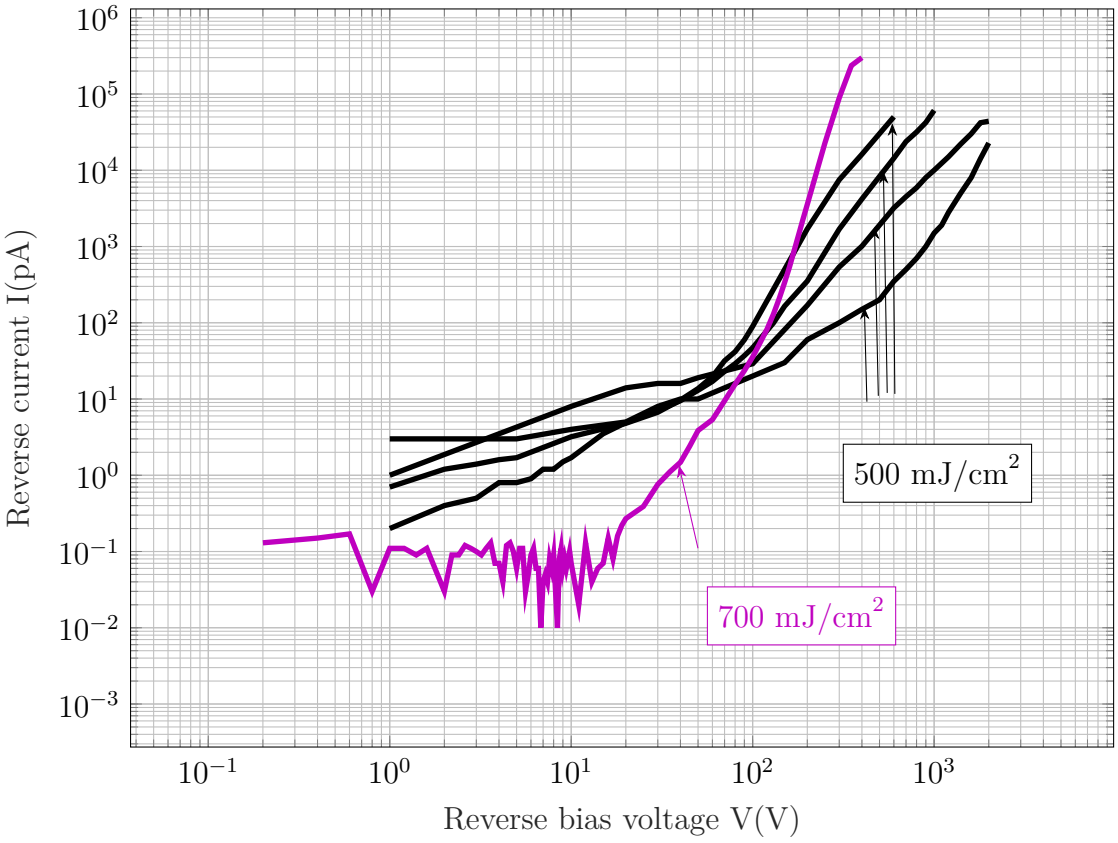

Figure 4.2: *First tests on Head 23 crystal with not-lithographed junction with 40/2 doping procedure; the various attempts to reprocess the p + junction with the PLM technique at pulse energy density* $0.5 Jcm^{-2}$ *(black curves) and* $0.7 Jcm^{-2}$ *(purple curve) are shown.*

The different curves are obtained after repassivation of the diodes or re-fabrication of the jucntion. No big change are obtained. In case when the laser energy is increased a more sharp breakdown curve is obtained with a lower leakage voltage bellow 15 V and a steeper power low breakdown above.
After the tests described, we decided to perform a lithography process with the aim of distinguish between the surface and the bulk leakage contributions by means of guard ring implementation. The results of such procedure will be discussed in paragraph 4.1.5. Before that here we show the effect of xylene cleaning procedure described in paragraph (4.1.3).
In the following a reasoned summary of the results is reported:

1. In Fig 4.3 (a):

   - the preliminary test curves described in the Fig4.2 are reported as black lines (first family) that are characterized by reverse bias currents less than 100 pA at 100 V . At this stage, a non-optimized deposit of a-Ge/Al 40/2 nm was used to fabricate the junction with pulse laser melting, with an energy density of 500mJ / cm ^{2}
   - brown dashed lines (second family), shows a worse trend of the curves (currents greater than 10 nA at 100V) after lithography has been done;these brown curves relate to the 40/2 doping procedure except one, which is highlighted in graph (c).Curves remained worse even after reprocessing a single junction contact without lithography i.e even if metal contant are removed and junction rebuild bu stretch. Junctions are produced more than one time, even annealing procedures of the crystal or repetition of the passivation are performed without any improvement of the leakage current . Most interestingly the curves remain with currents order of magnitude worse than before lithography test even if the pn junction with the optimized 10/ 4 nm a-Ge/Al doping procedure is performed.

2. Figure 4.3 (b) shows an improvement in reverse IV characteristics when a new xylene-based method of cleaning was implemented. More in details, the brown curve in 4.3 represents the 10/4 doping procedure IV measurements and shows a leakage current higher than 100nA at 100V that fell between the worst curves (the brown dotted curves). Exactly the same junction is tested again after applying the new cleaning method with xylene and re-passivating the diode (blue line), an improvement was measured, returning to the best curves of the first family. This is a quite good results that demonstrate how the contamination induced by kapton tape may induce breakdown at very low voltage and has to be strictly controlled in the production process. The idea is that the leakage current at very low voltage of the "brown" family of test is related to later breakdown of the diode i.e. is due to current going trough the lateral surface as it is very difficult to think that surface contamination may induce a bulk current. The lithography process involves the use of Kapton tape in various step to protect the face opposite to the junction to be lithographed. Kapton is used during baking and this may involve an heavy contamination. It could be quite surprising that the contamination still remain after many reprocessing of the of the crystal. The probable reason is that the reprocessing of the lateral surface consists in acid etching or cleaning procedures and the kapton tape glue accidentally reaching the lateral surface is acid resistant and may prevent a good passivation.

3. Figure 4.3 (c) shows that after cleaning the xylene, the reprocessing of the optimized 10/4 nm Al/Ge polished junction exhibits a slight worsening of the

IV's(green curve). A marked improvement occurs after an annealing of the diode as shown by the violet curve.

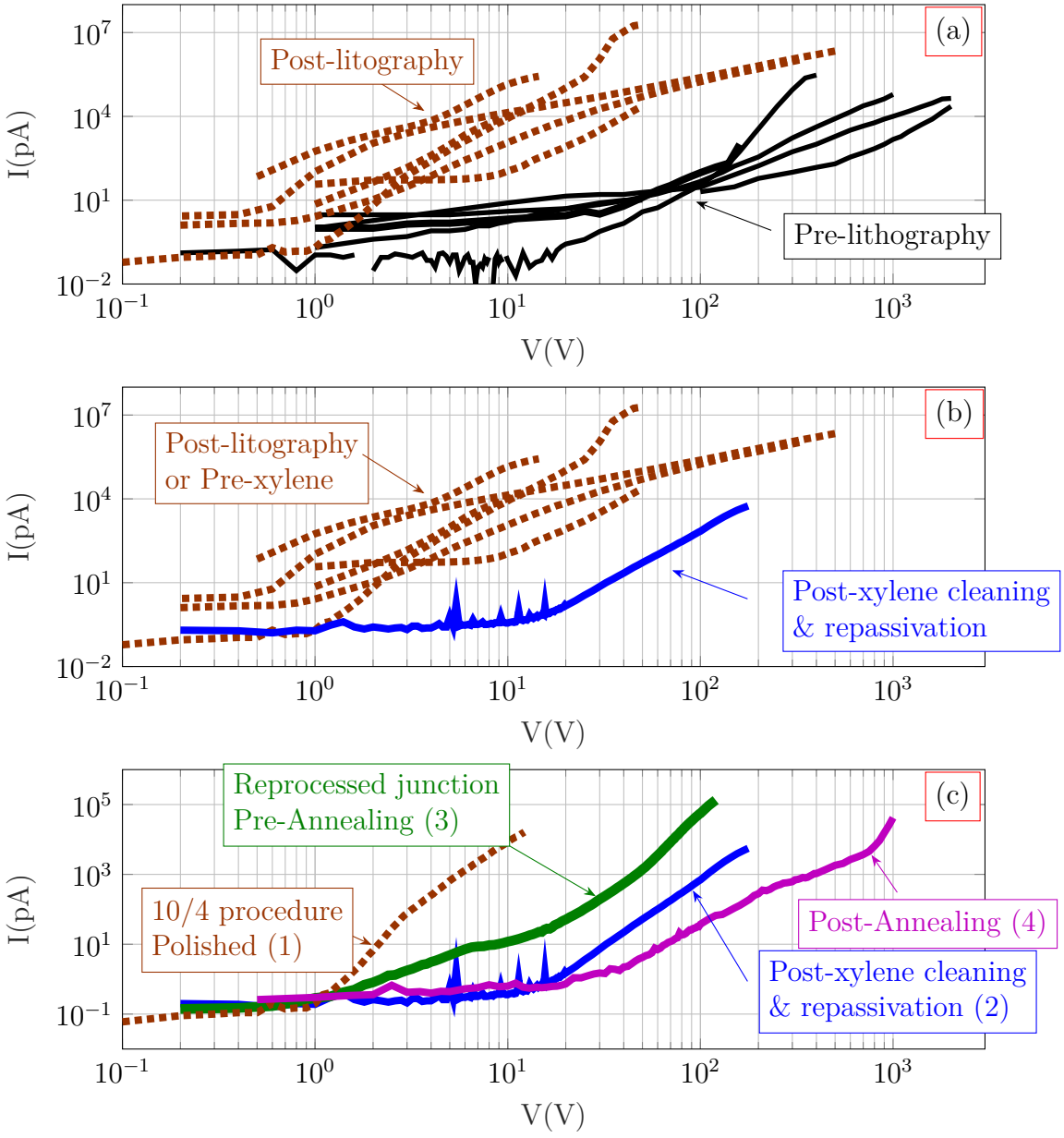

Figure 4.3: *From top to bottom: schematic history of the reversed bias IV characteristics associated with the various reprocessing of the crystal Head 23*

4.1.3 Effect of the Xylene cleaning

After a study on adhesive contamination of the scotch kapton, a new cleaning procedure was adopted using xylene, IPA and acetone. This procedure has given good results as it has returned again to the first family of curves. In fact, after cleaning and subsequent repassivation of the lateral surface of the diode previously processed, the breakdown voltage has increased in absolute value by approximately one order of magnitude.

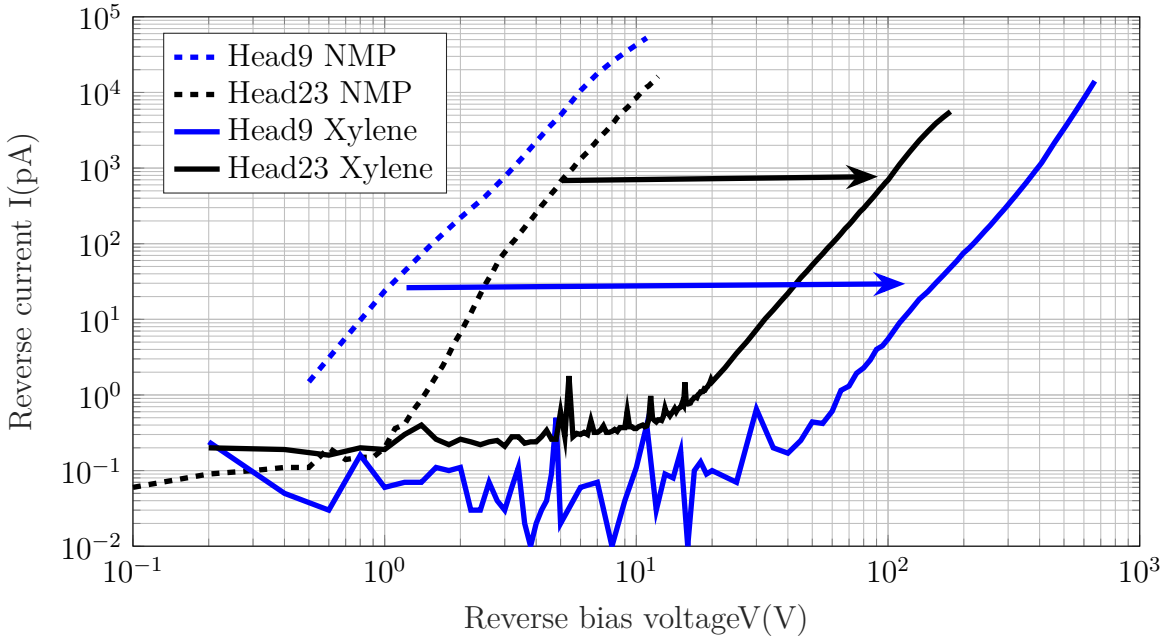

Figure 4.4: *Comparison of the reverse characteristics for two identical cyclindrical detectors Head 23 and Head 9 related to the cleaning process before passivation etching with N-Methyl-2-pyrrolidone (dotted curves) and Xylene (continuous curves); there is an improvement in the curves due to this optimization with an increase in the breakdown voltage of an order of magnitude; all the curves in the figure refer to the 10/4 doping procedure*

This could mean that the previous breakdown to about -1 V occurred on the lateral surface and was not a junction defect as one might think. However, a subsequent reprocessing of the junction gave slightly worse results than the previous ones. One of the reasons could be the non-cleaning of the polished germanium substrate before the deposition of Al / Ge and the subsequent laser melting. Even after an annealing process of the diode followed by a repassivation in methanol, this curve has improved, taking it among those of the first family (see fig.4.3(c)).

4.1.4 Effect of polishing and junction formation optimization procedure

In this paragraph we compare the 40/2 procedure (i.e. by using 2 nm of Al source plus 40 nm of amorphous Ge protecting layer) with the 10/4 procedure performed on polished surfaces.We make notice that the reported I-V results on sample that does not have lithography process or that were decontaminated from kapton glue if refurbished after lithography. In Fig 4.5 I show the diode apperance after p+ junction formation), a clear difference can be seen between the 40/2 nm doping procedure (half image on the left) and the optimized 10/4 nm polished one (half image on the right) on cylindrical n-type HPGe.

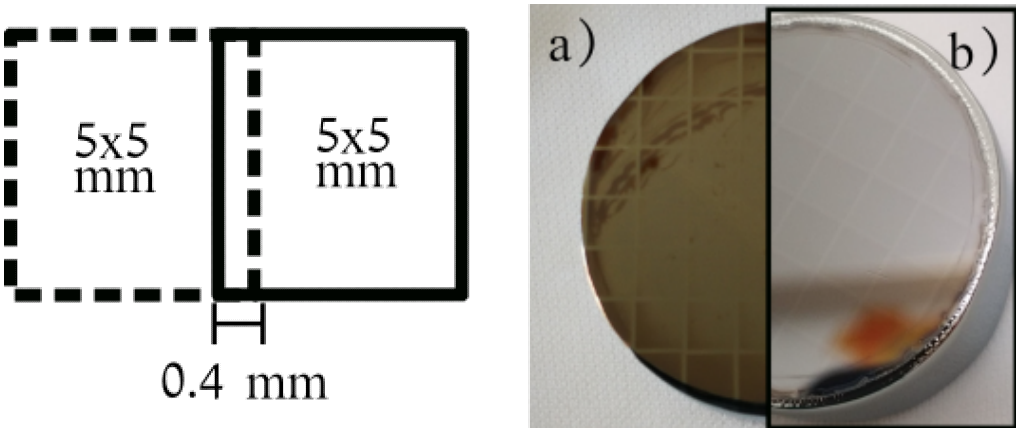

Figure 4.5: *On the left: laser spot pattern scheme with 0.4 mm overlaps between one spot and the next. On the right: visual comparison between lasered junctions with doping procedure: a) Al/a-Ge 40/2 nm; b)polished & Al/a-Ge 10/4 nm*

The visual comparison shows an improvement in the surface gloss which is due to the reduction of ablations with the introduction of the 10/4 procedure, and to the homogeneity of the laser treatment thanks to the polishing of the substrate before deposition. It is worth to note that the dark brown stripes in the middle top of fig a) once observed with a stylus profilometer shows localized ablation about 40nm deep. The optimized 10/4 doping procedure and its advantages in terms of better morphology and limited oxygen contamination have been described in the paragraph 3.1.
We repeated the two procedures several time and characterized the I-V characteristic curve. The figure 4.6 shows the I-Vcurves for a comparison between the 40/2 and 10/4 procedure. A substantial difference between the two is that in addition to the different thickness of the dopant layers deposited before the laser treatment, they have a different surface preparation; the surface for the 40/2 nm deposit had been prepared by etching the HPGe substrate with $HF : HNO_3$, while for the 10/4 nm procedure the substrate was prepared by polishing.

Looking at the two families of curves it is not possible to say that the 10/4 polishing process has introduced an improvement of the I-V performances. All the curves present a over linear trend that starts at about some tens of V. The breakdown onset is not reproducible. All the curves reach 100pA current at above 100V with the exception of one of the 10/4 family. Before breakdown (below 20-40V) most of the 40/2 curves have an about linear increase of the current indicating a small ohmic contribution before breakdown occurs. Due to this trend before breakdown current is in general better for the 10/4 polished sample with values close to the current detection limit) than for the 40/2 ones. One could suppose that the ohmic trend in 40/2 samples could be due to the ablation that exposes a small portion of the surface to ohmic contact with the indium metal pad that we used for contacting the junction in the test. On the other hand the polishing and 10/4 optimized procedure appears to have no systematic influence on the breakdown. .

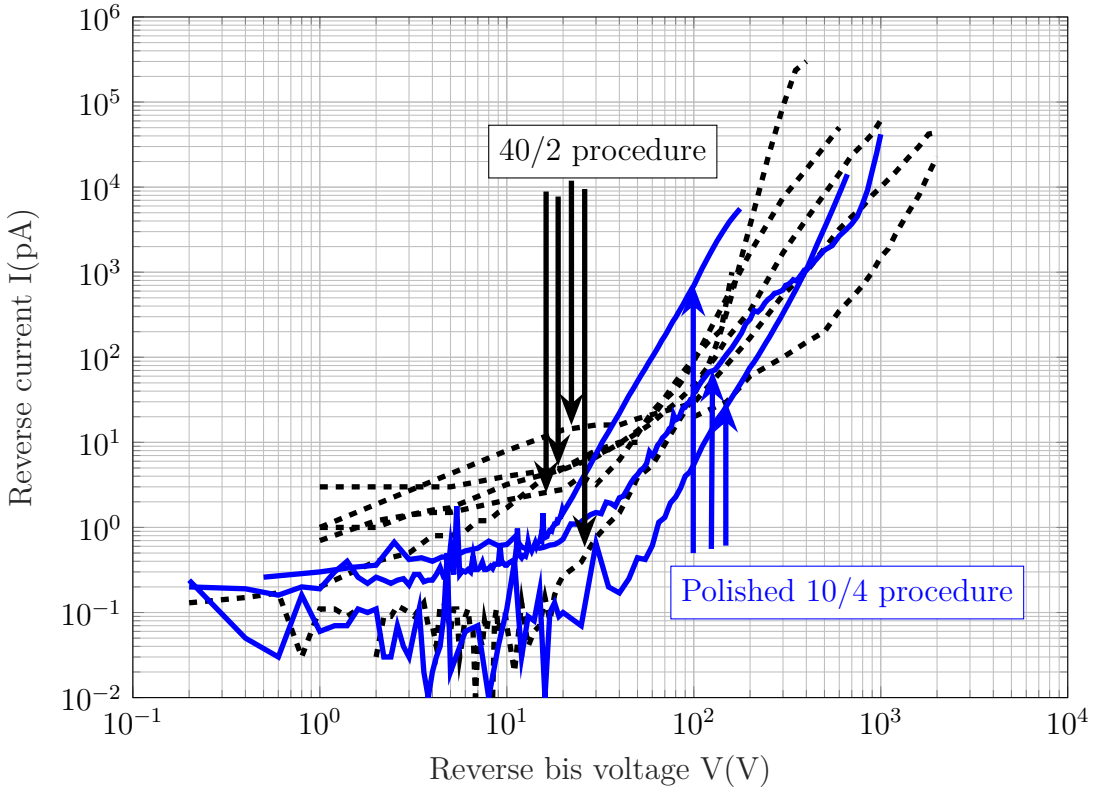

Figure 4.6: *Comparison between the best IV curves related to the 40/2 procedure and those related to the optimized 10/4 procedure with polished surface*

We will see that a more significant effect on the electrical measurements of the optimized 10/4 nm procedure emergs, after the metallization of the contact for the implementation of the guard ring presented in the next paragraph.

4.1.5 Guard ring implementation

The effects of optimization for junction formation are very visible in electrical measurements after contact metallization for implementation of guard ring and a central contact (Fig.4.7). As illustrated in chapter (**??**), a substantial morphological dif-

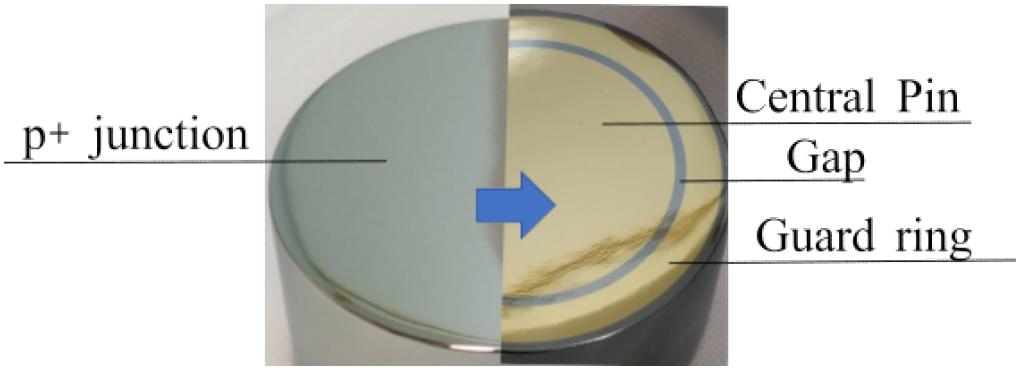

Figure 4.7: *On the left an image of a Head cylindrical detector with processed junction p+/n; on the right an image of the detector after the lithographic segmentation of the junction, for the formation of an external concentric guardring to a central circular contact*

ference between the doping procedures 10/4 and 40/2 is the optimization of of ablations and the reduction of material accumulation at the spot border. More in detail, we have seen, again in the chapter, that the ablations appeared in large spots in the case where 4nm of Al was deposited before lasing, they were reduced to small holes of a few nanometers in the case of the 40/2 procedure and became much less frequent and rarely visible in the case of procedure 10/4.
If the contact is metallized with gold deposition (100nm) and if ablations are present, we do expect that junction could be electrically compromised since an intimate contact between the conducting metal and a semiconductor with compromised jucntion is performed; this is one of reason why research has been done on the morphological optimization of the junction, the subject of the thesis of my colleague Pietro Argenton.
The gold particles could in fact penetrate inside the ablations creating a conductive passage that short-circuits parts of the junction. In fact, if these defective parts are spatially small, the rectifying contact responds with a counter-mechanism of depletion underlying the defective part (ablation with internal gold). Furthermore, depending on the type of underlying crystal, the deposited gold parts can form MS junction portions if the crystal is p-type while ohmic contacts in our case; in any case, the breakdown voltage of the pn junction would be compromised.

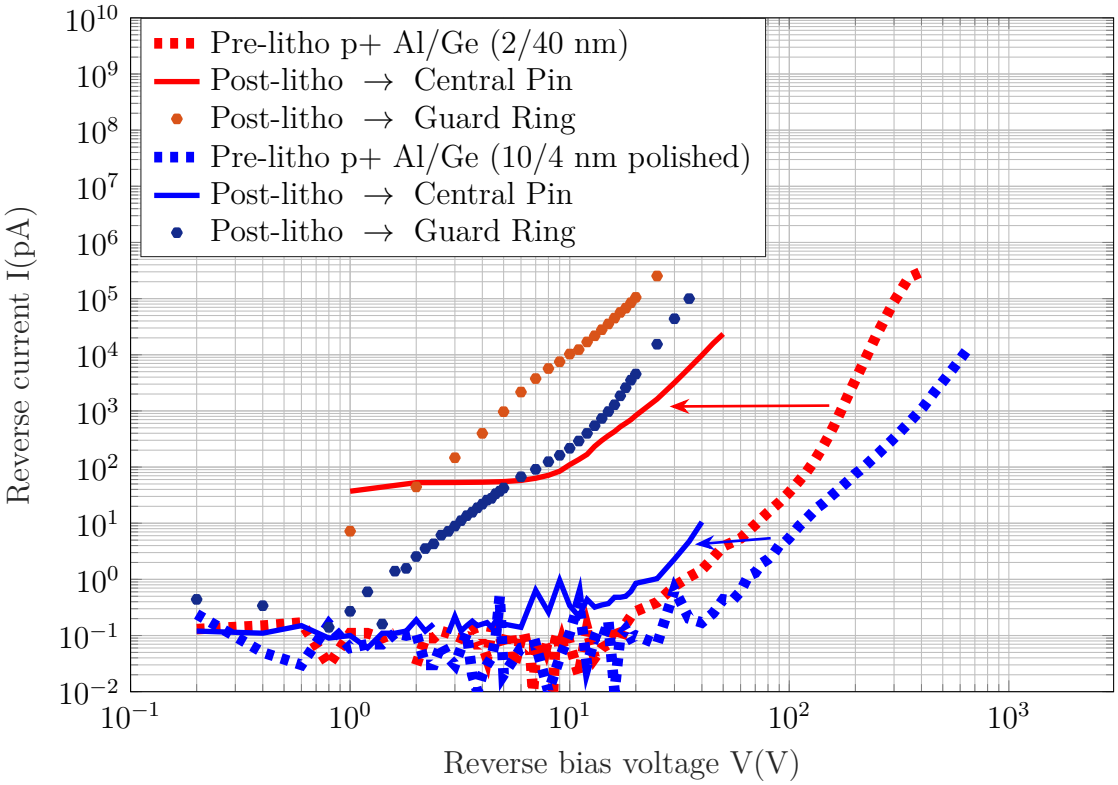

Figure 4.8: *Comparison of reverse IV curves for the two processes Al / Ge (40/2 nm) and Al / Ge (10/4 nm) before and after lithographic metallization; the electrical measurements confirm the morphological optimization of the Al / Ge process (10/4 nm) as after the lithographic metallization, the presence of non-ablated areas, keep the trend of the central-pin IV almost unchanged*

4.1.6 Summary tests of the various optimizations on Head 9 crystal

The head 9 is the twin crystal of the head 23. It was processed recently for the first time, after having optimized the processes by testing them on the head 23 and when, before cleaning with xylene, we thought that the latter had become contaminated by continuing to give unsuccessful results. Fortunately, the head 23 has resumed working again with the same results as at the beginning but in any case not exceeding the 100V breakdown voltage.

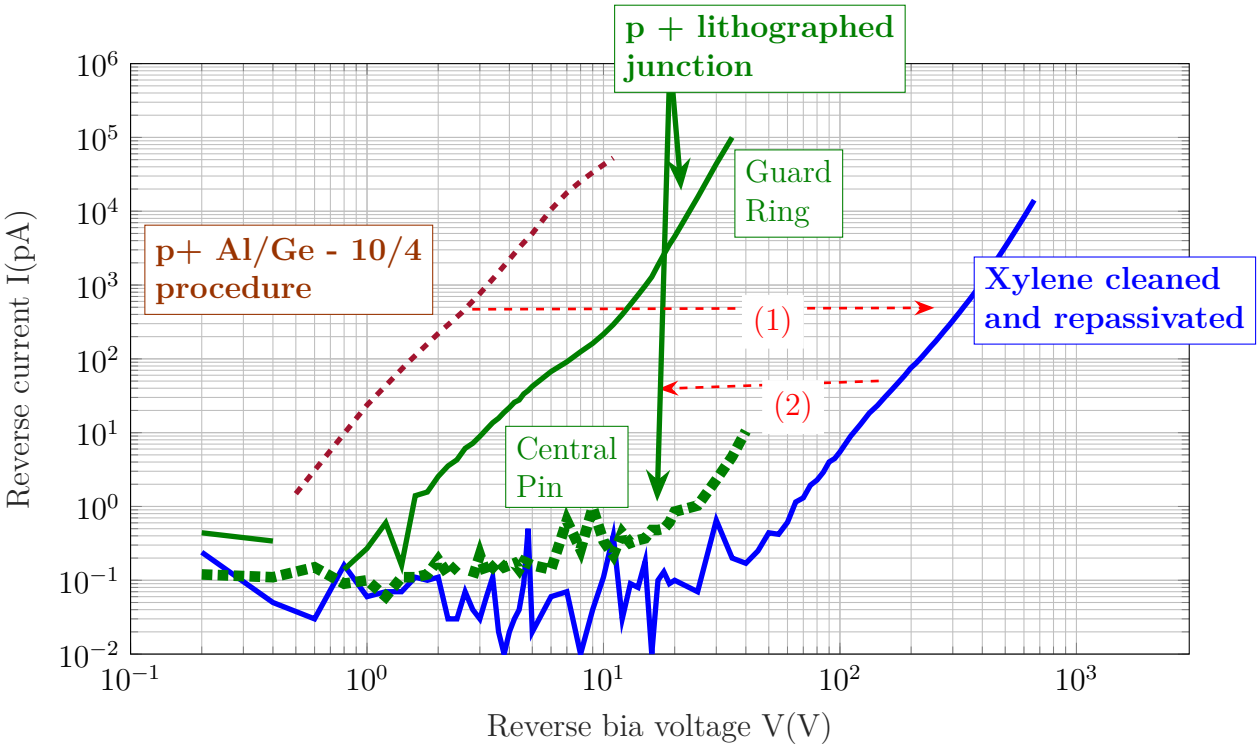

Figure 4.9: *Reverse IV characteristics for the diode the Head 9. The processed diode shows bad behavior, but improves by applying for the first time a methanol repassivation with previous xylene cleaning (1); the creation of a guardring and a central pin compromises the functioning of the junction under the guard ring but preserves that of the central contact (2)*

The first processing of the p+ junction on Head 9 was done using the 10/4 nm optimization procedure. Despite this optimization, the IV curve has a very low breakdown voltage, less than 1V. Applying for the first time cleaning with xylene to the processed diode and a subsequent 3:1 solution of HF/HNO_3 etching and methanol passivation, a subsequent measurement showed a marked improvement with a breakdown voltage of about 5V confirming that the previous breakdown had

occurred on the lateral surface. A lithography on the junction for the creation of a central contact and a concentric guard ring, showed a worsening in the guard ring current but the IV reverse characteristic of the central pin remains almost comparable to that measured previously.

4.2 Prong 1n

4.2.1 Single spot laser-doped junction test

As described in chapter 2.4.2, a junction is made by scanning different laser spots 5x5 mm over a square grid with a partial superposition of the spots. Superpositions along the sides of the squre spots produce areas with double spots, at the corner, areas with 4 spots are produced. During the junction optimisation tests performed in the parallel thesis work of Pietro Argenton, the junction was sucesfully tested with 1 2 and 4 spots. Some problems where met at the very border of even a single spot with the formation of an accumulation zone. This zone is reduced by using the 10/4 GeAl junction doping procedure but is very hard to determine with our experimental technique if the border zone is active. In this section we describe an additional experiment we did in order to determine if spot border effects are crytical for the HPGe detector performances by studying single spot contacts. Moreover this is intersting to disentangle the jucntion breakdown problem since if one of these fails, it compromises the whole junction as it begins to conduct current bringing the diode into breakdown. For this reason it was decided to build a twelve squared-strip n-type HPGe diode in which each of the twelve p + junctions are processed with a single laser spot and isolated eliminating by lithograpy the border of the spot.

This analysis allows the individual spot junctions to be assessed without overlapping effects of laser spots during junction processing.

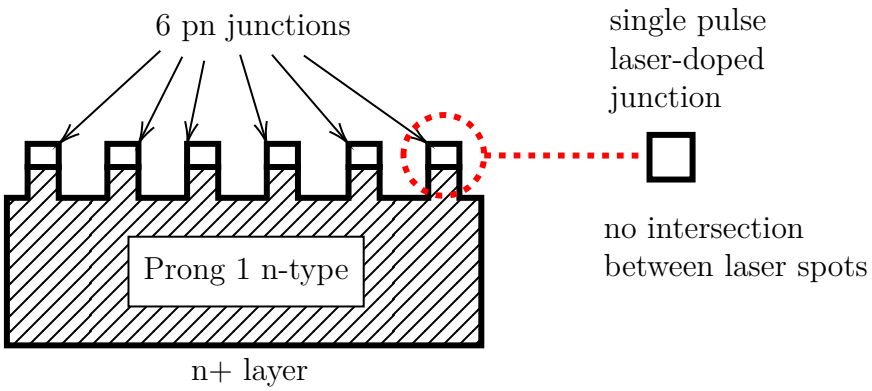

Figure 4.10: *Schematic of the 1n prong processed with rectifying contacts on single non-overlapping laser spots. The photo has already been shown in the Fig. 2.14*

The twelve lasered junctions are distributed to two groups of six spots in which each group falls on opposite sides of the same surface of the Prong 1N; this will allow the measurement of six spots at a time, since there are only six contact clips available for measuring the reverse IV characteristics .

4.2.2 Reverse IV charateristics analysis

In this case, the analysis of the characteristic curves highlights the quality of the individual lasered spots, separated from each other; this will lead us to have a statistic on how many spots the junction was well formed for our purposes and in which others the junction failed. Since the junction, which subtends the spot, must be optimised for reverse polarisation operation, the quality will be determined by the higher breakdown voltage that can be reached. In figure 4.11 the six laser contacts are measured during inverse polarisation. Voltage is applied to the n+ contact while all the contacts C1 to C6 are at ground with the exception of one of them that goes to ground through the picoammeter. The measure was repeated 6 times one for every contact (blue to bold green lines). Total current is also measured connecting by the picoammeter used to polarise. Dashed blue line is performed with contacts from 1 to 5 to picommeter and 6 to ground. A **compliance** value of **100 nA** has been set to prevent too high currents from contaminating the hyperpure crystal.

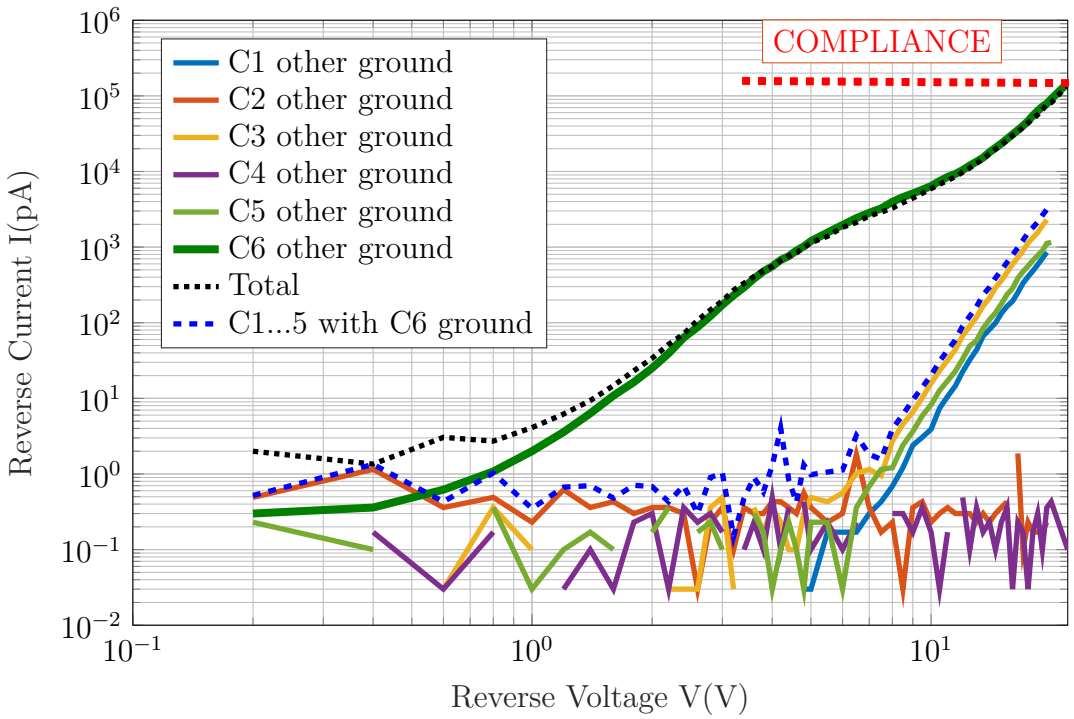

Figure 4.11: *Reverse IV characteristics of the six single spot junctions of the Prong 1N; the dotted black line corresponds to the total current while the dotted blue line corresponds to the short-circuit current of the segments C1 C2 C3 C4 C5*

Let's see immediately from the plot (Fig 4.11):

- a failure of the single spot C6 junction as the breakdown voltage is less than 1V and the reverse current is 100 nA at 20V.

- The single spot junctions corresponding to C1, C3, C5 separately, show almost the same behavior with a breakdown voltage of about 7 V and reverse currents of 1 or 2 nA at 20 V

- The best quality single spot junctions correspond to segments C2 and C4; unfortunately it is not possible, until now, to obtain the voltage and the breakdown currents for these contacts because the maximum current compliance value does not allow to extend the measurements to higher voltages. For this reason, a method has been applied to detect the breakdown voltage of these segments which I will describe below.

Measurement of the breakdown voltage of segments C2 and C4

As said before, the current compliance value reached by contact C6 at 20 V does not allow to measure currents at higher voltages and therefore does not allow to obtain the reverse IVs of the best contacts C2 and C4 to determine their breakdown voltages; in other words, the current of C6 does not allow to perform the subsequent measurements.

The simplest way to overcome this problem is to put C6 in a floating configuration with the other segments grounded. In this floating C6 configuration, since C6 cannot dissipate the current to ground, it will discharge towards the nearest segment C5. In fact, as can be seen in the figure, a current measurement of the common contact C1...C5 configuration with floating C6 is higher than the current on the common C1..C5 with C6 grounded precisely because the current of C6 will go to ground through the passivation resistance between C6 and C5.

The current flowing from C6 to C5 grounded is generated by an unknown reverse bias potential on the C6 floating contact and by the resistance between C6 and C5; this potential arises between the V = 0 of the segments and V> 0 of the underlying n + contact. The result is that in the C6 floating configuration, the total current is lowered because the C6 does not discharge directly to ground. Furthermore, the common contact C1 ... 5, which in this configuration has a higher current and buffers the current of C6 through the resistance between C6 and C5, at a certain point follows the current trend of the segments in the configuration in which C6 is grounded , when the breakdown occurs. So this is a good way to lower the currents and push forward with the voltage.

In general, therefore, we tried to put in floating configuration the "low voltage brakdown" contacts to limit the output currents and therefore go to the breakdowns of the best segments C2 and C4 that previously could not be seen due to the high currents at the limit of compliance.

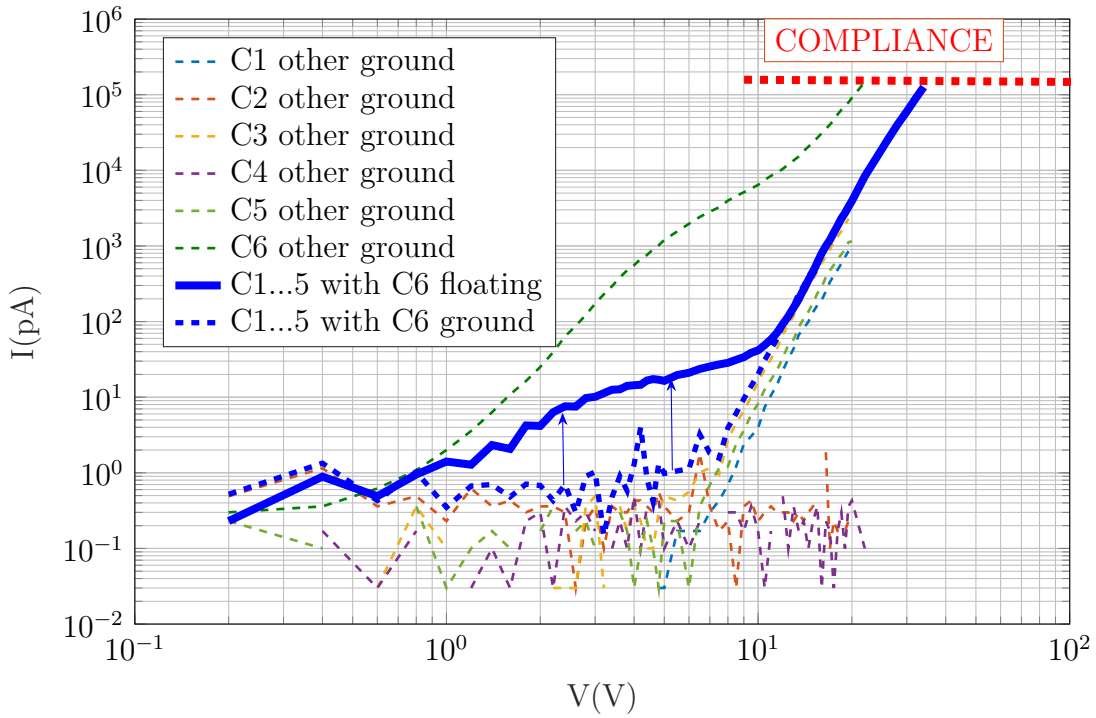

Figure 4.12: *Reverse IV characteristics of the six single spot junctions of the Prong 1N;the dotted blue line corresponds to the short-circuit current of the segments C1 C2 C3 C4 C5 with C6 grounded, while the blue solid line corresponds to the short-circuit current of the segments C1 C2 C3 C4 C5 with C6 floating. It is evident that the raising of the continuous blue curve with respect to the dashed one is due to the fact that contact C6 is in breakdown and, in floating configuration, discharges current on the closest contact C5 towards ground.*

We have put all contacts in floating configuration except C2 and C4 of which the common reverse current was measured.

As in the previous case, the common current of C2 and C4 will include the currents of all the other floating contacts, which flow to ground through the passivation resistances between the contacts themselves. At this point the breakdown of the common contact C2 and C4 at 100V can be due to C2 (and the breakdown of C4 occurs at higher voltages) or vice versa. In general, what you see when you have a common contact with multiple segments is the breakdown of the worst segment at lower voltages.

To understand which of the two segments this breakdown corresponds to, it is therefore necessary to make two measurements individually for the two configurations (figure 4.15):

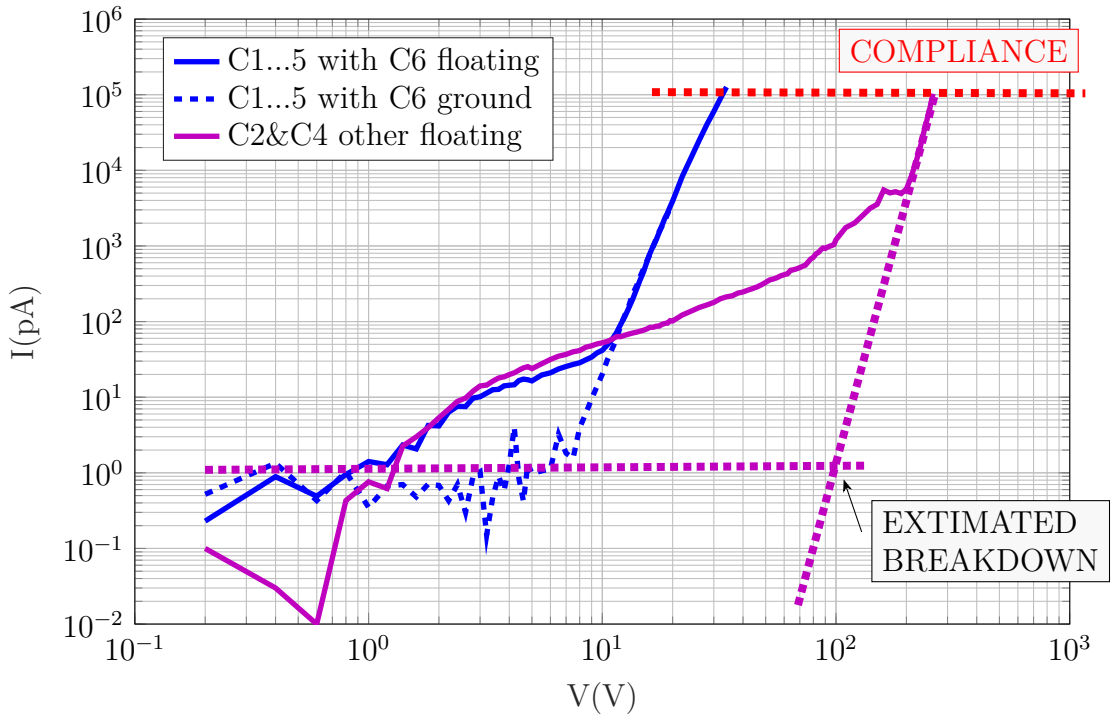

Figure 4.13: *Estimated breakdown voltage of the short-circuit contact C2 & C4 in the configuration with other floating contacts. The rise of the purple curve is due to the current that the floating contacts discharge (in breakdown) on contacts C1 & C2 towards ground.*

1. C2 grounded and the other floating (yellow)

2. C4 grounded and the other floating (green)

It is then seen that both C1 and C2 present a breakdown at the same reverse bias voltage since the individual current measurements on each segment while all the others are floating, show a rise in the curve with a change in slope due to the breakdown of the each measured segment.The present results are relevant for our understanding of the p+ laser junction performances in HPGe even if they are not conclusive about the origin of the breakdown of the laser annealing junction produced on HPGe. As can be seen the single spots contacts have a non uniform behaviour having breakdown from 1 to 100V. We can exclude that the spot borders of germanium accumulation fig 3.5, are the only reason of the breakdown in the multi-spot junctions, if fact it was so, we would have seen an improvement of the breakdown, being the border region of the spot completely etched away with the lithography process.

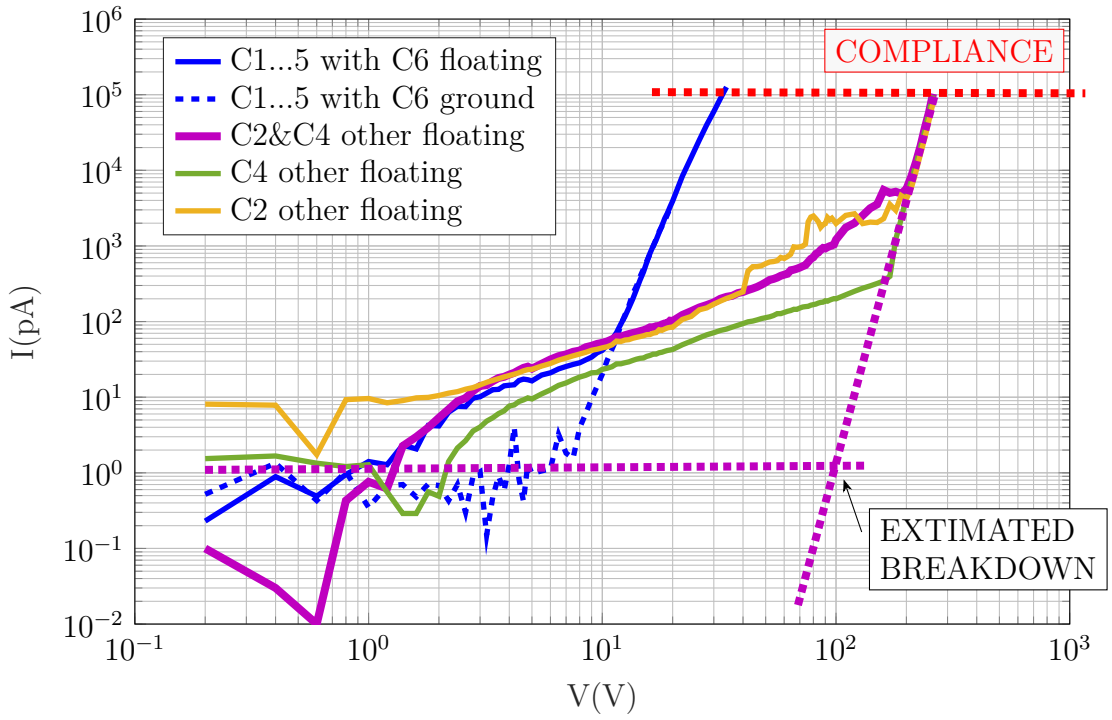

Figure 4.14:

Figure 4.15: *Estimated breakdown voltage of the contact C2 (or C4) in the configuration with other floating contacts. The rise of the purple curve is due to the current that the floating contacts discharge (in breakdown) on contacts C1 & C2 towards ground.*

Two main ideas are still candidates to be the reason of the breakdown. It may be a failure due to the intrinsic nature of the laser junction i.e. the current may come from the inner area of the spot, or it may be due to imperfection of the lithography border. As it was described in chapter 3.2 we have not yet solved the problem of the under-cut due to the aggressive passivation/trenching etching we actually use. Therefore metal canopies are also present in this PRONG 1n prototype. On the other breakdowns in the range of 10s of volts are obtained when multi-spots large detectors Head23 and Head 9 (having 49 and 64 spots respectively) are tested before the lithography process. One could conclude that in the lithography free detectors the problem is the superposition while in the single spot the problem is the lithography border. This is not a simple explanation and some more information can be given only by improving the lithography border production of this first single spot diode prototype.

The main future working plan is to use Reactive Ion Etching process, that is a

plasma etching under ion bombardment to improve vertical opening of the trenching. On the side of possible bulk effect in the inner area the research group is working trying to see if low temperature annealing of the junction may improve the quality of the junction at melt depth. Literature data show that vacancies could accumulate at the melt depth and the could be annealed even at relatively low temperature.

Intercontact resistivity

In appendix A, we report further tests that we performed on the Prong1n prototype in order to measure the intercontact resistivity. This is quite an interesting point to understand the performance of passivation but not only: in addition to the standard method, we have implemented a new method of measuring the resistances in case one or more segments are in a breakdown regime, ie it is a confirmation of the leakage mechanisms that we expect. For consistency with the order of presentation and not to lose the thread of the discussion, I report the discussion in appendix A, but this section is also very important.

4.3 Reverse I-V characteristics as a function of temperature

In this section we report about some measurements we performed in order to better understand the behavior of the diodes that we produced. The idea is to measure the I-V characteristic curves as a function of the temperature starting from liquid nitrogen temperature, at which the diode normally operates, up to room temperature. A special automatic set-up was developed. Automatic repeated I-V measurements are performed while the cryostat is warming-up after the liquid nitrogen (LN) in the cryostat is exhausted. The warming up of the cryostat is very slow and is continuously monitored by a thermoresistance, it takes about 12 hours from LN to room temperature (RT). An acquisition program that I developed starts a full I-V measurement that takes about (45 minutes) anytime that the temperature increases of a given temperature interval of 5K. During the IV measurements a negligible temperature increase occurs.

With reference to the theory developed briefly in the section, in which the main mechanisms causing leakage current and their temperature dependence were discussed, we tried to analyze our reverse I-V-T data and the activation energies for an Orthec test detector, compared with a PLM-processed Head, in order to understand the mechanisms responsible for leakeage.

4.3.1 I-V-T measurements on a standard detector

Two detectors are measured by varying the temperature according to the described methodology. The 805 detector is an Ortec commercial detector from the early 90s; more precisely it is a n-type coaxial detector.
The p + type junction is made by implantation of Boron and shows the reverse IV characteristic plotted in figure 4.16. As can be noted in the log-log scale the detector present a breakdown at around 200V where the current starts to increase over-linearly since the current increase of more than one order of magnitude as a result of an increase of less than an order of magnitude in the voltage. At voltage bellow 100V the current is very limited and slowly increase with the voltage.
Afterwards, the detector was slowly warmed up and the I-V curves was collected at different temperature. In Fig. 4.17 the I-V curve taken every $\Delta T = 5K$ are displayed. As can be noted the current generally increases with the temperature, and the trade-off between the sub-breakdown and over-breakdown regions becomes less and less visible increasing T. This means that sub-breakdown current increases faster with temperature than breakdown current. Below breakdown a slight dependence on the voltage is present. For temperature above -140°C the log-log plot shows that current increase by about half an order of magnitude while voltage increases of 2. These means a power law trend roughly as $V^{0.25}$.

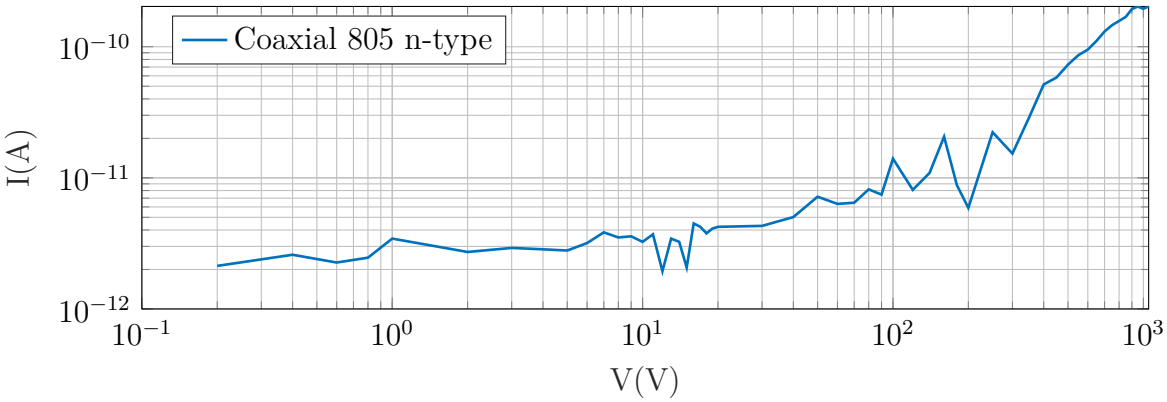

Figure 4.16: *Reverse IV characteristics of the detector 805 n at T = 90K*

In order to deeper understand the trend, I produced a further plot by reorganizing the same data. The log of the current at a fixed voltage was plot against the reciprocal of the temperature 1/kT, where k is the Boltzman factor. This is the so call Arrhenius plot. In case a single phenomenon activated by temperature Arrhenius plot evidences the activation energy that can be directly obtained by the slope of a linear fit to the data. In 4.18 the Arrhenius plot by increasing the voltage is reported. As can be noted at lower voltages up to about 200V a single linear trend is visible. Above 200V, that correspond to about the breakdown voltage, the trend is mode complex, and it is no more reproducible by a single straight

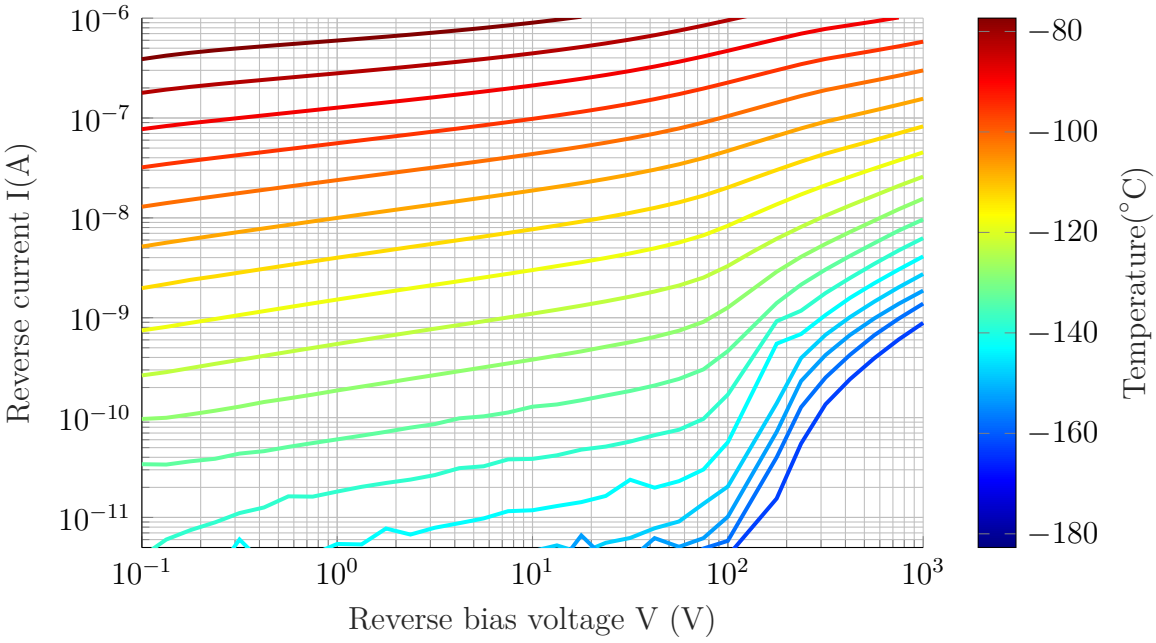

Figure 4.17: *805 n detector- reverse IV characteristics for various temperatures.*

line. Most probably breakdown current contribution of the surface passivation or of some parts of the junction are superimposed to the below-breakdown contribution in this regime.
All the curves of 4.18 are fitted by a straight line and the slope are reported in Fig. 4.19. The activation energy at low voltage is 0.45 ± 0.01eV and slightly decrease until breakdown. Above breakdown threshold voltage (200V), the activation energy is not perfectly defined being not associated to a linear Arrhenius trend but is a sort of average between the breakdown current activation energy (theoretically zero) and the main mechanism activation energy. The decrease of activation energy with voltage above breakdown threshold is therefore quite pronounced and reasonable.

For the sake of completeness, the derivatives of the Arrhenius plot are shown in the figure 4.20

The 0.45 eV activation energy is lower than the energy gap and may suggest a trap limited mechanism involving traps that are not exactly at the middle band (that would give 0.35eV being Eg=0.7 at LN temperature). The fact that the current increase slowly than 0.5 power low with the voltage does not correspond an ideal RHS model but make think that a trap assisted tunneling is not probable being in that case the V dependence with a power law higher than 0.5. Instead, the breakdown is most probably due to a worsening of the passivation due to possible contamination or radiation damage of the passivation after many years of operation.

This data set, performed on a crystal build with a standard B implanted junction, is an interesting benchmark to be compared with our diodes produced by PLM. In the following paragraph we show the same set of measurements performed on one of our p+ junction performed on the cylindrical crystal Head23.

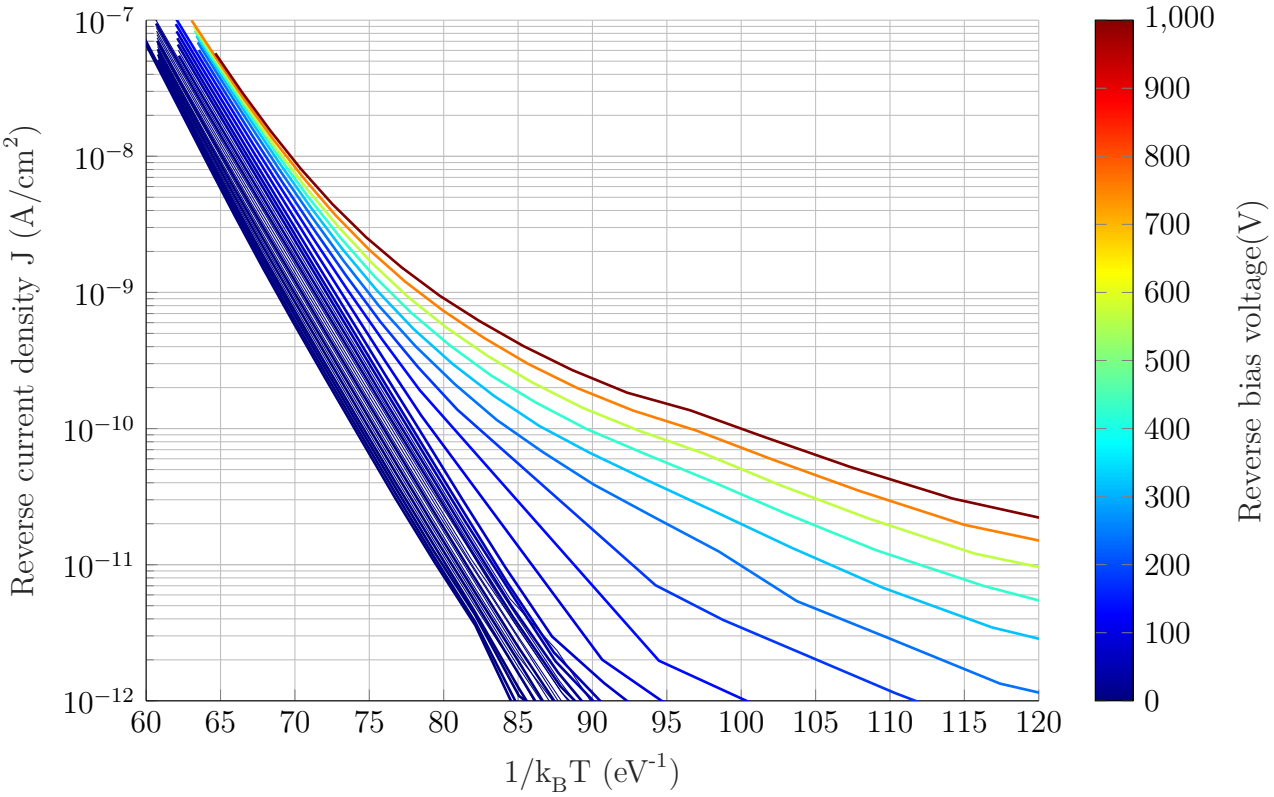

Figure 4.18: *Arrhenius plot for coaxial detector 805 n*

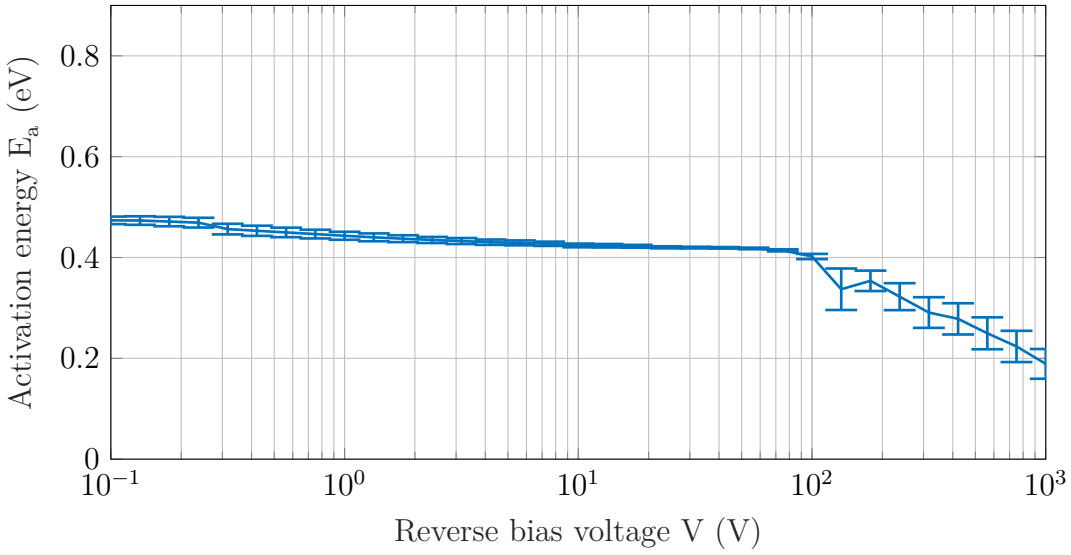

Figure 4.19: *Activation energies as a function of reverse bias voltage for coaxial detector 805 n*

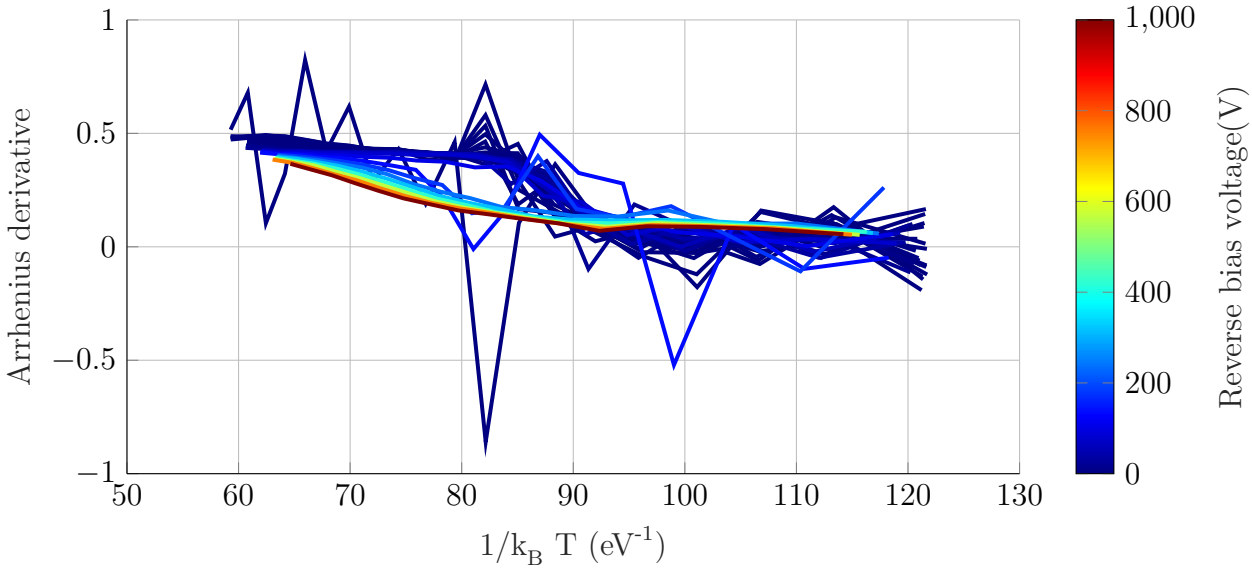

Figure 4.20: *Arrhenius derivative for the detector 805 n*

4.3.2 I-V-T measurement on a p+/HPGe laser diode

In Fig. 4.21 reverse IVs at different temperature for one of the Head 23 PLM-processed are displayed. This measurement is taken on a sample processed with 40-2 Al/Ge p. As can be noted the curve at lower temperature present a very low breakdown threshold. As a matter of fact, this particular sample was is one of the sample of the so call "brown family" of Fig. 4.3 that we discovered was affected by surface contamination and does not received the Kapton decontamination in its production. The Arrhenius plot for different voltages is reported in 4.22 , while

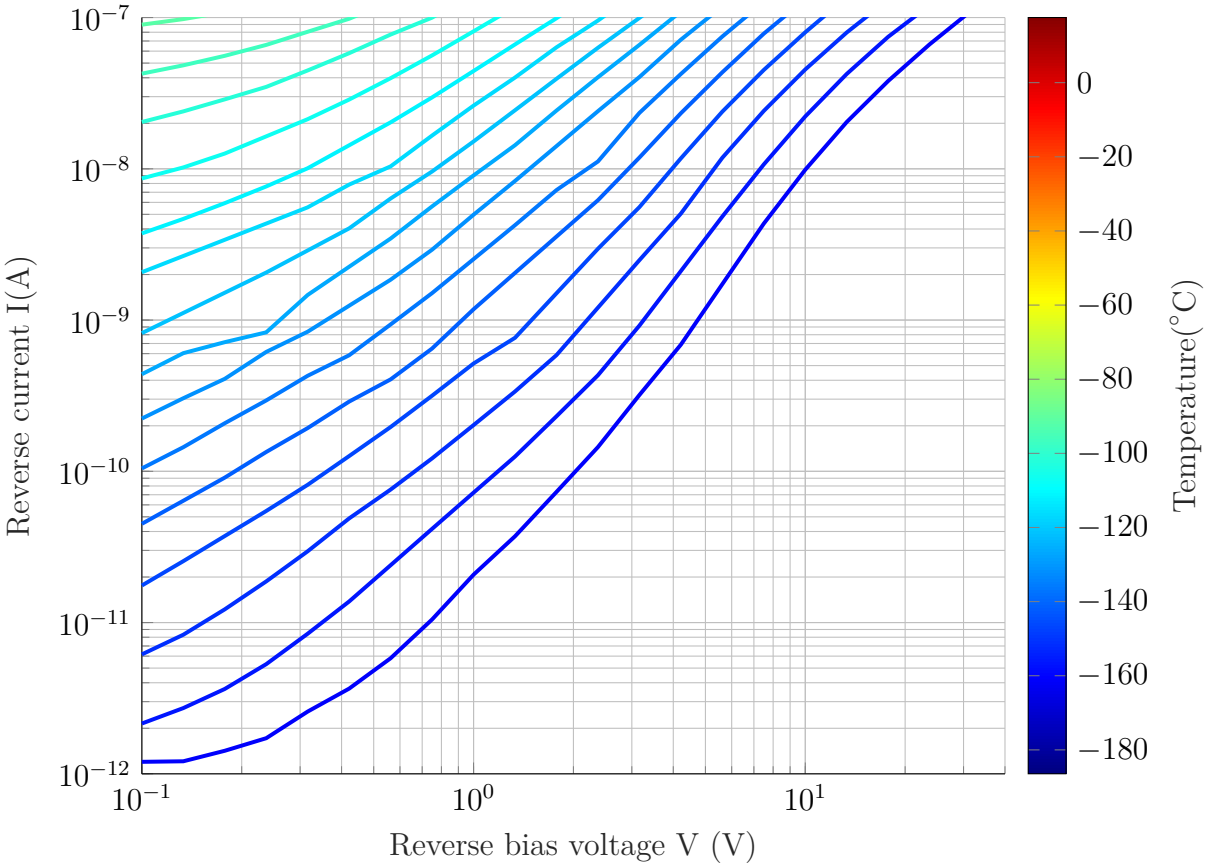

Figure 4.21: *Temperature-dependent reverse IV measurements of the p + junctions processed on one of t he n-type Head 23 crystal processed with PLM doping procedure 40/2 nm and pulse energy density 500mJ/cm* ^{2}

the activation energies obtained by linear fit are in 4.23. In this case the activation energy has a single decreasing trend with the voltage since the breakdown threshold is at very low voltage.

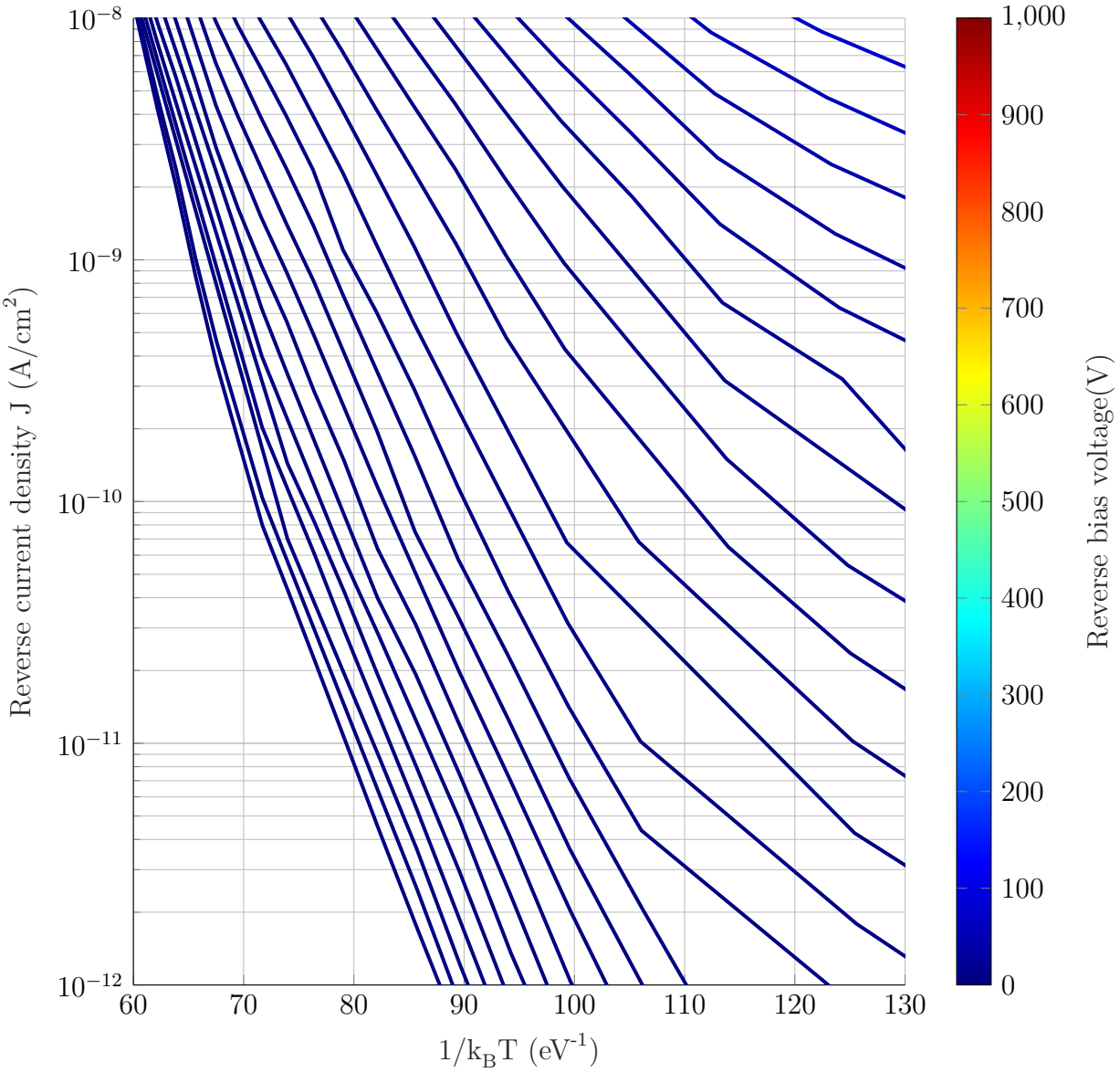

Figure 4.22: *Arrhenius plot for the a-Ge/Al junction*

It is worth to note that the activation energy at very low voltage is in agreement with what obtained with the previous "standard" detector i.e 0.43 ± 0.04 eV. Notwithstanding that this measurement has to be repeated in the future in a detector having a higher breakdown voltage, if confirmed, this result would suggest that the leakage current mechanism in PLM p+ junction is very similar to what

obtained with B implanted standard junction. We make notice that the eventual trap assisted generation that we hypothesize on the basis of these preliminary data, comes from the depletion region and that the very large portion of the depletion region is inside the HPGe material due to the high doping of the p+ region. These means that the traps that mediate the generation mechanism are characteristic of the HPGe material not of the produced junction, this is in agreement with the fact that the same activation energy is obtained for Laser and standard p+ junction production.

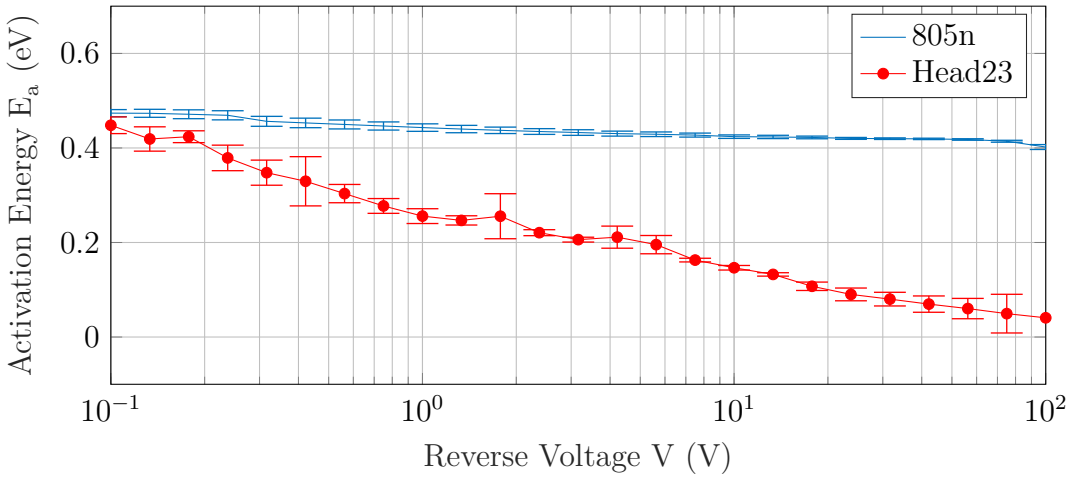

Figure 4.23: *Comparison of activation energies for the detector 805 and the processed Head*

Chapter 5

Conclusions

In this work, many aspects relevant to the manufacturing of HPGe large volume detectors with shallow junctions processed through the pulse laser melting technique have been analyzed.

A submicrometric junction of this type easily lends itself to chemical segmentation and the manufacturing technique preserves the underlying HPGe crystal from contamination, with excellent spatial control of the doping process. The PLM (pulse laser melting) technique is illustrated in chapter 1, in which the various phases of the procedure to create highly doped junction have been described. Some small thickness detectors (<2mm) with n +/p junction have already been tested with good results as illustrated in Chapter 2; we therefore tried to improve the manufacturing for large volume detectors that must be subjected to very high reverse polarizations (2400V) compared to those of small thickness (24V) for the complete depletion of the volume. The high polarization and the resulting maximum electric field at the junction put a strain on the junction, on the passivation and on the manufacturing techniques that were used askingaskingig for an improvement of quality, accuracy and contaminant control.

For this reason, starting from Chapter 2, the various steps for the manufacturing of the large volume HPGe diode at the Legnaro laboratories were described, presenting some examples of processed and segmented junctions,. In chapter 3 we presented the material science approach to various possible process optimizations (improvement of the junction formation, improvement of the surface starting morphology by polishing, improvement of the trenching, decontamination of the sample) while in chapter 4 we present the tests of process modification mainly by studying the I-V characteristic curve. A first step regards the improvement of the p+ junction production that is formed by means of a Al thin layer dopand source covered by an amorphous Ge protecting layer. The thickness of the protecting layer is optimized to improve surface morphology that may be detrimental for doping. A 10nm protecting layer thickness prevents oxygen contamination of the junction and maintains a continuous surface morphology with reduced border effect on the

laser spot. Higher thickness (40nm) causes accumulation of material at the spot border and some ablation along the surface. The 10 and 40 nm protecting layers were tested by producing HPGe diodes. While the optimized junction production seems not to affect the junction performance when not covered by metallic layer, after the metalization the 40 nm junction induces a strong increase of the leakage current even at low voltage, while the junction obtained with 10nm protecting layer does not dramatically worsten after metallization. The idea is that metallic contact may induce a strong worsening of the junction when it covers the ablated areas. .

Another important improvement of the process that we tried to introduce, was the polishing of the surface which made it possible to obtain more homogeneous surfaces after the laser treatment. We investigated a very effective procedure based on chemical mechanical polishing without abrasive components. The roughness reduction is in general an important aspect for the process reproducibility, our starting hypothesis was that it could be important for homogeneity of the laser junction and possibly reduce leakage current and breakdown effects. As a matter of fact not a strong improvement of the performances was obtained. Finally, I have shown that HF: HNO3 etching (used for segmentation and as a first step for passivation) creates some problems for segmentation; in particular, it forms canopies and undercuts to the gold metallized coating of the segments at the segment-gap interface. We have therefore tried to study a new etching, 3HP, which is very precise in the trenching of germanium. Unfortunately we discovered that the etching is very sensitive to the highly Al doped Germanium resulting in a very slow and inhomogeneous etching of this material. Effect of doping on echiants is reported in literature and it is due to the electron (or holes) availability for the chemical reactions that may influence their velocities, but it was not reported for this particular etching and was not revealed for B doped germanium in previous experiments performed by our group. Even if it is not suitable for the purposes of segmentation, therefore, it can be used in other etching phases on non-doped HPGe, as it maintains a great level of precision on the excavation compared to the previous etching. Furthermore, the results I have reported regarding the effects of 3HP on doped germanium, can give in the future information on the composition of the doped surface (for example if there are amorphous nanolayers or aluminum microclusters on the surface), but this further development requires other measures and a deeper study on the chemistry of the reaction. In order to improve the trenching process Reactive Ion Etching is being investigated , even if a new method for passivation should be investigated as well once the chemical route is abandoned.

The control of contaminants is essential for the success of a diode; after several months in which the electrical measurements showed a worsening of the processed diodes which we thought was irreversible, a study was dedicated to decontamination, in particular from that of the kapton glue, resistant to acids and solvents previously used; an interesting result of this study shows that in particular conditions of controlled temperature, a mixture of solvents can pulverize the silicone glue

and that this powder evaporates inside a vacuum chamber. This study allowed us to identify a decontamination procedure that showed excellent results, and allowed us to compare the other types of optimizations that were previously not visible due to the detrimental effect of this contamination. We think that kapton glue contamination removal is very important because it prevents a correct passivation of the surface since it induces protection from the acid attacks.

A very peculiar test was carried out on a diode whose rectifying contacts were obtained by segmentation, on single non-overlapping laser spots. This test allowed us to understand the role of the overlap between the spots on the overall effect of the junction and the reproducibility of the techniques used for the construction of these contacts. An analysis with some floating breakdown contacts was used to derive the breakdown voltage of the best segments avoiding very high currents that could have contaminated the crystal. The intersegment resistances were also measured with a standard procedure; to verify the validity of the theoretical hypotheses of the ongoing process previously used (to derive the breakdown voltages of the floating contacts), the floating curves were used to derive the resistances between the contacts with a new method derived from the our hypothesized model; these resistances obtained with the two methods are in perfect agreement. The results from this interesting trail are not still conclusive. As a matter of fact breakdown voltages are not better than what obtained for junctions with overlapped spots, but we have to take into account that this first test was performed with the standard lithography process that may have "canopies" on the gold layer that possibly induce lateral breakdown. The test will be repeated after improvement of the segmentation process.

Finally, the characteristic curves as a function of temperature were analyzed for a factory-implanted boron detector and for a detector built by us with the PLM technique; the acquired data have been reordered to obtain current curves as a function of temperature. From these we obtained the Arrhenius plots which gave us important information about the mechanisms that dominate the reverse polarization leakage and allowed us to compare them to those of the factory detector.

Although these results are very encouraging, the optimization processes are still in progress and the optimal results will be obtained by completing the improvement of the construction processes, the quality of the junction and the use of new etching and passivation procedures that will allow more control over the segmentation.

Appendix A

Intersegment insulation

The aim of this chapter is to test and apply a method to measure the inter-segment resistance when there is a depletion region above them. In this situation the resistance will be dominated by the surface current and will be the higher the higher is the efficiency of the electrical passivation process.

A.1 Measurement of intersegment resistances by unbalancing the potential between the contacts in reverse bias condition

The configuration adopted for measuring the surface resistance between two neighboring contacts is based on two main assumptions:

1. the two neighboring segments must be depleted in the same way if there is a zero potential difference between them. To do this, a potential V_{com}= 2 V is applied to pin n + when the two segments are both at potential 0; this ensures a sufficient depletion which prevents currents from pin n + towards the segments; the other segments are physically connected to ground.

2. Once the previous configuration has been set, the V_{seg} potential of one of the two segments varies in a small range of values both above and below 0 V, making sure that in total the segments always remain reversed biased; for each value of Vseg of a segment, the currents of the other segment at V = 0 are measured.

In our case we chose a reverse voltage on the n + contact V_{com} = 2V, set one of the two segments to zero voltage, and we measured the current on it by varying the voltage of the neighboring segment between 0 and 1 and between 0 and -1.

If the junctions are depleted then, by varying the potential at the first segment, we will measure a change in current on the second segment, whose voltage is fixed

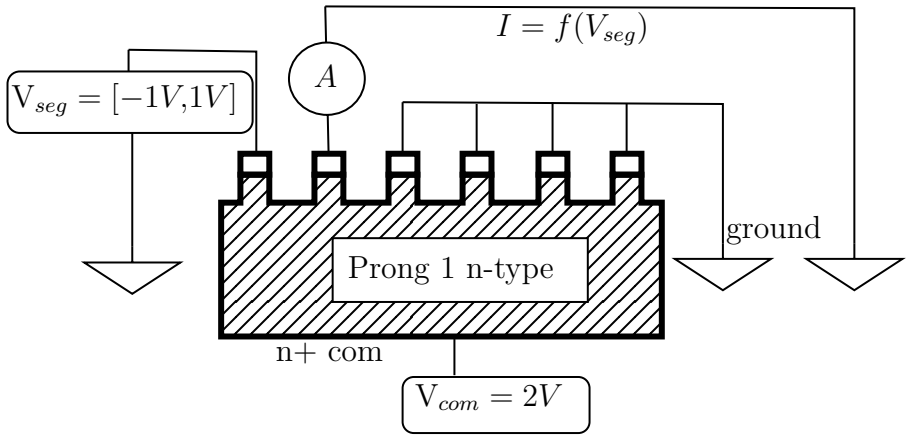

Figure A.1: *General scheme for measuring the resistance between two segments; the current variation on a grounded contact is measured by biasing the neighboring contact. As can be seen, all the other segments not involved in the measurement are grounded and the two involved in the measurement are kept counter-polarized by the potential on the common contact n + throughout the measurement process.*

at V = 0, which should discharge on the first segment through the surface resistance between them. In fact, if the potential on the first segment were not changed, the current variation due to the interaction between the two segments would not be measured on the second segment.

A fundamental condition is that both junctions must be depleted under their breakdown voltage with $\Delta V_{depletion}$ = V_{com}-V_{seg}> 0 and $\Delta V_{depletion}$ <$V_{breakdown}$. In fact, if one of the segments set at V_{seg} = 0 (for example the second) is measured in over the breakdown, the measured current (associated with the voltage variation Vseg on the first segment) will not correspond only to that which passes through the surface resistance between the two segments because one of the two diodes is not working as intended. The result in this case is an always negative current "reduced" by breakdown-operating diode under the second segment .

Therefore, given a measurement setting with S1 and S2 in the configuration given above, *the resistance measurement between the segments is not symmetrical by exchange of S1 and S2* if one of the junctions is above its breakdown voltage value. Let's see the results: the figure A.2 shows a V-I plot of the currents of a grounded segment as the voltage of the neighboring segment varies from -1V to 1V. These measurements are always in reverse bias as a voltage of 2V is applied to the common n + contact.

According to the provisions, the resistance measurements between the voltage unbalanced contacts are all compatible if a common reverse bias voltage is applied, except for contacts C5 and C6, since C6 is in breakdown regime.

The resistance between C3 and C4 is too great to be measured with the same

Vseg	Imeas	$R_{interseg}(\Omega)$ for $V_{seg} < 0$	$R_{interseg}(\Omega)$ for $V_{seg} > 0$
C2	C1	$(8.4 \pm 0.5)10^{11}$	$(8.3 \pm 0.3)10^{11}$
C5	C4	$(6.6 \pm 0.4)10^{11}$	$(5.9 \pm 0.5)10^{11}$
C6	C5	$(2.6 \pm 0.2)10^{12}$	$(1.1 \pm 0.1)10^{12}$
C5	C6	$(6.9 \pm 0.3)10^{11}$	$(5 \pm 0.4)10^{10}$
C3	C2	$(3.9 \pm 0.2)10^{11}$	$(2 \pm 0.3)10^{11}$

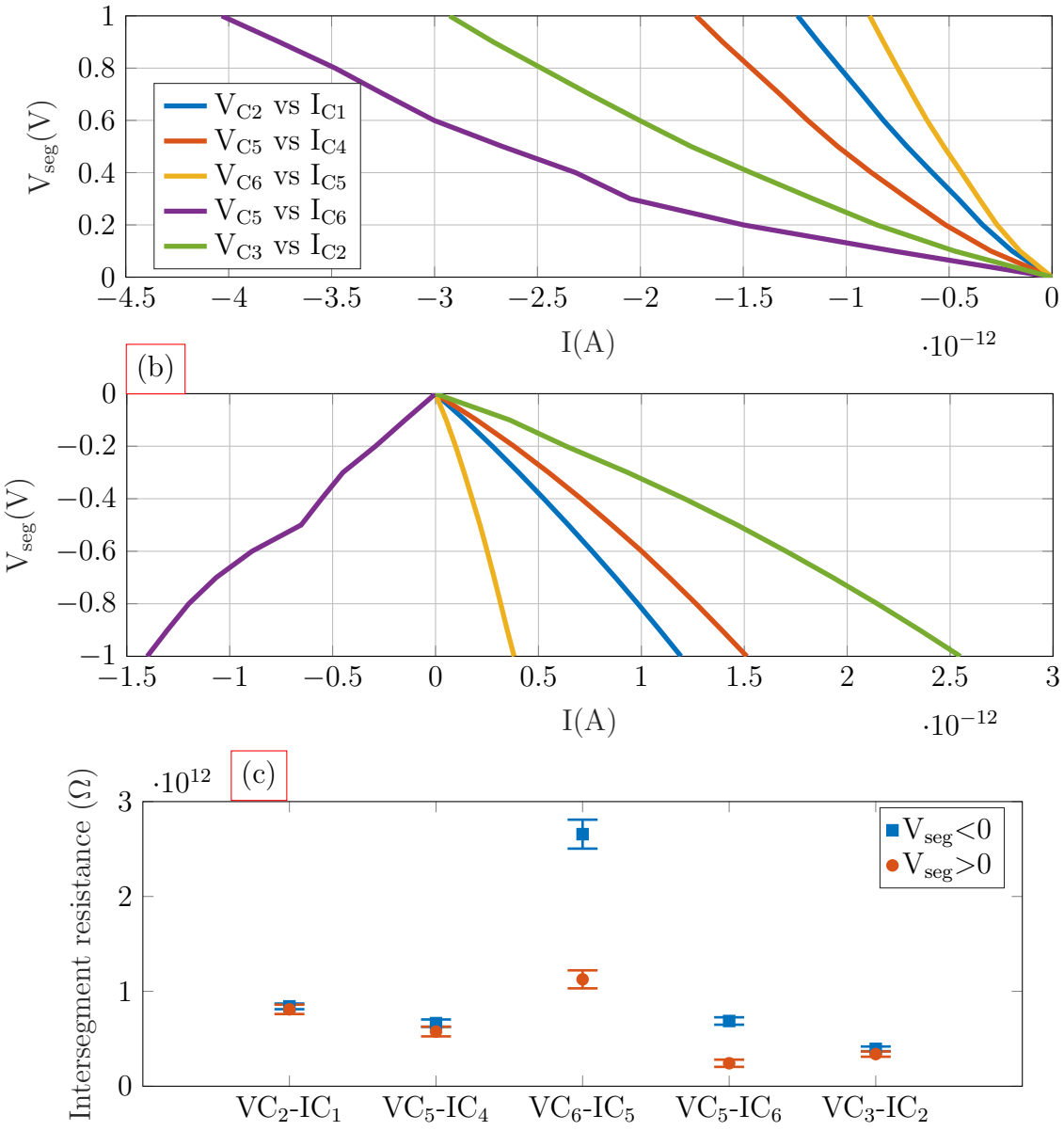

Figure A.2: *From top to bottom: currents measured to ground for each segment as a function of the polarization of the near segment (Vseg) in the configuration where all other contacts are grounded and a reverse bias potential of 2 V on the opposite common contact is applied : in the first plot (a) Vseg = [0,1] in the second plot (b) Vseg = [0, -1]; The third plot (c) shows the intersegment resistances calculated from the fits and compares those obtained from Vseg> 0 and Vseg <0 for each intersegment resistance configuration.*

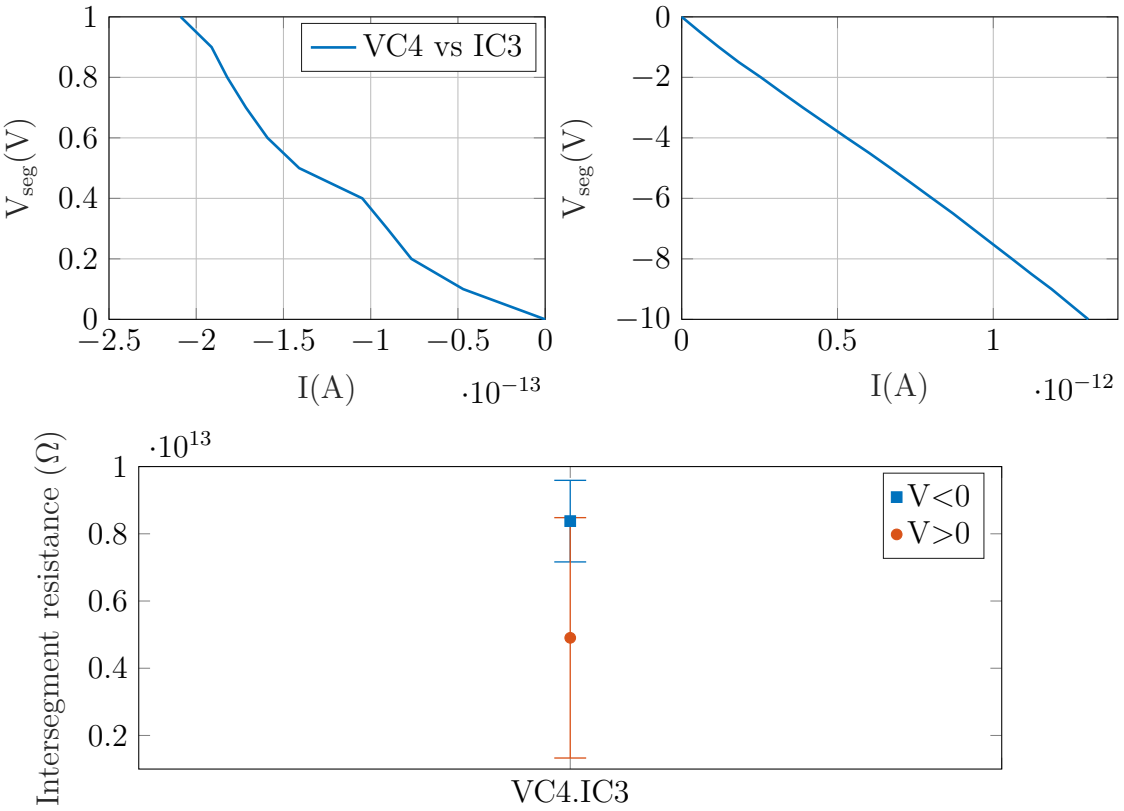

Figure A.3: *Evaluation of the intersegment existence between contacts C3 and C4 by measuring the current on C3 by biasing C4 in total configuration of reverse bias*

procedure as the others. In fact, the measured current (<pA) is below the Keithley current resolution limit. To measure a reasonable value of current on C3 we have to polarize contact C4 step by step at voltages up to -10V for negative voltages. For positive polarizations of C4 instead we stop at 1V to keep the diode in reverse polarization; for positive voltages, therefore, we will get a large error bar, but we will make a right of it (see figure A.3). Although the current measurements for $Vseg > 0$ relating to the unbalanced contacts have great uncertainty, it can be said that the resistance between contacts C4 and C3 is in the order of some $T\Omega$

R [Ω] V<0	R [Ω] V>0
$4.8 \pm 3.5 * 10^{12}$	$8.4 \pm 1.2 * 10^{12}$

A.2 Measurement of intersegment resistance with the floating breackdown contact method

Since the intersegment resistance measurements with the previous method are not reliable if one of the segments is in a breakdown regime, we have thought of a way to deal with this situation. As can be seen in the figure A.4, the short-circuit current of segments C1 ... 5 increases if one passes from the configuration with grounded C6 to that with floating C6. This is reasonable because, as already mentioned, the floating C6 current cannot discharge directly to ground but will have to flow to the neighboring segment passing through the intersegment resistance. Remember that C6 is already in a breakdown regime. The passage of the current in the C6-C5 segment is clearly visible in the graph and manifests itself with a resistive behavior that I have indicated as the "Ohmic region". on a loglog scale in fact we have in general that:

$$I = \frac{V}{R} \quad \text{linear scale} \tag{A.1}$$

$$logI = logV + log\frac{1}{R} \quad \text{log-log scale} \tag{A.2}$$

one immediately sees that if Ohm's law holds, the slope of the IVs is always unitary on a log-log scale and the value of the resistance is placed on the intercept. Therefore, using this method it is possible to verify on a log-log scale that the increase of the current in the C6 floating configuration with respect to that of C6 grounded follows an ohmic trend, in a given reverse bias voltage range.

By selecting the interested interval and making a linear fit on linear scale, it is possible to find the intersegment resistance between C6 and C5 (which is equivalent to evaluating the intercept of the fit on a log log scale).

In particular, the resistance is the inverse of the slope b and the error on the resistance $\epsilon(R)$ was obtained by propagating the error of the slope, i.e.

$$R = \frac{1}{b}; \quad \epsilon(R) = \frac{1}{b^2} * \epsilon(b) \tag{A.3}$$

b $[1/\Omega]$	R_{C6-C5} $[\Omega]$
$(3.8 \pm 0.2) * 10^{-12}$	$(2.55 \pm 0.12) * 10^{11}$

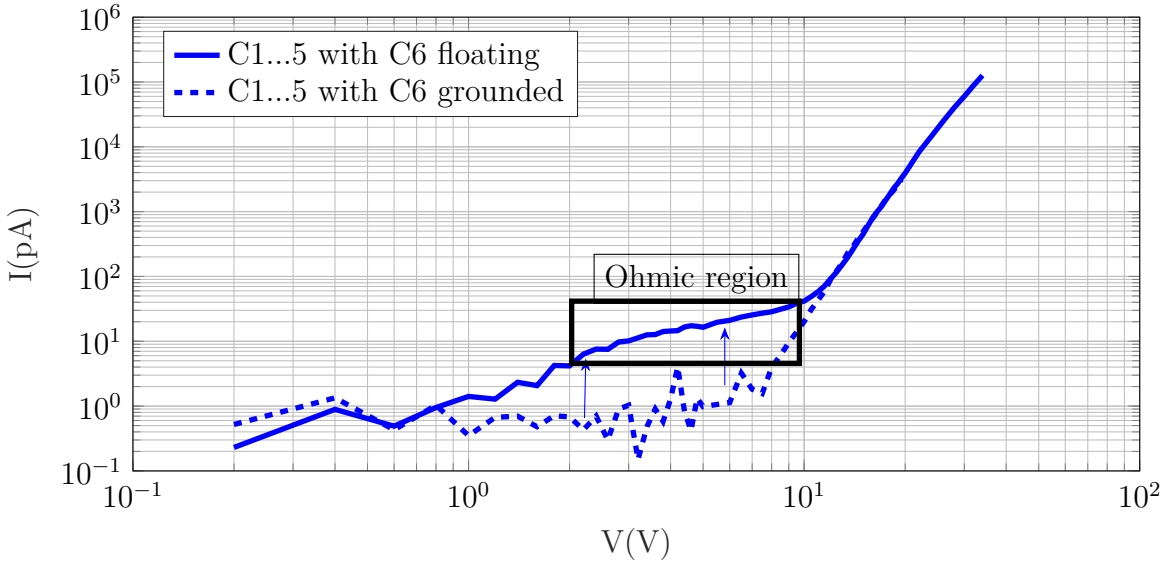

Figure A.4: *IV curves in comparison: short-circuit of segments C1-C5 with C6 grounded (bul dotted curve) and short-circuit of segments C1-C5 with C6 floating (blue continuous curve); in this last configuration there is an increase due to the fact that floating C6 discharges the current towards the nearest contact.A zone with Ohmic behavior is also identified in the configuration with floating C6*

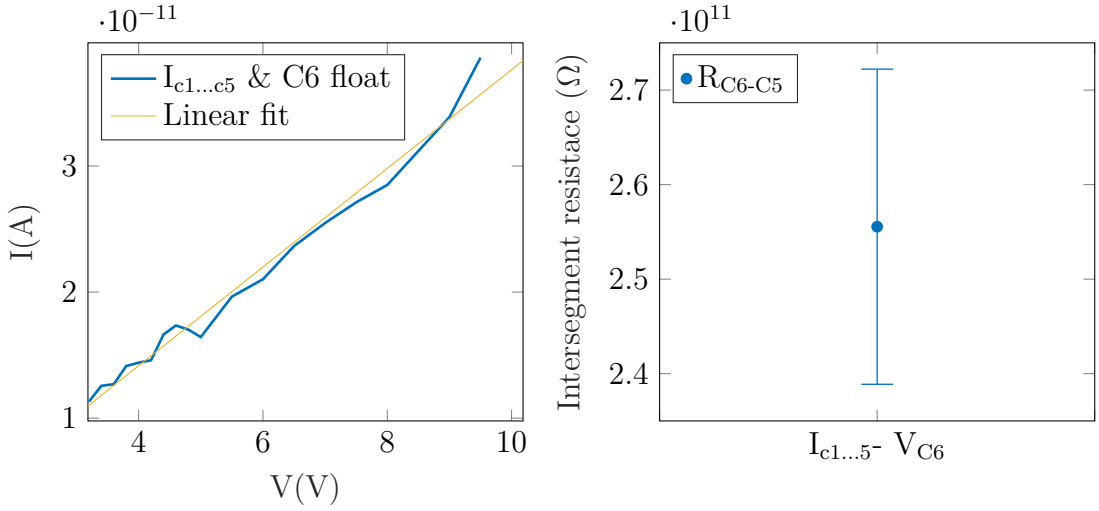

Figure A.5: selection of the ohmic zone in the figure A.4 and fit on a linear scale to determine the intercontact resistance between C6 and C5

A.2.1 Floating contact method: Test of validity

So far we have obtained all the intersegment resistances with the two methods described: the first method (unbalance of the intercontact potential) allowed us to derive the resistance for the junctions not in breakdown while the second method (floating contacts) allowed us to derive the resistance between contacts if one of them was over the breakdown regime. Since the second method was designed to

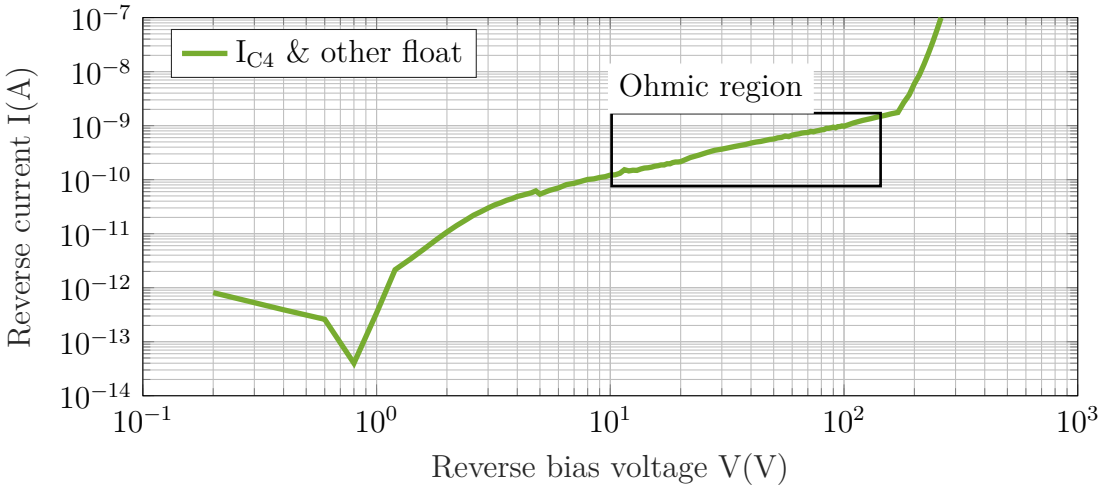

Figure A.6: *Current on segment C4 towards ground with all other floating segments, as a function of the reverse bias voltage of the common contact*

first obtain the breakdown voltages of the best segments (which we would not have reached due to the current in compliance) and then processed for the measurement of the inter-contact resistances, it was decided to perform a validity test by measuring the same resistance with both methods.

Considering that the resistance R_{C3-C4} (calculated with the unbalance potential method) is greater than one order of magnitude with respect to R_{C4-C5}, if we left the contacts C3 and C5 floating the current I_{C3-C4} should be negligible with respect to I_{C4-C5}; The floating contact method should lead to the calculation of the smallest resistance that is R_{C4-C5} if we measure the current on C4 towards ground by placing the other floating contacts and setting as a function of the reverse bias potential on the common contact n+.

By selecting the Ohmic region from the plot (as already done previously) on a loglog scale and bringing it back to a linear scale, it is possible to derive the resistance from the linear fit; the result is shown in the figure A.7, which also shows the resistances measured with the method of the unbalanced potential.

As can be seen, the different methods for the calculation of the resistance R_{C4-C5} are consistent and this demonstrates the validity of the floating contact method for measuring the inter-contact resistance in the configuration where one of these is in

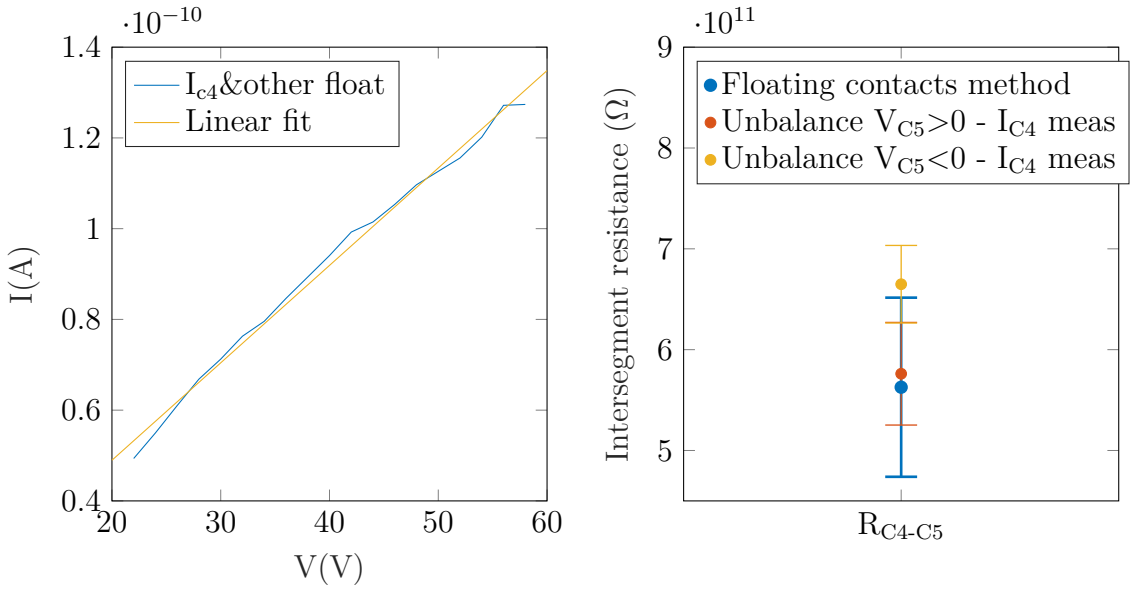

Figure A.7: *Right: Ohmic region on a linear scale and linear fit. Left: resistance calculated with the floating contact method (blue), and with the unbalanced potential method V_{C5}> 0 (orange) and V_{C5} <0 (yellow) with C4 grounded*

breakdown.

Appendix B

Matlab codes for Keithleys automation

B.1 Two-keitheley IV measures

```
%implementato da Alessi/date 17/12/2020
%Vpol,Ipol 237 bottom
%Ijunc     237 top      only read clear all;
clc;
filename=input('Insert filename:','s');
date=clock;
hold off;
pause(1)
%indirizzi sistemati bott 16 top 8
Keithley237_BOTTOM = instrfind('Type', 'gpib',
 'BoardIndex', 0,
  'PrimaryAddress',16
   'Tag', '');
Keithley237_TOP = instrfind('Type', 'gpib', 'BoardIndex', 0,
 'PrimaryAddress',8, 'Tag', '');
if isempty(Keithley237_BOTTOM)
Keithley237_BOTTOM = gpib('NI', 0, 16);
else
fclose(Keithley237_BOTTOM);
Keithley237_BOTTOM = Keithley237_BOTTOM(1);
end
if isempty(Keithley237_TOP)
Keithley237_TOP = gpib('NI', 0, 8);
else
```

```
fclose(Keithley237_TOP);
Keithley237_TOP = Keithley237_TOP(1);
end

fopen(Keithley237_BOTTOM);
fopen(Keithley237_TOP);

clrdevice(Keithley237_BOTTOM);
clrdevice(Keithley237_TOP);
set(Keithley237_BOTTOM, 'Timeout', 20);
set(Keithley237_BOTTOM, 'EOSMode', 'read&write');
set(Keithley237_TOP, 'Timeout', 20);
set(Keithley237_TOP, 'EOSMode', 'read&write');

fprintf(Keithley237_BOTTOM,'F0,0O0L9e-7,0B0,0,0T0,0,0,0P4R1N1Y0K0G15,0,0X');
 %Lcompl in questo caso 300 nm se-7
fprintf(Keithley237_TOP,'F0,0O0L9e-7,0B0,0,0T0,0,0,0P4R1N1Y0K0G15,0,0X');%
flushoutput(Keithley237_BOTTOM);
flushoutput(Keithley237_TOP);
pause(5);
tic();
%  Output_Keithley=strsplit(query(Keithley237_BOTTOM,'X'),',');
out=query(Keithley237_BOTTOM,'X');
Output_Keithley=strsplit(out,',');
Measure_Prefix_bottom=cell2mat(Output_Keithley(3));
i_pol=str2double(Measure_Prefix_bottom(6:end));




out=query(Keithley237_TOP,'X');
Output_Keithley=strsplit(out,',');
Measure_Prefix_top=cell2mat(Output_Keithley(3));
i_jun=str2double(Measure_Prefix_top(6:end));
 %ho corretto in data17/12/2020 prima era Measure_Prefix_top(6:end)
V_pol=0;
OffsetCurrent=["tempo","Vpol","i_pol","i_jun";toc(),V_pol,i_pol,i_jun];
plot(V_pol,i_pol,'k.');
hold on;

while abs(V_pol)<=1100
%set the maximux value of vpol, doesn't matter the sign
```

```
if (abs(i_pol)<6e-7 && abs(i_jun)<6e-7)
%control of the maximum value of current
if (abs(V_pol)>=0)&&(abs(V_pol)<=4.9)

passi=+0.2;%inserisci il segno
%misura IV da cavo HV con keithley bottom,( ).
fprintf(Keithley237_BOTTOM,['B',num2str(V_pol),',0,0X']);

%inserisce il nuovo valore di vpol dopo ogni ciclo
pause(20);

out=query(Keithley237_BOTTOM,'X');
%ipol da trattare, bisogna escludere le lettere che non servono
% e prendere solo la musura.
Output_Keithley=strsplit(out,',');
 %separa i valori tra le virgole in celle
Measure_Prefix_bottom=cell2mat(Output_Keithley(3));

%converte il valore della cella in un singolo carattere
i_pol=str2double(Measure_Prefix_bottom(6:end));

 % escludo le lettere iniziali e converto in double

out=query(Keithley237_TOP,'X');
Output_Keithley=strsplit(out,',');
Measure_Prefix_top=cell2mat(Output_Keithley(3));
 %corretto itop,bottom, prima erano scambiati anche
 %se non dovrebbe cambiare nulla
i_jun=str2double(Measure_Prefix_top(6:end));
OffsetCurrent=[OffsetCurrent;toc(),V_pol,i_pol,i_jun];
plot(V_pol,i_pol,'--k.');
V_pol=V_pol-passi;
elseif (abs(V_pol)>4.9) && (abs(V_pol)<=19.9)
passi=0.2; % cambio i passi
fprintf(Keithley237_BOTTOM,['B',num2str(V_pol),',0,0X']);
%inserisce il nuovo valore di vpol dopo ogni ciclo
pause(10);
out=query(Keithley237_BOTTOM,'X');
Output_Keithley=strsplit(out,',');

 %separa i valori tra le virgole in celle
Measure_Prefix_bottom=cell2mat(Output_Keithley(3));
```

```
%converte il valore della cella in una singola matrice
i_pol=str2double(Measure_Prefix_bottom(6:end));

% escludo le lettere iniziali e converto in double



out=query(Keithley237_TOP,'X');
Output_Keithley=strsplit(out,',');
Measure_Prefix_top=cell2mat(Output_Keithley(3));
i_jun=str2double(Measure_Prefix_top(6:end));
OffsetCurrent=[OffsetCurrent;toc(),V_pol,i_pol,i_jun];
plot(V_pol,i_pol,'--k.');
V_pol=V_pol-passi;
elseif (abs(V_pol)>19.9) && (abs(V_pol)<=99.9)
passi=0.5; % cambio i passi
fprintf(Keithley237_BOTTOM,['B',num2str(V_pol),',0,0X']);

 %inserisce il nuovo valore di vpol dopo ogni ciclo
pause(30);

out=query(Keithley237_BOTTOM,'X');
out=query(Keithley237_BOTTOM,'X');
Output_Keithley=strsplit(out,','); %separa i valori tra le virgole in celle
Measure_Prefix_bottom=cell2mat(Output_Keithley(3));

%converte il valore della cella in una singola matrice
i_pol=str2double(Measure_Prefix_bottom(6:end));

 % escludo le lettere iniziali e converto in double

out=query(Keithley237_TOP,'X');
Output_Keithley=strsplit(out,',');
Measure_Prefix_top=cell2mat(Output_Keithley(3));
i_jun=str2double(Measure_Prefix_top(6:end));
OffsetCurrent=[OffsetCurrent;toc(),V_pol,i_pol,i_jun];
plot(V_pol,i_pol,'-k.');
for i=1:5
V_pol=V_pol-passi;
fprintf(Keithley237_BOTTOM,['B',num2str(V_pol),',0,0X']);
pause(5);
```

```
end
elseif (abs(V_pol)>99.9 && abs(V_pol)<=399)
passi=1; % cambio i passi
fprintf(Keithley237_BOTTOM,['B',num2str(V_pol),',0,0X']);

 %inserisce il nuovo valore di vpol dopo ogni ciclo
pause(60);

out=query(Keithley237_BOTTOM,'X');
out=query(Keithley237_BOTTOM,'X');
Output_Keithley=strsplit(out,','); %separa i valori tra le virgole in celle
Measure_Prefix_bottom=cell2mat(Output_Keithley(3));

%converte il valore della cella in una singola matrice
i_pol=str2double(Measure_Prefix_bottom(6:end));

 % escludo le lettere iniziali e converto in double


out=query(Keithley237_TOP,'X');
Output_Keithley=strsplit(out,',');
Measure_Prefix_top=cell2mat(Output_Keithley(3));
i_jun=str2double(Measure_Prefix_top(6:end));
OffsetCurrent=[OffsetCurrent;toc(),V_pol,i_pol,i_jun];

plot(V_pol,i_pol,'k.');
V_pol=V_pol-passi;
for i=1:10
V_pol=V_pol-passi;
fprintf(Keithley237_BOTTOM,['B',num2str(V_pol),',0,0X']);
pause(5);
end
elseif(abs(V_pol)>399) && (abs(V_pol)<=999)
passi=1; % cambio i passi
fprintf(Keithley237_BOTTOM,['B',num2str(V_pol),',0,0X']);

 %inserisce il nuovo valore di vpol dopo ogni ciclo
pause(60);
out=query(Keithley237_BOTTOM,'X');
out=query(Keithley237_BOTTOM,'X');
Output_Keithley=strsplit(out,',');
%separa i valori tra le virgole in celle
```

```
Measure_Prefix_bottom=cell2mat(Output_Keithley(3));
%converte il valore della cella in una singola matrice
i_pol=str2double(Measure_Prefix_bottom(6:end));
 % escludo le lettere iniziali e converto in double

out=query(Keithley237_TOP,'X');
Output_Keithley=strsplit(out,',');
Measure_Prefix_top=cell2mat(Output_Keithley(3));
i_jun=str2double(Measure_Prefix_top(6:end));
OffsetCurrent=[OffsetCurrent;toc(),V_pol,i_pol,i_jun];

plot(V_pol,i_pol,'-k.');
V_pol=V_pol-passi;
for i=1:50
V_pol=V_pol-passi;
fprintf(Keithley237_BOTTOM,['B',num2str(V_pol),',0,0X']);
pause(5);
end
end
else
break;
end
end
%   b1=string(clock);
%   b=char(b1); %piuttostro che str2mat
%   c=['datiIV_@',b(:,:,3),'.',b(:,:,2),'.',b(:,:,1),'_',b(:,:,4),'.',
b(:,:,5),'_',filename];

b=string(clock);

c=[filename,'@datiIV_botpol_topread_@',char(b(1,3)),'.',char(b(1,2)),
'.',char(b(1,1)),'_',char(b(1,4)),'.',char(b(1,5))];
writematrix(OffsetCurrent,(strcat(c,'.xlsx')))
save(strcat(c,'.mat'));


% oppure-----------------------------------------------
%  b=string(clock);
%   c=strcat('DatiIV_',strjoin([b(3),b(2),b(1),b(4),b(5)],{'_','_','_','_'}),
 filename);
%  writematrix(OffsetCurrent,(strcat(c,'.xlsx')))
%    save(strcat(c,'.mat'));
```

```
while(V_pol<0)
pause(10);
V_pol=V_pol+20;

if V_pol>0
V_pol=0;
end
fprintf(Keithley237_BOTTOM,['B',num2str(V_pol),',0,0X']);
end

if V_pol>0
V_pol=0;
end
fprintf(Keithley237_BOTTOM,['B',num2str(V_pol),',0,0X']);



clrdevice(Keithley237_BOTTOM);
clrdevice(Keithley237_TOP);
close all;
delete(Keithley237_BOTTOM);
delete(Keithley237_TOP);
% plot(OffsetCurrent(:,1),OffsetCurrent(:,4));
% writematrix(OffsetCurrent,'Dati_IV.xlsx');
% writematrix(OffsetCurrent,('head23_0.1V_40s_[0-10]V.xlsx'))
```

B.2 Three-keitheley IVT measures

```
%implementato da Alessi/date 15/1/2021
%Vpol,Ipol 237 top
%Ijunc     237 bot     only read




clear all;
clc;
filename=input('Insert filename:','s');
date=clock;
hold off;
pause(1)
%indirizzi sistemati bott 16 top 8
```

```
Keithley237_BOTTOM = instrfind('Type', 'gpib', 'BoardIndex',
 0, 'PrimaryAddress',16, 'Tag', '');
Keithley237_TOP = instrfind('Type', 'gpib', 'BoardIndex', 0,

'PrimaryAddress',8, 'Tag', '');
Keithley2400 = instrfind('Type', 'gpib', 'BoardIndex', 0,
 'PrimaryAddress', 24, 'Tag', '');
if isempty(Keithley237_TOP)
Keithley237_TOP = gpib('NI', 0, 8);
else
fclose(Keithley237_TOP);
Keithley237_TOP = Keithley237_TOP(1);
end
if isempty(Keithley237_BOTTOM)
Keithley237_BOTTOM = gpib('NI', 0, 16);
else
fclose(Keithley237_BOTTOM);
Keithley237_BOTTOM = Keithley237_BOTTOM(1);
end
if isempty(Keithley2400)
Keithley2400 = gpib('NI', 0, 24);
else
fclose(Keithley2400);
Keithley2400 = Keithley2400(1);
end
fopen(Keithley237_TOP);
fopen(Keithley237_BOTTOM);
fopen(Keithley2400);
clrdevice(Keithley237_TOP);
clrdevice(Keithley237_BOTTOM);
clrdevice(Keithley2400);

set(Keithley237_TOP, 'Timeout', 20);
set(Keithley237_TOP, 'EOSMode', 'read&write');
set(Keithley237_BOTTOM, 'Timeout', 20);
set(Keithley237_BOTTOM, 'EOSMode', 'read&write');

fprintf(Keithley237_TOP,'F0,0O0L3e-7,0B0,0,0T0,0,0,
0P4R1N1Y0K0G15,0,0X');
fprintf(Keithley237_BOTTOM,'F0,0O0L3e-7,0B0,0,0T0,0,0,
0P4R1N1Y0K0G15,0,0X');
```

```
flushoutput(Keithley237_TOP);
flushoutput(Keithley237_BOTTOM);
fprintf(Keithley2400, ':SYSTEM:REM');
fprintf(Keithley2400, ':TRACE:CLEAR');
fprintf(Keithley2400, ':CONF:CURR');
fprintf(Keithley2400, ':SENS:CURR:RANGE:AUTO 0');
fprintf(Keithley2400, ':SENS:CURR:PROT:LEV 5e-2');%SET COMPLIANCE
fprintf(Keithley2400, ':SENS:CURR:RANG:UPP 5e-2');

%SET MEASUREMENT PRECISION < COMPLIANCE
fprintf(Keithley2400, ':SOUR:VOLT:RANG 200');%SET SOURCE PRECISION
fprintf(Keithley2400, ':DISP:DIG MAX'); %0.2 s FOR THE CURRENT TO SET
fprintf(Keithley2400, ':TRAC:TST:FORM DELT');
fprintf(Keithley2400, ':DISP:ENAB 1');
fprintf(Keithley2400, ':SOUR:VOLT 0');
flushoutput(Keithley2400);pause(5);
tic();
%  Output_Keithley=strsplit(query(Keithley237_BOTTOM,'X'),',');
Rtotemp=(40+200)/(577.7-92.6);
%-----------------------------------------------------
fprintf(Keithley2400, ':SOUR:VOLT 1');
Output_Keithley=str2num(query(Keithley2400, ':READ?'));
%-----------------------------------------------------
%R0=1/Output_Keithley(2);
%R=R0;
R0=0;
R=1/Output_Keithley(2);
t_T=["time","R","T°";toc(),R,R*Rtotemp-245.81];
while R<540
if R-R0>10
disp('Start I-V');
[i_pol,i_jun,i2400]=MeasureCurrent(Keithley237_TOP,
Keithley237_BOTTOM,Keithley2400);
V_pol=0;
OffsetCurrent=["t","Rpt","Temp°","Vpol_top","i_pol-TOP","i_jun_bot";
toc(),R,R*Rtotemp-245.81,V_pol,i_pol,i_jun];
OffsetCurrentHalf=["t","Rpt","Temp°","Vpol_top","i_pol-TOP",

"i_jun_bot";toc(),R,R*Rtotemp-245.81,V_pol,i_pol,i_jun];
OffsetCurrentQuarter=["t","Rpt","Temp°","Vpol_top",
"i_pol-TOP","i_jun_bot";toc(),R,R*Rtotemp-245.81,V_pol,i_pol,i_jun];
plot(V_pol,i_pol,'k.');
```

```
hold on;
V_pol=-0.1;
p=5;
while abs(V_pol)<=1000

%set the maximux value of vpol, doesn't matter the sign
if (abs(i_pol)<1e-5 && abs(i_jun)<1e-5
 && abs(i_pol*V_pol) <1e-3 && abs(i_jun*V_pol)<1e-3)
  %control of the maximum value of current )
fprintf(Keithley237_TOP,['B',num2str(V_pol),',0,0X']);
 %inserisce il nuovo valore di vpol dopo ogni ciclo
pause(p/4);
[i_pol,i_jun,i2400]=MeasureCurrent(Keithley237_TOP,
Keithley237_BOTTOM,Keithley2400);
OffsetCurrentQuarter=[OffsetCurrentQuarter;toc(),1/i2400,
1/i2400*Rtotemp-245.81,V_pol,i_pol,i_jun];
pause(p/4);
[i_pol,i_jun,i2400]=MeasureCurrent(Keithley237_TOP,
Keithley237_BOTTOM,Keithley2400);
OffsetCurrentHalf=[OffsetCurrentHalf;toc(),1/i2400,
1/i2400*Rtotemp-245.81,V_pol,i_pol,i_jun];
pause(p/2);
[i_pol,i_jun,i2400]=MeasureCurrent(Keithley237_TOP,
Keithley237_BOTTOM,Keithley2400);
OffsetCurrent=[OffsetCurrent;toc(),1/i2400,
1/i2400*Rtotemp-245.81,V_pol,i_pol,i_jun];
plot(V_pol,i_pol,'kd');
V_pol=V_pol*10^(1/8);
p=p*1.12;
else
break;
end
end
b=string(clock);
c=[filename,'@Head23heatingR',num2str(round(R)),'@',
char(b(1,3)),
'.',char(b(1,2)),'.',char(b(1,1)),'_',char(b(1,4)),'.',
char(b(1,5))];
writematrix(OffsetCurrent,(strcat(c,'.xlsx')),'Sheet',
'FullPause');
writematrix(OffsetCurrentHalf,(strcat(c,'.xlsx')),'Sheet',
'HalfPause');
```

```
writematrix(OffsetCurrentQuarter,(strcat(c,'.xlsx')),'Sheet',
'QuarterPause');
save(strcat(c,'.mat'));
while(V_pol<0)
pause(5);
V_pol=V_pol+50;
if V_pol>0
V_pol=0;
end
fprintf(Keithley237_TOP,['B',num2str(V_pol),',0,0X']);
end
fprintf(Keithley237_TOP,['B0,0,0X']);
disp('Stop I-V');
R0=R;
end
pause(1);
Output_Keithley=str2num(query(Keithley2400, ':READ?'));
R=1/Output_Keithley(2);
t_T=[t_T;toc(),R,R*Rtotemp-245.81];
end
writematrix(t_T,'time_temp.xlsx');
clrdevice(Keithley237_BOTTOM);
clrdevice(Keithley237_TOP);
close all;
delete(Keithley237_BOTTOM);
delete(Keithley237_TOP);
% plot(OffsetCurrent(:,1),OffsetCurrent(:,4));
% writematrix(OffsetCurrent,'Dati_IV.xlsx');


function  [I_TOP, I_BOTTOM,I_2400]=MeasureCurrent(INSTR1,INSTR2,INSTR3)
out=query(INSTR1,'X');
Output_Keithley=strsplit(out,',');
Measure_Prefix_top=cell2mat(Output_Keithley(3));
I_TOP=str2double(Measure_Prefix_top(6:end));
out=query(INSTR2,'X');
Output_Keithley=strsplit(out,',');
Measure_Prefix_bottom=cell2mat(Output_Keithley(3));
I_BOTTOM=str2double(Measure_Prefix_bottom(6:end));
Output_Keithley=str2num(query(INSTR3, ':READ?'));
I_2400=Output_Keithley(2);
end
```

Whole bibliography

[] *"Ortec," [Online].* URL: http://www.ortec-online.com.

[AL00] M Amman and P.N Luke. "Three-dimensional position sensing and field shaping in orthogonal-strip germanium gamma-ray detectors". In: *Nuclear Instruments and Methods in Physics Research Section A: Accelerators, Spectrometers, Detectors and Associated Equipment* 452.1-2 (Sept. 2000), pp. 155–166. DOI: 10.1016/s0168-9002(00)00351-x. URL: https://doi.org/10.1016/s0168-9002(00)00351-x.

[ALB07] M. Amman, P.N. Luke, and S.E. Boggs. "Amorphous-semiconductor-contact germanium-based detectors for gamma-ray imaging and spectroscopy". In: *Nuclear Instruments and Methods in Physics Research Section A: Accelerators, Spectrometers, Detectors and Associated Equipment* 579.2 (Sept. 2007), pp. 886–890. DOI: 10.1016/j.nima.2007.05.307. URL: https://doi.org/10.1016/j.nima.2007.05.307.

[Ame+84] S.R. Amendolia et al. "Germanium microstrip detectors with 50 and 100 μm pitch". In: *Nuclear Instruments and Methods in Physics Research Section A: Accelerators, Spectrometers, Detectors and Associated Equipment* 226.1 (Sept. 1984), pp. 117–121. DOI: 10.1016/0168-9002(84)90178-5. URL: https://doi.org/10.1016/0168-9002(84)90178-5.

[Att86] Frank Herbert Attix. *Introduction to Radiological Physics Radiation Dosimetry*. 1st ed. Wiley-VCH, 1986. ISBN: 0471011460,9780471011460,9783527617142.

[Bae+79] P. Baeri et al. "A melting model for pulsing-laser annealing of implanted semiconductors". In: *Journal of Applied Physics* 50.2 (Feb. 1979), pp. 788–797. DOI: 10.1063/1.326046. URL: https://doi.org/10.1063/1.326046.

[Bar+19] Zhaslan Baraissov et al. "Selective Wet Etching of Silicon Germanium in Composite Vertical Nanowires". In: *ACS Applied Materials & Interfaces* 11.40 (Sept. 2019), pp. 36839–36846. DOI: 10.1021/acsami.9b11934. URL: https://doi.org/10.1021/acsami.9b11934.

[BB08] Sergej Brotzmann and Hartmut Bracht. "Intrinsic and extrinsic diffusion of phosphorus, arsenic, and antimony in germanium". In: *Journal of Applied Physics* 103.3 (Feb. 2008), p. 033508. DOI: 10.1063/1.2837103. URL: https://doi.org/10.1063/1.2837103.

[Ber+21] S. Bertoldo et al. "New method for the production of thin and stable, segmented n+ contacts in HPGe detectors". In: *The European Physical Journal A* 57.6 (June 2021). DOI: 10.1140/epja/s10050-021-00487-8. URL: https://doi.org/10.1140/epja/s10050-021-00487-8.

[BH70] R. D. Baertsch and R. N. Hall. "Gamma Ray Detectors Made from High Purity Germanium". In: *IEEE Transactions on Nuclear Science* 17.3 (1970), pp. 235–240. DOI: 10.1109/tns.1970.4325695. URL: https://doi.org/10.1109/tns.1970.4325695.

[Bol+18] V Boldrini et al. "Characterization and modeling of thermally-induced doping contaminants in high-purity germanium". In: *Journal of Physics D: Applied Physics* 52.3 (Nov. 2018), p. 035104. DOI: 10.1088/1361-6463/aae9c0. URL: https://doi.org/10.1088/1361-6463/aae9c0.

[Bru+10] E. Bruno et al. "High-level incorporation of antimony in germanium by laser annealing". In: *Journal of Applied Physics* 108.12 (Dec. 2010), p. 124902. DOI: 10.1063/1.3520671. URL: https://doi.org/10.1063/1.3520671.

[Bru+12] E. Bruno et al. "Anomalous transport of Sb in laser irradiated Ge". In: *Applied Physics Letters* 101.17 (Oct. 2012), p. 172110. DOI: 10.1063/1.4764069. URL: https://doi.org/10.1063/1.4764069.

[BV62] J. Bloem and J. C. van Vessem. "Etching Ge with Mixtures of HF-H[sub 2]O[sub 2]-H[sub 2]O". In: *Journal of The Electrochemical Society* 109.1 (1962), p. 33. DOI: 10.1149/1.2425321. URL: https://doi.org/10.1149/1.2425321.

[Car+20] Chiara Carraro et al. "N-type heavy doping with ultralow resistivity in Ge by Sb deposition and pulsed laser melting". In: *Applied Surface Science* 509 (Apr. 2020), p. 145229. DOI: 10.1016/j.apsusc.2019.145229. URL: https://doi.org/10.1016/j.apsusc.2019.145229.

[Col] Colautti. "Sviluppo di una Membrana Submicrometrica di Germanio per Esperimenti di Channeling".

[Coo+07] R.J. Cooper et al. "Position sensitivity of the first SmartPET HPGe detector". In: *Nuclear Instruments and Methods in Physics Research Section A: Accelerators, Spectrometers, Detectors and Associated Equipment* 573.1-2 (Apr. 2007), pp. 72–75. DOI: 10.1016/j.nima.2006.11.035. URL: https://doi.org/10.1016/j.nima.2006.11.035.

[Det76] J. F. Detko. "Progress toward a Stable Orthogonal Strip Germanium Gamma Camera". In: *IEEE Transactions on Nuclear Science* 23.1 (1976), pp. 538–542. DOI: 10.1109/tns.1976.4328301. URL: https://doi.org/10.1109/tns.1976.4328301.

[Duf+10] R. Duffy et al. "Quantitative prediction of junction leakage in bulk-technology CMOS devices". In: *Solid-State Electronics* 54.3 (Mar. 2010), pp. 243–251. DOI: 10.1016/j.sse.2009.09.007. URL: https://doi.org/10.1016/j.sse.2009.09.007.

[Eds82] J. Poate (Eds.) *Laser Annealing of Semiconductors*. Academic Press, 1982. ISBN: 978-0-12-558820-1,0-12-558820-8.

[Fan63] U Fano. "Penetration of Protons, Alpha Particles, and Mesons". In: *Annual Review of Nuclear Science* 13.1 (Dec. 1963), pp. 1–66. DOI: 10.1146/annurev.ns.13.120163.000245. URL: https://doi.org/10.1146/annurev.ns.13.120163.000245.

[Gho13] Walid Ghoggali. "Optimization of the performance of a pixellated germanium Compton camera". PhD thesis. University College London, 2013.

[Gut90] D. Gutknecht. "Photomask technique for fabricating high purity germanium strip detectors". In: *Nuclear Instruments and Methods in Physics Research Section A: Accelerators, Spectrometers, Detectors and Associated Equipment* 288.1 (Mar. 1990), pp. 13–18. DOI: 10.1016/0168-9002(90)90456-g. URL: https://doi.org/10.1016/0168-9002(90)90456-g.

[Hal06] E.E. Haller. "Germanium: From its discovery to SiGe devices". In: *Materials Science in Semiconductor Processing* 9.4-5 (Aug. 2006), pp. 408–422. DOI: 10.1016/j.mssp.2006.08.063. URL: https://doi.org/10.1016/j.mssp.2006.08.063.

[Har+12] LJ Harkness et al. "Semiconductor detectors for Compton imaging in nuclear medicine". In: *Journal of Instrumentation* 7.01 (Jan. 2012), pp. C01004–C01004. DOI: 10.1088/1748-0221/7/01/c01004. URL: https://doi.org/10.1088/1748-0221/7/01/c01004.

[He01] Zhong He. "Review of the Shockley-Ramo theorem and its application in semiconductor gamma-ray detectors". In: *Nuclear Instruments and Methods in Physics Research Section A: Accelerators, Spectrometers, Detectors and Associated Equipment* 463.1-2 (May 2001), pp. 250–267. DOI: 10.1016/s0168-9002(01)00223-6. URL: https://doi.org/10.1016/s0168-9002(01)00223-6.

[Hea+07] J. Headspith et al. “First experimental data from XH, a fine pitch germanium microstrip detector for energy dispersive EXAFS (EDE)”. In: *2007 IEEE Nuclear Science Symposium Conference Record*. IEEE, 2007. DOI: 10.1109/nssmic.2007.4436647. URL: https://doi.org/10.1109/nssmic.2007.4436647.

[HH82] W. L. Hansen and E.E. Haller. “High-Purity Germanium Crystal Growing”. In: *MRS Proceedings* 16 (1982). DOI: 10.1557/proc-16-1. URL: https://doi.org/10.1557/proc-16-1.

[Hue+16] Fernando Hueso-González et al. “Compton Camera and Prompt Gamma Ray Timing: Two Methods for In Vivo Range Assessment in Proton Therapy”. In: *Frontiers in Oncology* 6 (Apr. 2016). DOI: 10.3389/fonc.2016.00080. URL: https://doi.org/10.3389/fonc.2016.00080.

[Hyd+19] Jennifer M. Hydrick et al. “Chemical Mechanical Polishing of Epitaxial Germanium on SiO2-patterned Si(001) Substrates”. In: *ECS Transactions* 16.10 (Dec. 2019), pp. 237–248. DOI: 10.1149/1.2986777. URL: https://doi.org/10.1149/1.2986777.

[Imp+13] G. Impellizzeri et al. “B-doping in Ge by excimer laser annealing”. In: *Journal of Applied Physics* 113.11 (Mar. 2013), p. 113505. DOI: 10.1063/1.4795268. URL: https://doi.org/10.1063/1.4795268.

[Ins01] Keithley Instruments. “236/237/238 Manual Package”. In: (2001). URL: https://download.tek.com/manual/236_900_01E.pdf.

[Ish+10] Shin-nosuke Ishikawa et al. “Development of Double-Sided CdTe Strip Detectors for gamma-Ray Imaging and Spectroscopy”. In: *Japanese Journal of Applied Physics* 49.11 (Nov. 2010), p. 116702. DOI: 10.1143/jjap.49.116702. URL: https://doi.org/10.1143/jjap.49.116702.

[Kal+16] T. Kalliovaara et al. “Electrical compensation via vacancy–donor complexes in arsenic-implanted and laser-annealed germanium”. In: *Applied Physics Letters* 109.18 (Oct. 2016), p. 182107. DOI: 10.1063/1.4966947. URL: https://doi.org/10.1063/1.4966947.

[Kno10] Glenn F. Knoll. *Radiation Detection and Measurement*. 4th. Wiley, 2010. ISBN: 9780470131480.

[Kra87] Kenneth S. Krane. *Introductory Nuclear Physics*. 1st ed. Wiley, 1987. ISBN: 9780471805533,047180553X.

[Kri+15] J. Krimmer et al. “Development of a Compton camera for medical applications based on silicon strip and scintillation detectors”. In: *Nuclear Instruments and Methods in Physics Research Section A: Accelerators, Spectrometers, Detectors and Associated Equipment* 787 (July 2015), pp. 98–101. DOI: 10.1016/j.nima.2014.11.042. URL: https://doi.org/10.1016/j.nima.2014.11.042.

[Lai+09] A. Laikhtman et al. “Contamination Produced by Vacuum Outgassing of Kapton Acrylic Adhesive Tape”. In: *Journal of Spacecraft and Rockets* 46.2 (Mar. 2009), pp. 236–240. DOI: 10.2514/1.31868. URL: https://doi.org/10.2514/1.31868.

[Lin16] Maximilian Linser. “Germanium Doping by Aluminium Ion Implantation and Laser Thermal Annealing”. PhD thesis. 2016.

[Lla72] J. Llacer. “Planar and coaxial high purity germanium radiation detectors”. In: *Nuclear Instruments and Methods* 98.2 (Jan. 1972), pp. 259–268. DOI: 10.1016/0029-554x(72)90106-1. URL: https://doi.org/10.1016/0029-554x(72)90106-1.

[LPD94] P.N. Luke, R.H. Pehl, and F.A. Dilmanian. “A 140-element Ge detector fabricated with amorphous Ge blocking contacts”. In: *IEEE Transactions on Nuclear Science* 41.4 (Aug. 1994), pp. 976–978. DOI: 10.1109/23.322842. URL: https://doi.org/10.1109/23.322842.

[Mag+15] G. Maggioni et al. “Characterization of different surface passivation routes applied to a planar HPGe detector”. In: *The European Physical Journal A* 51.11 (Nov. 2015). DOI: 10.1140/epja/i2015-15141-9. URL: https://doi.org/10.1140/epja/i2015-15141-9.

[Mag+18] G. Maggioni et al. “Pulsed laser diffusion of thin hole-barrier contacts in high purity germanium for gamma radiation detectors”. In: *The European Physical Journal A* 54.3 (Mar. 2018). DOI: 10.1140/epja/i2018-12471-0. URL: https://doi.org/10.1140/epja/i2018-12471-0.

[Mih+07] L. Mihailescu et al. “SPEIR: A Ge Compton camera”. In: *Nuclear Instruments and Methods in Physics Research Section A: Accelerators, Spectrometers, Detectors and Associated Equipment* 570.1 (Jan. 2007), pp. 89–100. DOI: 10.1016/j.nima.2006.09.111. URL: https://doi.org/10.1016/j.nima.2006.09.111.

[Mil+14] R. Milazzo et al. “N-type doping of Ge by As implantation and excimer laser annealing”. In: *Journal of Applied Physics* 115.5 (Feb. 2014), p. 053501. DOI: 10.1063/1.4863779. URL: https://doi.org/10.1063/1.4863779.

[Nea02] Donald Neamen. *Semiconductor Physics And Devices*. 3rd ed. McGraw-Hill Science/Engineering/Math, 2002. ISBN: 9780072321074,0072321075.

[Ped+11] Shivaji Peddeti et al. “Chemical Mechanical Polishing of Ge Using Colloidal Silica Particles and H2O2”. In: *Electrochemical and Solid-State Letters* 14.7 (2011), H254. DOI: 10.1149/1.3575166. URL: https://doi.org/10.1149/1.3575166.

[Pel60] E. M. Pell. "Ion Drift in an n-p Junction". In: *Journal of Applied Physics* 31.2 (Feb. 1960), pp. 291–302. DOI: 10.1063/1.1735561. URL: https://doi.org/10.1063/1.1735561.

[Pit+04] Arthur J. Pitera et al. "Coplanar Integration of Lattice-Mismatched Semiconductors with Silicon by Wafer Bonding Ge/Si[sub 1-x]Ge[sub x]/Si Virtual Substrates". In: *Journal of The Electrochemical Society* 151.7 (2004), G443. DOI: 10.1149/1.1757462. URL: https://doi.org/10.1149/1.1757462.

[PR77] D. Protic and G. Riepe. "High-Resolution Charged-Particle Spectroscopy with High-Purity Germanium Detectors in the Intermediate Energy Range". In: *IEEE Transactions on Nuclear Science* 24.1 (Feb. 1977), pp. 64–67. DOI: 10.1109/tns.1977.4328644. URL: https://doi.org/10.1109/tns.1977.4328644.

[Sch67] B. Schwartz. "Chemical Etching of Germanium in the System HF-H[sub 2]O[sub 2]-H[sub 2]O". In: *Journal of The Electrochemical Society* 114.3 (1967), p. 285. DOI: 10.1149/1.2426568. URL: https://doi.org/10.1149/1.2426568.

[SG66] S.M. Sze and G. Gibbons. "Effect of junction curvature on breakdown voltage in semiconductors". In: *Solid-State Electronics* 9.9 (Sept. 1966), pp. 831–845. DOI: 10.1016/0038-1101(66)90033-5. URL: https://doi.org/10.1016/0038-1101(66)90033-5.

[SHS73] V. Schönfelder, A. Hirner, and K. Schneider. "A telescope for soft gamma ray astronomy". In: *Nuclear Instruments and Methods* 107.2 (Mar. 1973), pp. 385–394. DOI: 10.1016/0029-554x(73)90257-7. URL: https://doi.org/10.1016/0029-554x(73)90257-7.

[Sze81a] S.M. Sze. *Physics of Semiconductor Devices*. 2nd. John Wiley and Sons (WIE), 1981. ISBN: 047109837X,9780471098379.

[Sze81b] S.M. Sze. *Physics of Semiconductor Devices*. 2nd. John Wiley and Sons (WIE), 1981. ISBN: 047109837X,9780471098379.

[Tav64] A. J. Tavendale. "Semiconductor Lithium-Ion Drift Diodes as High-Resolution Gamma-Ray Pair Spectrometers". In: *IEEE Transactions on Nuclear Science* 11.3 (1964), pp. 191–200. DOI: 10.1109/tns.1964.4323422. URL: https://doi.org/10.1109/tns.1964.4323422.

[TNE74] R. W. TODD, J. M. NIGHTINGALE, and D. B. EVERETT. "A proposed gamma camera". In: *Nature* 251.5471 (Sept. 1974), pp. 132–134. DOI: 10.1038/251132a0. URL: https://doi.org/10.1038/251132a0.

[VBM04] K Vetter, M Burks, and L Mihailescu. "Gamma-ray imaging with position-sensitive HPGe detectors". In: *Nuclear Instruments and Methods in Physics Research Section A: Accelerators, Spectrometers, Detectors and Associated Equipment* 525.1-2 (June 2004), pp. 322–327. DOI: 10.1016/j.nima.2004.03.087. URL: https://doi.org/10.1016/j.nima.2004.03.087.

[Vet+18] Kai Vetter et al. "Gamma-Ray imaging for nuclear security and safety: Towards 3-D gamma-ray vision". In: *Nuclear Instruments and Methods in Physics Research Section A: Accelerators, Spectrometers, Detectors and Associated Equipment* 878 (Jan. 2018), pp. 159–168. DOI: 10.1016/j.nima.2017.08.040. URL: https://doi.org/10.1016/j.nima.2017.08.040.

Articles only

[AL00] M Amman and P.N Luke. "Three-dimensional position sensing and field shaping in orthogonal-strip germanium gamma-ray detectors". In: *Nuclear Instruments and Methods in Physics Research Section A: Accelerators, Spectrometers, Detectors and Associated Equipment* 452.1-2 (Sept. 2000), pp. 155–166. DOI: 10.1016/s0168-9002(00)00351-x. URL: https://doi.org/10.1016/s0168-9002(00)00351-x.

[ALB07] M. Amman, P.N. Luke, and S.E. Boggs. "Amorphous-semiconductor-contact germanium-based detectors for gamma-ray imaging and spectroscopy". In: *Nuclear Instruments and Methods in Physics Research Section A: Accelerators, Spectrometers, Detectors and Associated Equipment* 579.2 (Sept. 2007), pp. 886–890. DOI: 10.1016/j.nima.2007.05.307. URL: https://doi.org/10.1016/j.nima.2007.05.307.

[Ame+84] S.R. Amendolia et al. "Germanium microstrip detectors with 50 and 100 μm pitch". In: *Nuclear Instruments and Methods in Physics Research Section A: Accelerators, Spectrometers, Detectors and Associated Equipment* 226.1 (Sept. 1984), pp. 117–121. DOI: 10.1016/0168-9002(84)90178-5. URL: https://doi.org/10.1016/0168-9002(84)90178-5.

[Bae+79] P. Baeri et al. "A melting model for pulsing-laser annealing of implanted semiconductors". In: *Journal of Applied Physics* 50.2 (Feb. 1979), pp. 788–797. DOI: 10.1063/1.326046. URL: https://doi.org/10.1063/1.326046.

[Bar+19] Zhaslan Baraissov et al. "Selective Wet Etching of Silicon Germanium in Composite Vertical Nanowires". In: *ACS Applied Materials & Interfaces* 11.40 (Sept. 2019), pp. 36839–36846. DOI: 10.1021/acsami.9b11934. URL: https://doi.org/10.1021/acsami.9b11934.

[BB08] Sergej Brotzmann and Hartmut Bracht. "Intrinsic and extrinsic diffusion of phosphorus, arsenic, and antimony in germanium". In: *Journal of Applied Physics* 103.3 (Feb. 2008), p. 033508. DOI: 10.1063/1.2837103. URL: https://doi.org/10.1063/1.2837103.

[Ber+21] S. Bertoldo et al. "New method for the production of thin and stable, segmented n+ contacts in HPGe detectors". In: *The European Physical Journal A* 57.6 (June 2021). DOI: 10.1140/epja/s10050-021-00487-8. URL: https://doi.org/10.1140/epja/s10050-021-00487-8.

[BH70] R. D. Baertsch and R. N. Hall. "Gamma Ray Detectors Made from High Purity Germanium". In: *IEEE Transactions on Nuclear Science* 17.3 (1970), pp. 235–240. DOI: 10.1109/tns.1970.4325695. URL: https://doi.org/10.1109/tns.1970.4325695.

[Bol+18] V Boldrini et al. “Characterization and modeling of thermally-induced doping contaminants in high-purity germanium”. In: *Journal of Physics D: Applied Physics* 52.3 (Nov. 2018), p. 035104. DOI: 10.1088/1361-6463/aae9c0. URL: https://doi.org/10.1088/1361-6463/aae9c0.

[Bru+10] E. Bruno et al. “High-level incorporation of antimony in germanium by laser annealing”. In: *Journal of Applied Physics* 108.12 (Dec. 2010), p. 124902. DOI: 10.1063/1.3520671. URL: https://doi.org/10.1063/1.3520671.

[Bru+12] E. Bruno et al. “Anomalous transport of Sb in laser irradiated Ge”. In: *Applied Physics Letters* 101.17 (Oct. 2012), p. 172110. DOI: 10.1063/1.4764069. URL: https://doi.org/10.1063/1.4764069.

[BV62] J. Bloem and J. C. van Vessem. “Etching Ge with Mixtures of HF-H[sub 2]O[sub 2]-H[sub 2]O”. In: *Journal of The Electrochemical Society* 109.1 (1962), p. 33. DOI: 10.1149/1.2425321. URL: https://doi.org/10.1149/1.2425321.

[Car+20] Chiara Carraro et al. “N-type heavy doping with ultralow resistivity in Ge by Sb deposition and pulsed laser melting”. In: *Applied Surface Science* 509 (Apr. 2020), p. 145229. DOI: 10.1016/j.apsusc.2019.145229. URL: https://doi.org/10.1016/j.apsusc.2019.145229.

[Coo+07] R.J. Cooper et al. “Position sensitivity of the first SmartPET HPGe detector”. In: *Nuclear Instruments and Methods in Physics Research Section A: Accelerators, Spectrometers, Detectors and Associated Equipment* 573.1-2 (Apr. 2007), pp. 72–75. DOI: 10.1016/j.nima.2006.11.035. URL: https://doi.org/10.1016/j.nima.2006.11.035.

[Det76] J. F. Detko. “Progress toward a Stable Orthogonal Strip Germanium Gamma Camera”. In: *IEEE Transactions on Nuclear Science* 23.1 (1976), pp. 538–542. DOI: 10.1109/tns.1976.4328301. URL: https://doi.org/10.1109/tns.1976.4328301.

[Duf+10] R. Duffy et al. “Quantitative prediction of junction leakage in bulk-technology CMOS devices”. In: *Solid-State Electronics* 54.3 (Mar. 2010), pp. 243–251. DOI: 10.1016/j.sse.2009.09.007. URL: https://doi.org/10.1016/j.sse.2009.09.007.

[Fan63] U Fano. “Penetration of Protons, Alpha Particles, and Mesons”. In: *Annual Review of Nuclear Science* 13.1 (Dec. 1963), pp. 1–66. DOI: 10.1146/annurev.ns.13.120163.000245. URL: https://doi.org/10.1146/annurev.ns.13.120163.000245.

[Gut90] D. Gutknecht. "Photomask technique for fabricating high purity germanium strip detectors". In: *Nuclear Instruments and Methods in Physics Research Section A: Accelerators, Spectrometers, Detectors and Associated Equipment* 288.1 (Mar. 1990), pp. 13–18. DOI: 10.1016/0168-9002(90)90456-g. URL: https://doi.org/10.1016/0168-9002(90)90456-g.

[Hal06] E.E. Haller. "Germanium: From its discovery to SiGe devices". In: *Materials Science in Semiconductor Processing* 9.4-5 (Aug. 2006), pp. 408–422. DOI: 10.1016/j.mssp.2006.08.063. URL: https://doi.org/10.1016/j.mssp.2006.08.063.

[Har+12] LJ Harkness et al. "Semiconductor detectors for Compton imaging in nuclear medicine". In: *Journal of Instrumentation* 7.01 (Jan. 2012), pp. C01004–C01004. DOI: 10.1088/1748-0221/7/01/c01004. URL: https://doi.org/10.1088/1748-0221/7/01/c01004.

[He01] Zhong He. "Review of the Shockley-Ramo theorem and its application in semiconductor gamma-ray detectors". In: *Nuclear Instruments and Methods in Physics Research Section A: Accelerators, Spectrometers, Detectors and Associated Equipment* 463.1-2 (May 2001), pp. 250–267. DOI: 10.1016/s0168-9002(01)00223-6. URL: https://doi.org/10.1016/s0168-9002(01)00223-6.

[HH82] W. L. Hansen and E.E. Haller. "High-Purity Germanium Crystal Growing". In: *MRS Proceedings* 16 (1982). DOI: 10.1557/proc-16-1. URL: https://doi.org/10.1557/proc-16-1.

[Hue+16] Fernando Hueso-González et al. "Compton Camera and Prompt Gamma Ray Timing: Two Methods for In Vivo Range Assessment in Proton Therapy". In: *Frontiers in Oncology* 6 (Apr. 2016). DOI: 10.3389/fonc.2016.00080. URL: https://doi.org/10.3389/fonc.2016.00080.

[Hyd+19] Jennifer M. Hydrick et al. "Chemical Mechanical Polishing of Epitaxial Germanium on SiO2-patterned Si(001) Substrates". In: *ECS Transactions* 16.10 (Dec. 2019), pp. 237–248. DOI: 10.1149/1.2986777. URL: https://doi.org/10.1149/1.2986777.

[Imp+13] G. Impellizzeri et al. "B-doping in Ge by excimer laser annealing". In: *Journal of Applied Physics* 113.11 (Mar. 2013), p. 113505. DOI: 10.1063/1.4795268. URL: https://doi.org/10.1063/1.4795268.

[Ins01] Keithley Instruments. "236/237/238 Manual Package". In: (2001). URL: https://download.tek.com/manual/236_900_01E.pdf.

[Ish+10] Shin-nosuke Ishikawa et al. "Development of Double-Sided CdTe Strip Detectors for gamma-Ray Imaging and Spectroscopy". In: *Japanese Journal of Applied Physics* 49.11 (Nov. 2010), p. 116702. DOI: 10.1143/jjap.49.116702. URL: https://doi.org/10.1143/jjap.49.116702.

[Kal+16] T. Kalliovaara et al. “Electrical compensation via vacancy–donor complexes in arsenic-implanted and laser-annealed germanium”. In: *Applied Physics Letters* 109.18 (Oct. 2016), p. 182107. DOI: 10.1063/1.4966947. URL: https://doi.org/10.1063/1.4966947.

[Kri+15] J. Krimmer et al. “Development of a Compton camera for medical applications based on silicon strip and scintillation detectors”. In: *Nuclear Instruments and Methods in Physics Research Section A: Accelerators, Spectrometers, Detectors and Associated Equipment* 787 (July 2015), pp. 98–101. DOI: 10.1016/j.nima.2014.11.042. URL: https://doi.org/10.1016/j.nima.2014.11.042.

[Lai+09] A. Laikhtman et al. “Contamination Produced by Vacuum Outgassing of Kapton Acrylic Adhesive Tape”. In: *Journal of Spacecraft and Rockets* 46.2 (Mar. 2009), pp. 236–240. DOI: 10.2514/1.31868. URL: https://doi.org/10.2514/1.31868.

[Lla72] J. Llacer. “Planar and coaxial high purity germanium radiation detectors”. In: *Nuclear Instruments and Methods* 98.2 (Jan. 1972), pp. 259–268. DOI: 10.1016/0029-554x(72)90106-1. URL: https://doi.org/10.1016/0029-554x(72)90106-1.

[LPD94] P.N. Luke, R.H. Pehl, and F.A. Dilmanian. “A 140-element Ge detector fabricated with amorphous Ge blocking contacts”. In: *IEEE Transactions on Nuclear Science* 41.4 (Aug. 1994), pp. 976–978. DOI: 10.1109/23.322842. URL: https://doi.org/10.1109/23.322842.

[Mag+15] G. Maggioni et al. “Characterization of different surface passivation routes applied to a planar HPGe detector”. In: *The European Physical Journal A* 51.11 (Nov. 2015). DOI: 10.1140/epja/i2015-15141-9. URL: https://doi.org/10.1140/epja/i2015-15141-9.

[Mag+18] G. Maggioni et al. “Pulsed laser diffusion of thin hole-barrier contacts in high purity germanium for gamma radiation detectors”. In: *The European Physical Journal A* 54.3 (Mar. 2018). DOI: 10.1140/epja/i2018-12471-0. URL: https://doi.org/10.1140/epja/i2018-12471-0.

[Mih+07] L. Mihailescu et al. “SPEIR: A Ge Compton camera”. In: *Nuclear Instruments and Methods in Physics Research Section A: Accelerators, Spectrometers, Detectors and Associated Equipment* 570.1 (Jan. 2007), pp. 89–100. DOI: 10.1016/j.nima.2006.09.111. URL: https://doi.org/10.1016/j.nima.2006.09.111.

[Mil+14] R. Milazzo et al. “N-type doping of Ge by As implantation and excimer laser annealing”. In: *Journal of Applied Physics* 115.5 (Feb. 2014), p. 053501. DOI: 10.1063/1.4863779. URL: https://doi.org/10.1063/1.4863779.

[Ped+11] Shivaji Peddeti et al. “Chemical Mechanical Polishing of Ge Using Colloidal Silica Particles and H2O2”. In: *Electrochemical and Solid-State Letters* 14.7 (2011), H254. DOI: 10.1149/1.3575166. URL: https://doi.org/10.1149/1.3575166.

[Pel60] E. M. Pell. “Ion Drift in an n-p Junction”. In: *Journal of Applied Physics* 31.2 (Feb. 1960), pp. 291–302. DOI: 10.1063/1.1735561. URL: https://doi.org/10.1063/1.1735561.

[Pit+04] Arthur J. Pitera et al. “Coplanar Integration of Lattice-Mismatched Semiconductors with Silicon by Wafer Bonding Ge/Si[sub 1-x]Ge[sub x]/Si Virtual Substrates”. In: *Journal of The Electrochemical Society* 151.7 (2004), G443. DOI: 10.1149/1.1757462. URL: https://doi.org/10.1149/1.1757462.

[PR77] D. Protic and G. Riepe. “High-Resolution Charged-Particle Spectroscopy with High-Purity Germanium Detectors in the Intermediate Energy Range”. In: *IEEE Transactions on Nuclear Science* 24.1 (Feb. 1977), pp. 64–67. DOI: 10.1109/tns.1977.4328644. URL: https://doi.org/10.1109/tns.1977.4328644.

[Sch67] B. Schwartz. “Chemical Etching of Germanium in the System HF-H[sub 2]O[sub 2]-H[sub 2]O”. In: *Journal of The Electrochemical Society* 114.3 (1967), p. 285. DOI: 10.1149/1.2426568. URL: https://doi.org/10.1149/1.2426568.

[SG66] S.M. Sze and G. Gibbons. “Effect of junction curvature on breakdown voltage in semiconductors”. In: *Solid-State Electronics* 9.9 (Sept. 1966), pp. 831–845. DOI: 10.1016/0038-1101(66)90033-5. URL: https://doi.org/10.1016/0038-1101(66)90033-5.

[SHS73] V. Schönfelder, A. Hirner, and K. Schneider. “A telescope for soft gamma ray astronomy”. In: *Nuclear Instruments and Methods* 107.2 (Mar. 1973), pp. 385–394. DOI: 10.1016/0029-554x(73)90257-7. URL: https://doi.org/10.1016/0029-554x(73)90257-7.

[Tav64] A. J. Tavendale. “Semiconductor Lithium-Ion Drift Diodes as High-Resolution Gamma-Ray Pair Spectrometers”. In: *IEEE Transactions on Nuclear Science* 11.3 (1964), pp. 191–200. DOI: 10.1109/tns.1964.4323422. URL: https://doi.org/10.1109/tns.1964.4323422.

[TNE74] R. W. TODD, J. M. NIGHTINGALE, and D. B. EVERETT. “A proposed gamma camera”. In: *Nature* 251.5471 (Sept. 1974), pp. 132–134. DOI: 10.1038/251132a0. URL: https://doi.org/10.1038/251132a0.

[VBM04] K Vetter, M Burks, and L Mihailescu. "Gamma-ray imaging with position-sensitive HPGe detectors". In: *Nuclear Instruments and Methods in Physics Research Section A: Accelerators, Spectrometers, Detectors and Associated Equipment* 525.1-2 (June 2004), pp. 322–327. DOI: 10.1016/j.nima.2004.03.087. URL: https://doi.org/10.1016/j.nima.2004.03.087.

[Vet+18] Kai Vetter et al. "Gamma-Ray imaging for nuclear security and safety: Towards 3-D gamma-ray vision". In: *Nuclear Instruments and Methods in Physics Research Section A: Accelerators, Spectrometers, Detectors and Associated Equipment* 878 (Jan. 2018), pp. 159–168. DOI: 10.1016/j.nima.2017.08.040. URL: https://doi.org/10.1016/j.nima.2017.08.040.

Books only

[Att86] Frank Herbert Attix. *Introduction to Radiological Physics Radiation Dosimetry*. 1st ed. Wiley-VCH, 1986. ISBN: 0471011460,9780471011460 ,9783527617142.

[Eds82] J. Poate (Eds.) *Laser Annealing of Semiconductors*. Academic Press, 1982. ISBN: 978-0-12-558820-1,0-12-558820-8.

[Kno10] Glenn F. Knoll. *Radiation Detection and Measurement*. 4th. Wiley, 2010. ISBN: 9780470131480.

[Kra87] Kenneth S. Krane. *Introductory Nuclear Physics*. 1st ed. Wiley, 1987. ISBN: 9780471805533,047180553X.

[Nea02] Donald Neamen. *Semiconductor Physics And Devices*. 3rd ed. McGraw-Hill Science/Engineering/Math, 2002. ISBN: 9780072321074,0072321075.

[Sze81a] S.M. Sze. *Physics of Semiconductor Devices*. 2nd. John Wiley and Sons (WIE), 1981. ISBN: 047109837X,9780471098379.

[Sze81b] S.M. Sze. *Physics of Semiconductor Devices*. 2nd. John Wiley and Sons (WIE), 1981. ISBN: 047109837X,9780471098379.